NTNU

Norwegian University of
Science and Technology

# Optimization and verification of dosimetric robustness of VMAT dose-plans

Camilla Hægeland

Master of Science in Physics and Mathematics
Submission date: June 2016
Supervisor: Catharina de Lange Davies, IFY
Co-supervisor: Jomar Frengen, St. Olavs Hospital

Norwegian University of Science and Technology
Department of Physics

# Abstract

Radiation therapy has for several years played an important role in the curative management of patients with early stage disease and also in the palliation of symptoms associated with advanced or metastatic disease. Organs at risk (OAR) and normal healthy tissue located around the tumor may receive a high radiation dose that can cause serious side effects and altered quality of life. A highly conformal and precise dose delivery is therefore very important for a successful treatment. Volumetric modulated arc therapy (VMAT) is a relative new radiation technique that has become a conventional method used in radiotherapy. VMAT is arc-based, in which the gantry speed, multi-leaf collimator (MLC) position, and dose rate vary continuously during dose delivery. In this thesis the dosimetric predictability of VMAT plans has been studied.

A Delta4 phantom from ScandiDos was the main detector used for the measurements of dose distributions and verification values of treatment plans. A diamond detector and a gafchromic EBT film were also used in measurements of small field sizes and the penumbra region. A verification depends on how well the delivered dose and its spatial coordinates correspond to a calculated value. For the Delta4 phantom the $\gamma$-index was used as a comparison index for the verification, including both the dose deviation (DD) and the spatial deviation (DTA, distance to agreement). The $\gamma$-index analyzes the deviation between the calculated and measured dose distribution. The criteria to the $\gamma$-index was set to 3 % / 3 mm, allowing a maximum DD of $\pm$ 3 % and maximum DTA of $\pm$ 3 mm.

The robustness against introduced offsets were tested for two different optimization sequences for eight clinical treatment plans. The two sequences had a simultaneous and a sequential sequence, where the arrangement of added object functions/constraints to the plan differed. The introduced offsets were both physical MLC offset, and simulated offsets of geometrical parameters in the linac model, simulated in the doseplanning system.

In RayStation treatment planning system (TPS) different scripts were made to extract information from treatment plans in the TPS, and to create plans with specific MLC behavior. The extracted MLC information was used in numerical analyzes of differences in the MLC positions, comparing different optimization sequences (sequential, simultaneous, and the original clinical optimization) for the eight clinical treatment cases. The extracted information was related to the complexity of a treatment plan, and which of the optimization sequence that may result in a less complex and more robust plan. Plans with specific MLC behavior were used to study MLC characteristics and uncertainties regarding the dynamic MLC movements. Specific plans were created for measurements of the gravitational effect on the MLC leaves, small field dosimetry, and MLC motion.

In this study MLC characteristics and the robustness of VMAT plans have been studied, trying to get a better understanding of the dosimetric predictability of VMAT plans. A robustness-index has been suggested, based on the results in this thesis, giving an estimate of the robustness and complexity of a treatment plan.

# Sammendrag

Strålebehandling har i flere år vært en viktig rolle i den kurative behandling av pasienter med en tidlig sykdomsfase, og i lindring av symptomer assosiert med avansert eller metastatisk sykdom. Risiko organer (OAR) og normalt friskt vev som ligger rundt svulsten kan få en høy stråledose, noe som kan medføre alvorlige bivirkninger og endret livskvalitet. En konform og presis dose levering er derfor svært viktig for en vellykket behandling. Volumetric arc therapy (VMAT) er en relativ ny strålingsteknikk som har blitt en konvensjonell metode, brukt i stråleterapi den dag i dag. VMAT er arc-basert, karakterisert ved en gantry rotasjon, multi-leaf collimator (MLC) bevegelse, og doserate som kontinuerlig varierer i løpet av bestrålingen. I denne oppgave ble den dosimetriske forutsigbarheten til VMAT planer studert.

Et Delta4 fantom fra ScandiDos ble brukt som hoved detektor i målinger av dose fordelinger og verifisering av behandlingsplaner. En diamant-detektor og en gafchromic EBT film ble også benyttet i målinger av små feltstørrelser og penumbra-området. En verifisering avhenger av hvor godt avgitt dose, og dets romlige koordinater, samsvarer med en beregnet verdi. For Delta4 fantomet ble $\gamma$-indeksen anvendt som en sammenlignings-indeks for verifisering, som inkluderer både dosen avvik (DD) og romlige avvik (DTA). Dermed analyserer $\gamma$-indeksen avviket mellom beregnet og målt dose fordeling. Kriteriene til $\gamma$-indeksen var satt til 3% / 3 mm, noe som gir et maksimum i DD på 3 % og i DTA på 3 mm.

Robustheten, ved introduserte offset, ble testet for to forskjellige optimaliseringssekvenser for åtte kliniske behandlingsplaner. De to sekvensene hadde en samtidig og en sekvensiell sekvens, hvor rekkefølgen av objektfunksjoner lagt til behandlingsplanen var forskjellig. De introduserte offsetene bestod både av fysisk MLC offset og simulert offset av geometriske parametre i linac modellen, simulert i doseplan systemet RayStation.

I RayStation behandling planleggings system (TPS) ble ulike skript brukt til å hente ut informasjon fra behandlingsplaner. Skript ble også brukt til å lage planer med spesifikk MLC bevegelse. Den uthentede MLC informasjon ble anvendt i numeriske analyser av forskjeller i MLC posisjon, og sammenligninger ble gjort av de ulike optimaliseringssekvensene (sekvensiell, samtidige, og den opprinnelige klinisk optimaliseringen), for de åtte kliniske behandlingsplanene. Den uthentede informasjonen ble relatert til kompleksiteten for behandlingsplaner, og til hvilke av optimaliseringssekvensene som resulterte i den minst komplekse og mest robuste planen. Planer med spesifikk MLC bevegelse ble brukt til å studere MLC karakteristikk og usikkerhet tilknyttet de dynamiske MLC bevegelsene. Spesifikke planer ble også opprettet for målinger av effekt av gravitasjons feltet på MLC bladene og dosimetrien for små felt.

I dette studiet ble MLC karakteristikk og robustheten til VMAT planer studert, for å prøver og få en bedre forståelse av dosimetrisk forutsigbarhet for VMAT planer. En robusthets-indeks har blitt foreslått, basert på resultater fra denne oppgaven, som gir et anslag på robustheten og kom-

pleksiteten til behandlingsplaner.

# Preface

The present report is my master's thesis in Biophysics and Medical Technology, written for the Norwegian University of Science and Technology (NTNU). The work was carried out at the Department of Radiotherapy at St. Olavs Hospital, Trondheim, during the spring of 2016.

I would especially like to thank my supervisor Jomar Frengen, a medical physicist at the Department of Radiotherapy, for his continuous guidance, help and support through the assignment. I would like to give a big thank to the other staff at the radiotherapy department for good availability, positivity and guidance when needed.

Also, I would like to thank Professor Catharina de Lange Davies, my supervisor at the Department of Physics, NTNU, for giving valuable feedback in the writing process.

Camilla Hægeland,

Trondheim,

June, 2016.

# Table of Contents

# Abbreviations

| | |
|---|---|
| **AAA** | Analytical anisotropic algorithm |
| **BEV** | Beam-eye-view |
| **CC** | Collapsed cone |
| **CCD** | Charge-coupled device |
| **CP** | Control point |
| **CPE** | Charged particle equilibrium |
| **CT** | Computed tomography |
| **DD** | Dose deviation ($\delta$) |
| **DLG** | Dynamic leaf guides |
| **DOV** | Dose volume histogram |
| **DTA** | Distance to agreement |
| **DVH** | Dose volume histogram |
| **FWHM** | Full width at half maximum |
| **GTV** | Gross tumor volume |
| **IM** | Internal margin |
| **IMRT** | Intensity modulated radiation therapy |
| **ITV** | Internal target volume |
| **KERMA** | Kinetic energy released per mass unit |
| **LINAC** | Linear accelerator |
| **MC** | Monte Carlo |
| **MU** | Monitor unit(s) |
| **MLC** | Multi leaf collimator |
| **OAR** | Organ at risk |
| **OPF** | Output factor |
| **PB** | Pencil beam |
| **PE** | Photoelectric effect |
| **PP** | Pair production |
| **ROI** | Region of interest |

| | |
|---|---|
| **SB** | Strålebehandling |
| **SAD** | Source-axis distance |
| **SDD** | Source-to-diaphragm distance |
| **SM** | Setup margin |
| **SSD** | Source-to-skin distance |
| **T&G** | Tongue and Groove |
| **TERMA** | Total energy released per unit mass |
| **TM** | Total margin |
| **TPS** | Treatment planning system |
| **VMAT** | Volumetric modulated arc therapy |
| **QA** | Quality assurance |
| **3D-CRT** | three-dimensional conformal radiation therapy |

Chapter 1

# Introduction

Radiation therapy has experienced a huge improvement during recent years, including the development of new imaging techniques that have resulted in a more precise measurement of target volumes and margins [Newbold et al. (2006)]. An important goal in radiotherapy is to reduce the radiation dose to normal tissue, and thereby increase the chance for a successful result. The development of delivering techniques has therefore been in focus, leading to an improvement in dose distribution and conformity [Thwaites and Tuohy (2006)].

Conventional delivering techniques commonly used today are 3D-CRT (three-dimensional conformal radiation therapy), IMRT (intensity-modulated radiation therapy) and VMAT (volumetric modulated arc therapy). All of these techniques constitutes of MLCs (multileaf collimators) that define the shape of the radiation field. In 3D-CRT the radiation beams are matched to the shape of the tumor and delivered from several directions, each with a specific MLC shape. IMRT plans have multiple MLC shapes per gantry angle and can vary the beam intensities during the irradiation to achieve the desired dose-distribution. VMAT, an arc-based rotational therapy, was developed to overcome some of the limitations to the fixed field IMRT. The concept of arc therapy is a continuously rotation of the treatment source around the patient. A reduction in both time and use of monitor units (MU) was obtained with VMAT, resulting in a more efficient delivery of the radiation with reduced irradiation to the rest of the body [Palma et al. (2010)].

VMAT is a novel technique, introduced in 2007 [Yu (1995)], and allows a simultaneous variation of three parameters during the irradiation; gantry rotation speed, the shape of the MLC, and the dose rate [Otto (2008)]. VMAT combines inverse planning, intensity modulation, and arc therapy for radiation delivery, resulting in a short treatment duration. Some studies have also shown that VMAT gives a better dosimetric plan [Otto (2008), Yu (1995)]. However, complex treatment plans, as those obtained with VMAT, require a dosimetric quality assurance (QA) before clinical delivery. If the medical physicist obtains more information about each component's characteristic in the radiation treatment, a dosiemtric verification may not be necessary, thereby reducing time spent on QA.

This thesis builds on my specialization project done in the fall 2015 [Hægeland (2015)] and the nine clinical patient cases studied there. In the spring of 2015 St. Olavs Hospital switched treatment

planning system from Oncentra Masterplan to RayStation. In that context, a dosimetric verification was done with a Delta4 phantom before treatment of the first 66 VMAT-patients. Nine patient cases with the poorest verification outcome were selected to be further studied. The goal was to learn, in general, why some treatment plans are associated with a poorer QA outcome. In the project thesis two different optimization sequences were made that resulted in different verification values for the nine patient cases. It was concluded that the optimization process has influence on the final patient outcome. These two sequences, called sequential and simultaneous, continued to be used in this context, studying the robustness against different offsets.

The scope of this thesis is primarily to explore the robustness of complex VMAT plans. Possibilities in the treatment planning system RayStation were exploited by scripting in the software. Different scripts were made to extract information of a VMAT plan and to make 3D-CRT and VMAT plans with specific MLC behavior. Plans with specific behavior made it possible to analyze different characteristics of the MLC leaves: the dynamic movement of the leaves, the tongue-and-groove effect (an under-dosage as a result of the MLC shape), the effect of the gravity field, and different field sizes (MLC openings). The MLC leaves were pushed to the limit of constraints to study their behavior at extreme situations. The extracted plan-information from different scripts was used to analyze a specific treatment plan and compare it to either a plan within the same patient or to a different patient plan. The main goals were to establish a robustness-parameter for treatment plans that could determined the need for an individual dosimetric quality assurance, and to achieve a better understanding of the different components' behavior during irradiation.

Chapter 2

# Background

## 2.1 Radiation equipment

The linear accelerator (linac) customizes the radiation treatment to conform to the shape of the tumor, destroying the cancer cells while sparing the surrounding normal tissue. All body sites can be treated with the best suitable type of radiation, created by the linac.

### 2.1.1 Linear accelerator

The electrons, sent through the long cylindrical accelerator, get sufficient energy when passing the synchronized radio-frequency electromagnetic field, gaining a speed close to the speed of light [Manual (2012)]. The high energetic electron beam (usually 6 or 15 MeV) can either be used directly as radiation therapy for shallow tumors or be converted to a photon beam for treating deeper situated tumors. The photon beam is created when the electron beam hits a target creating Bremsstrahlung radiation. A spectrum of different photon energies and directions is obtained and is attenuated by a flattening filter, focused by rectangular collimators (jaws) and shaped by multi-leaf collimators (MLC).

**Fig. 2.1** shows the setup of the linac. The magnetron sends pulsating radio frequency waves into the waveguide, synchronized with injection of a pulsed electron beam from the electron gun [Laboratories (2012c)]. The radio frequency waves accelerate the electron beam to a speed approaching the speed of light. The waveguide is composed of a long cylindrical tube containing a series of copper cells in vacuum, to prevent interaction with other particles. Together with two sets of magnets along the waveguide small holes between these copper cells ensure a focused beam.

After passing through the waveguide the electrons in the beam have slightly different energies, and therefore need to pass an achromatic bending system so that all the electrons exit at the same point and direction. The Elekta linac uses a slalom bending system to perform this task [Mayles

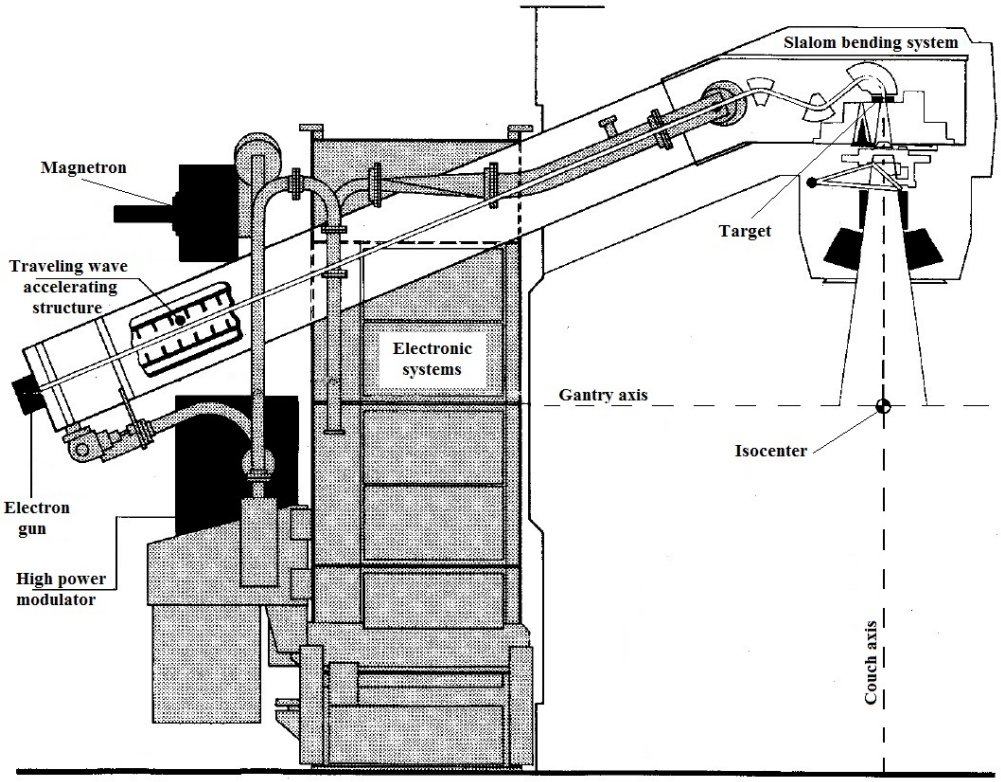


**Figure 2.1:** The main components of the linac. The magnetron produces microwaves to accelerate the electrons produced by the electron gun through the waveguide. The electron beam is shaped by the slalom bending system before it collides with a target (tungsten) creating high energy photons. The radiation can be delivered from any angle by rotating the gantry and the treatment couch.

et al. (2007)]. Three magnets cause the electron beam to bend through the slalom-trajectory, focusing the beam to a diameter of 1 mm. This technique is unique for the Elekta linac, which minimizes the size of the machine, and ensures that the isocenter remains low (important for the patient setup).

### 2.1.2 Radiation treatment modalities

The main goal of radiotherapy is to deliver the desired dose to target volumes, while sparing the healthy adjacent tissue to an acceptable dose level. The multi-leaf collimator (MLC) has become an important factor in achieving this goal, by shaping the photon/electron beam according to the tumor volume and making it possible to obtain a conform radiation. Treatment techniques that are commonly used in radiotherapy today are 3D-CRT, IMRT and VMAT, which all consist of MLC-based delivery and use information from modern imaging modalities such as CT and MRI.

#### 3D conformal radiation therapy

Conventional three-dimensional conformal radiation therapy (3D-CRT) uses collimators to conform the treatment fields to the shape of the tumor. Fields are delivered from several directions,

each with a specific MLC shape, delivered dose and fluence intensity. The shaping of 3D-CRT fields is very complicated and time-consuming.

#### Intensity modulated radiotherapy

Intensity modulated radiotherapy (IMRT) is composed of a discrete number of beams delivered from fixed gantry angles, usually 4-8 different beam angles. Each beam is subdivided into several segments, each with a specific MLC shape, thereby controlling and modulating the delivered dose. Continuously moving MLC leaves deliver a more conform treatment field to the target volumes compared to 3D-CRT. However, IMRT is a time-consuming technique, mainly because each segment may vary in both shape and size, and time used is required to change the gantry angle. Common effects of the long treatment time are poorer reproducibility of the treatment position due to intrafraction motion, and the ability to treat fewer patients each day. Also, during the extra treatment time the tumor's reparation and repopulation has been shown to increase, resulting in radiobiological implications [Wang et al. (2003)].

#### Volumetric modulated arc therapy

Volumetric modulated arc therapy (VMAT) is the newest technique for delivering external photon beam radiotherapy, introduced in 2007 and proposed by Yu in 1995 [Yu (1995)]. VMAT is a development of IMRT where the gantry rotates around the patient with the radiation constantly on. A VMAT plan consists of one or more arcs, where an arc is defined as a gantry rotation of up to 360°. The MLC leaves move continuously along with the gantry rotation achieving a conform dose distribution. The gantry moves with different speed and dose rate (MU per time) during an arc to achieve the desired dose distribution. The treatment time has been shown to be reduced to one third compared to IMRT and to produce better treatment plans [Oliver et al. (2009), Yu (1995)].

### 2.1.3 Isocenter and coordinate system

The position of the isocenter is the beam's primary reference location, and is located in the intercept between the axis of the gantry rotation and the central beam [Mayles et al. (2007)]. Three laser devices are used to indicate the position of the isocenter in the treatment room, as shown in **fig. 3.2**. The gantry (arc motion), collimators and the treatment table rotate around the isocenter and the beam irradiation is calibrated with high precision [Litzenberg et al. (2013)] to ensure high accuracy during the different rotations. The isocenter is also the origin of the coordinate system used in the treatment planning system (TPS) RayStation (RaySearch Laboratories, Stockholm, Sweden).

In the workspace of RayStation TPS the beams-eye-view (BEV) can be visualized (**fig. 2.2a**), seen from the gantry head through the collimators. The collimator angle is defined to be positive for counterclockwise rotation in the BEV and may take a value between 0° – 180°, e.g. **fig. 2.2a** has a collimator angle of +5°. The blue arrow in **fig. 2.2b** represents the positive rotation of the collimator angle.

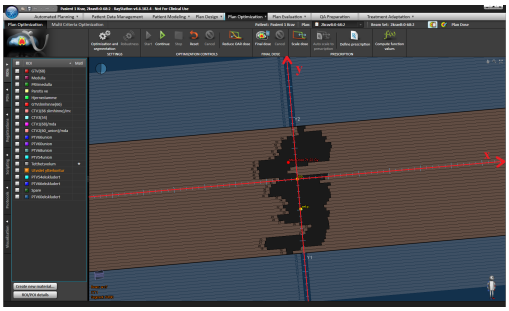

**(a)** The xy-axis in the BEV

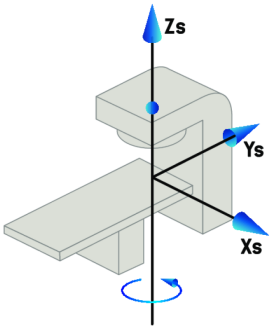


**(b)** Reference coordinate system

**Figure 2.2:** Coordinate system used in the RayStation TPS.

### 2.1.4 Collimators

The Elekta linac has a maximum field size of 40 x 40 $cm^2$ at the linac isocenter, created by collimators [Laboratories (2012c)]. The primary collimators and the jaws are placed close to the photon beam source and define the limits of the opening in the y- and x-direction respectively. The schematic structure of the main physical linac components are presented in **fig. 2.3**.

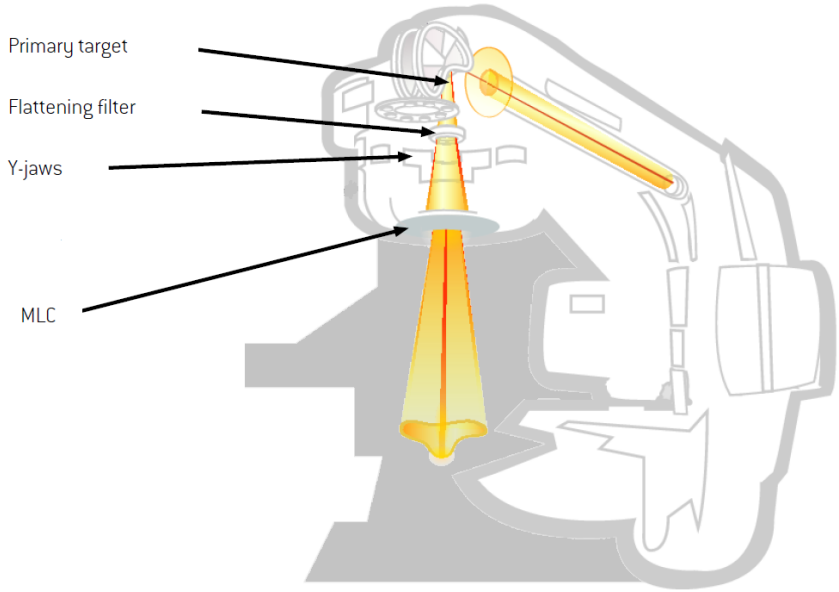


**Figure 2.3:** The highlighted area represents the electron beam, which is converted to a photon beam at the primary target. The flattening filter smoothes out the axial photo-fluence before the photon beam passes the y-jaws and is shaped by the MLC leaves. The picture is taken from [Laboratories (2012b)].

The secondary beam defining collimator, the multi-leaf collimator (MLC), shapes the radiation

field with high accuracy and efficiency to ensure that it matches the shape of the tumor. Modifications have been made to the MLC leaves giving rise to many different variants (an overview of different variants are shown in **fig. 2.4**). At the department of St. Olavs the linacs come from the vendor Elekta, Versa HD. Versa HD features Agility MLC that has 80 x 2 MLC leaves (one MLC bank on each side consisting of 80 leaves), each with a leaf width of 5 mm and thickness of 90 mm, and with a 40 x 40 $cm^2$ treatment field. All leaves move independently of one another, thereby enabling the linac to create a variety of complex treatment shapes [Elekta (2012)].

The MLC leaves are supported by dynamic leaf guides (DLG) that allows the leaves to move up to 15 cm over the central axis of the beam. Adding the two maximum speeds of the DLG (30 mm/s) and MLC leaves (35 mm/s) the total maximum leaf speed is 65 mm/s [Vorwerk et al. (2008)]. A single set of diaphragms (y-jaws) move perpendicular to the MLC and can over-travel the central axis by up to 15 cm. Both leaf and diaphragm ends are rounded. **Fig. 2.4** shows the schematics of the DLG, diaphragm and the MLC leaves for the Agility collimator.

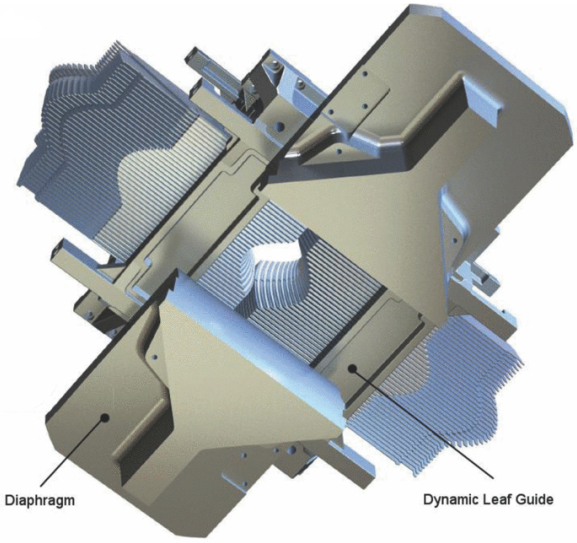


**Figure 2.4:** Schematic representation of how the MLC leaves, diaphragms and DLGs are positioned for the Agility collimator. The picture is taken from [Thompson et al. (2014)].

The gaps between the leaves are tilted slightly against the beam to reduce overall transmission and minimize the interleaf leakage. A CCD (charge-coupled device) camera is used to acquire an image of the fluorescent elements on the top surface of the leaves. The linac control system uses these images to determine the positions of the leaves and is presented in the BEV of the linac software.

**Definitions of MLC properties: tongue-and-groove effect, MLC speed and MLC island**

As previous mentioned different vendors have designed different profiles of the MLC leaf in order to reduce interleaf leakage (**fig. 2.5**). This spatial extent/tilting is taken into account in the tongue-and-groove (T&G) parameter in RayPhysics, where the linac geometry can be set (see **2.7.3**). The tongue-and- groove effect can thereby be tuned to a value so that the measured and calculated dose curves correspond. The T&G-offset at St. Olavs Hospital is set to 0.05 cm.

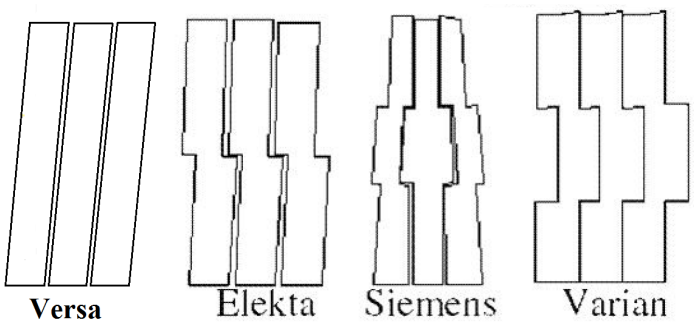


**Figure 2.5:** Different vendors have different designs of the MLC leaves to reduce the interleaf leakage. St. Olavs Hospital have Agility collimator from Versa.

The **MLC flank** is created when the long-side of the MLC leaves are exposed to an opened field. It is here the tongue-and-groove effect makes a contribution to the final dose. For the agility MLC-model, the leaves are tilted and the transmission through the tongue-and-groove region will be the square-root of the MLC transmission [Laboratories (2012b)]. **Fig. 2.6**, seen from BEV, shows where three contributions of the T&G effect are placed at the periphery of the radiation field affecting the transmission, indicated with a red marker. The T&G effect has a relative negligible influence on large fields. However, the effect is additive and can be of significant value over many fields, especially for VMAT plans consisting of many segments.

**MLC speed** is in this thesis defined as the distance one MLC leaf travels between two subsequent segments/control points. In **fig. 2.7** two consecutive segments are represented: **fig. 2.7a** depicts the first segment and **fig. 2.7a** the second segment. The distance traveled by a MLC leaf between these two segments will be defined as the speed, measured in cm/deg.

An **MLC island** refers to an MLC opening surrounded by MLC leaves. Each segment has at least one MLC island, delineated by the y-jaws, but may contain several MLC islands. **Fig. 2.8** shows how the MLC positions are placed making a segment of five MLC islands. The MLC leaves no. 30 and 31, 36 and 37, 39 and 40, 42 and 43 are overlapping giving rise to the MLC islands.

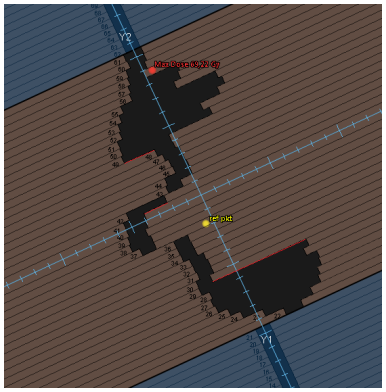

**Figure 2.6:** The field opening of the MLC leaves seen from BEV in RayStation TPS. Three MLC flanks are indicated with a red marker.

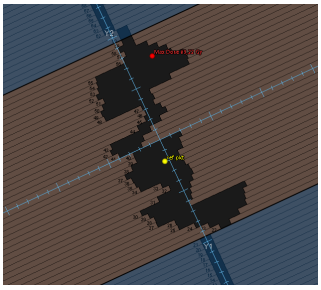

**(a)** First segment

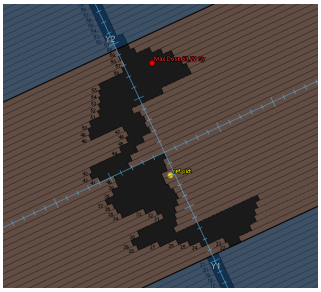

**(b)** Second segment

**Figure 2.7:** Two consecutive segments of patient case no. 7, showing the movement of MLC leaves between two segments, which is defined as the travel distance or the MLC speed.

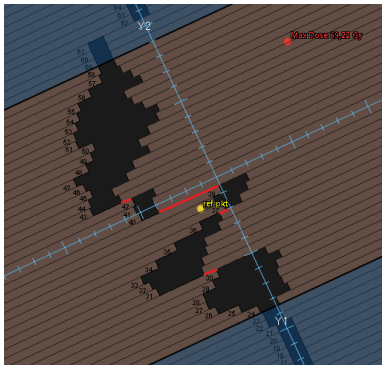

**Figure 2.8:** Where the MLC leaves from opposite sides make a closure, an MLC island is created at each side of this closure. In this segment four MLC closures are present (red markers) giving rise to five MLC islands.

### 2.1.5 Penumbra

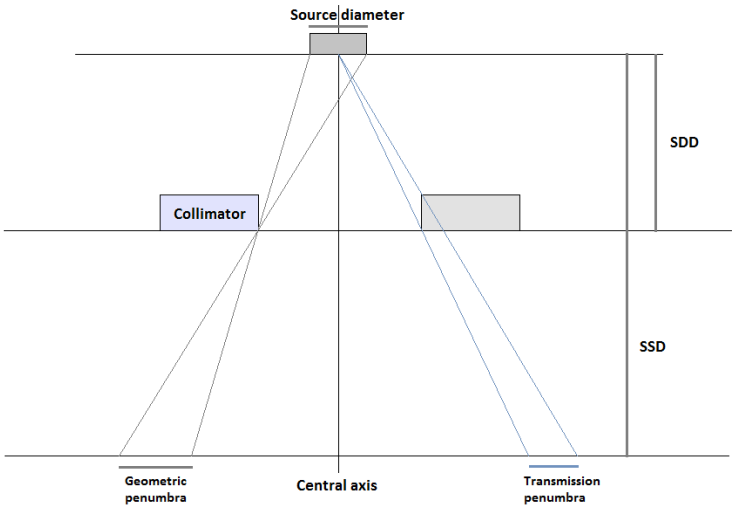


**Figure 2.9:** Presentation of the geometric and transmission penumbra (not to scale). The geometrical penumbra is a result of the source width. The transmission penumbra is a result of different amounts of photons transmitted through the collimator, depending on the thickness of the collimator through which the photon beam travels.

The penumbra indicates the region at the lateral edges of a radiation beam where the dose rate changes rapidly as a function of distance from the beam axis. This region is commonly defined as the area between the 20 % and 80 % isodose lines, represented with red lines in **fig. 2.23**. Three components add up to the total penumbra, called physical penumbra [ICRU (1976)]: transmission, geometric and scatter penumbra. The geometric penumbra results from a finite source diameter and is therefore affected by the source-to-skin distance (SSD) and the distance from the source to the distal end of the diaphragm (SDD). The transmission penumbra is the resultant of the edge of the collimators not being parallel to the edge of the beam transmission penumbra, and will therefore be more pronounced for larger field sizes due to a greater obliquity of the rays at the edges of the collimators. The transmission penumbra may smear the geometric penumbra. The scattered penumbra is due to in-patient X-ray scatter, dependent on the beam energy. The size of the physical penumbra region is therefore affected by the size of the source/target, the radiation/photon energy, SSD, the collimating system, and whether electronic equilibrium is present or not [Podgorsak (2005)]. **Fig. 2.9** shows the principles of the geometric and transmission penumbra.

The penumbra is affected by the field size, where for small fields the region may overlap. For large field sizes the entire source can be viewed from the detector's point of view, CPE (charged particle equilibrium) can be obtained, and the FWHM (full width at half maximum) of the dose profiles is approximately at 50 % of the dose level of CPE (**fig. 2.10a**). For very small field sizes

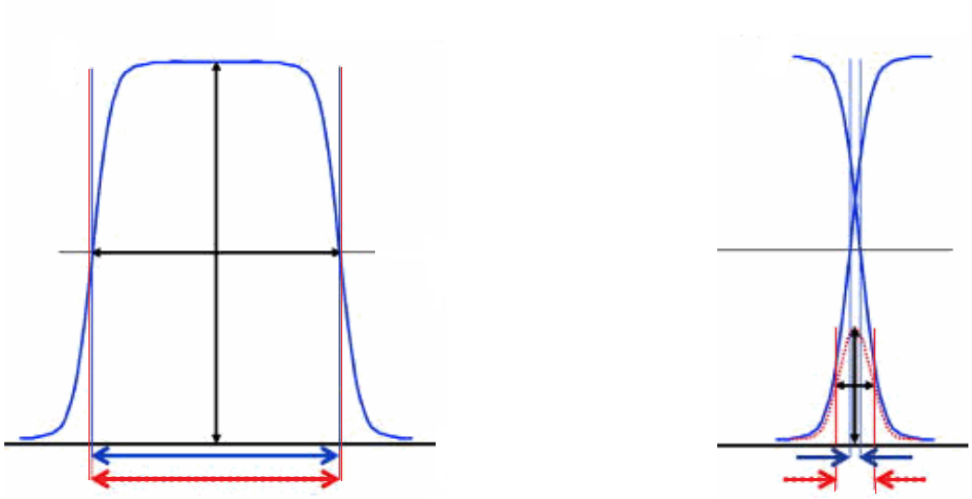

**(a)** Large field size

**(b)** Small field size

**Figure 2.10:** For large field sizes the FWHM of the dose profiles will be approximately at 50 % of the dose level of CPE. For very small field sizes the penumbra from opposing field edges may overlap and the FWHM will be below the 50 % dose level, resulting in an under-dosage.

the penumbra from opposing field edges may overlap. This will cause an error in the field size determination due to the FWHM data and the resulting field size will be overestimated (**fig. 2.10b**.)

### 2.1.6 Monitor units

A monitor unit is the measured output of radiation exposure, measured by a monitor chamber inside the linac head. It is common to calibrate the linac so that 1 gray (Gy) absorbed dose corresponds to 100 MU delivered to a point at a depth of 10 cm in a water phantom. The field size is 10 x 10 $cm^2$ measured with a distance of 90 cm between the linac source and the surface of the phantom [Laboratories (2012c)].

1 Gy is defined as 1 joule (J) absorbed radiation energy per kilogram (kg) of matter [Brochure (2006)]. The number of MU required to deliver a specified dose to a point at a desired depth is calculated by the software program RayStation [Laboratories (2012c)]. To control the amount of MU delivered to the patient an ionization chamber inside the linac head measures the fluence passing through, thereby counting the MU. RayStation TPS calculates the amount of MU needed to fulfill the desired dose distribution to a plan.

## 2.2 Delta4 phantom

Complex radiotherapy treatment plans such as IMRT, VMAT and TomoTherapy require a dosimetric verification before clinical delivery. To verify the plan, a phantom and its software are used to measure the delivered dose distribution, compare it to the planned dose and analyze it against the

selected pass/fail criteria. St. Olavs Hospital uses the Delta4 Phantom from ScandiDos, with high accuracy and efficient quality assurance [Bedford et al. (2009)].

**Figure 2.11:** Conventional linac at St. Olavs Hospital, shown with the Delta4 phantom placed on the patient treatment table.

### 2.2.1 Technical equipment

A phantom is a cylindrical shaped polymethylmethacrylate (PMMA) device that replaces the patient anatomy, **fig. 2.11**, and is used for quality assurance (QA) and verification of treatment plans. The phantom from ScandiDos has 1069 diode detectors arranged in a matrix along two crossing orthogonal planes, **fig. 2.12**. The phantom is able to measure a three-dimensional dose map, providing full coverage of the cross-section in any beam direction. The total detection area is 20 x 20cm$^2$ per plane, where a central area around the isocenter (6 x 6 cm$^2$) is composed of diodes at a distance of 0.5 cm between them. The outer area has a distance of 1.0 cm between the diodes.

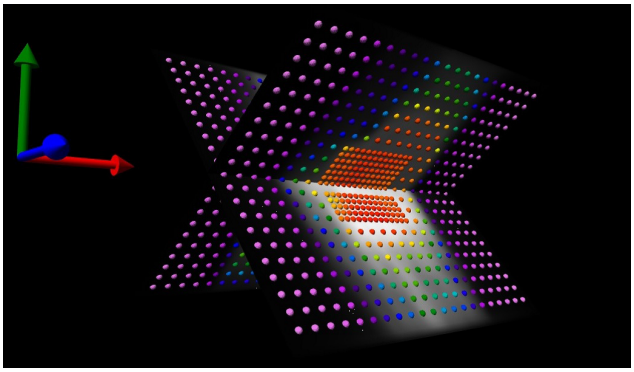

**Figure 2.12:** A cylindrical phantom consists of two orthogonal cross planes with detectors, where the concentration of detectors is higher in the central area. Each beam can be studied individually. Red color equals high dose while violet equals low dose.

Individual beams can be studied together with the composite dose, absolute dose and the dose

distribution, all at the same time, building a 3D dose-picture. A verification of the dose gradients in x, y, and z directions can then be achieved.

### 2.2.2 Daily correction factor

To correct for the daily differences in radiation output of the linac, a daily correction factor is added. The factor is derived from a selected measurement done on a 10 x 10 $cm^2$ field at gantry degrees of 90° and 270°, which is compared to a calculated dose. If there is a deviation between the calculated and measured dose it will be accounted for by a correction factor. In the Delta4 software the user has the option of either applying this factor or inserting a factor manually.

### 2.2.3 Pass/fail criteria

The measured data is saved in the Delta4 software where the parameters dose deviation (DD), distance to agreement (DTA) and the gamma index ($\gamma$-index) are calculated and compared. The $\gamma$-index [Low and Dempsey (2003)] has become a standard technique for planar dose verification in IMRT QA [Winiecki et al. (2010)] and VMAT QA [Qian et al. (2011), Defoor et al. (2015)]. The $\gamma$ calculates the outcome of the QA using the preselected dose difference (DD) and distance to agreement (DTA) for a point of interest [Low et al. (1997)]. Common values selected for DD and DTA are 3 %/3 mm (which also are the criterion at St. Olavs Hospital), meaning that the tolerated deviation in the local dose is maximum 3 % and that the tolerated deviation in the distance is maximum 3 mm. A cut-off is also selected for points receiving less than 50 % of the dose maximum.

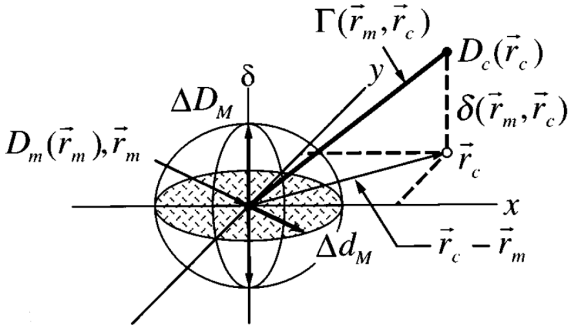


**Figure 2.13:** Representation of the dose distribution evaluation criteria combining the ellipsoidal DD and DTA test. The measurement is used as the reference information, and the calculated surface representing the acceptance criterion [Low et al. (1997)].

The DTA criterion is represented by a disk in the x-y plane with radius equal to $\Delta d_M = r_m$ - $r_c$ (= 3 mm), **fig. 2.13**. If the calculation point $D_c(r_c)$ intersects this disk the DTA criterion is fulfilled and the calculated distribution passes the DTA test at this point. Along the $\delta$-axis the dose difference represents with its length $2\Delta D_M$. The DD criterion is within acceptance if $\mid D_c(r_c)$ –

$D_m(r_m) \mid \leq \Delta D_M$ (= 3%) is fulfilled. The ellipsoid (**fig. 2.13**) is representing the acceptance criterion for both the DTA and the DD, and is therefore also the basis for the $\gamma$ criterion, with the equation defining the surface:

$$1 = \sqrt{\frac{\mid r - r_m \mid^2}{\Delta d^2} + \frac{(D(r) - D_m(r_m))^2}{\Delta D^2}}. \tag{2.1}$$

This equation can be used to identify the $\gamma$-index at each point in the evaluation plan $r_m - r_c$ for the measurement point $r_m$,

$$\gamma(r_m) = \min\big[\Gamma(r_m, r_c)\big], \tag{2.2}$$

where

$$\Gamma(r_m, r_c) = \sqrt{\frac{\mid r_c - r_m \mid^2}{\Delta d^2} + \frac{(D_c(r_c) - D_m(r_m))^2}{\Delta D^2}}. \tag{2.3}$$

$\mid r_c$ - $r_m \mid$ is the difference in distance and $D_c(r_c)$ - $D_m(r_m)$ is the dose difference between the calculated and the measured distribution. The pass/fail criterion therefore passes if $\gamma \leq 1$, and fails if $\gamma > 1$. At St. Olavs Hospital will a treatment plan be verified if 90 % of the dose-points pass the $\gamma$-criterion.

## 2.3 Dosimetry

The intensity to the radiation passing through matter is gradually attenuated because of the energy deposition interactions. For a monoenergetic photon beam the intensity $I(x)$ decreases exponentially as the beam travels through a unit of thickness $x$ in the matter, by the following equation:

$$I(x) = I_0 e^{-\mu x},$$

where $I_0$ is the initial intensity on the surface of the matter and $\mu = n \cdot \sigma$ is the absorption/linear attenuation coefficient [$cm^{-1}$]. $n$ is the number of atoms per $cm^3$ in the matter, and $\sigma$ is the absorption cross section [$cm^2$].

An atom can either be directly or indirectly ionized. Direct ionization by photons happens through a photon interaction (photoelectric effect, Compton scattering or Pair production, depending on the photons energy), and directly damages the DNA by breaking its bonds. Indirect ionizing radiation deposits energy in the absorber through two steps. The first step is the transfer of energy through photon interaction to secondary charged particles, quantified as KERMA (kinetic energy released per mass unit). KERMA is defined as the kinetic energy transferred from the indirectly ionizing radiation to charged particles per unit mass. The second step is when the secondary particle (electorns) transfers the energy to the matter via atomic excitations or ionizations and results in absorbed dose. Indirectly ionizing radiation damages the DNA via radicals and reactive molecules.

### 2.3.1 Photon interaction with matter

Depending on the incident energy of the photon, $hv$, and on the atomic number Z of the tissue, various interactions may occur. The main interactions in radiation are the photoelectric effect (PE), Compton scattering (Compt), and pair production (PP). The total probability for the photon to interact is the sum of the cross-sections for each individual processes: $\sigma = \sigma_{PE} + \sigma_{PP} + \sigma_{Compt}$. In radiotherapy the energy of the photons is commonly around $6-20$ MeV, and therefore Compton scattering is the dominating interaction. The energy region each type of photon interaction dominates for a specific atomic number of the absorber is shown in **fig. 2.14**.

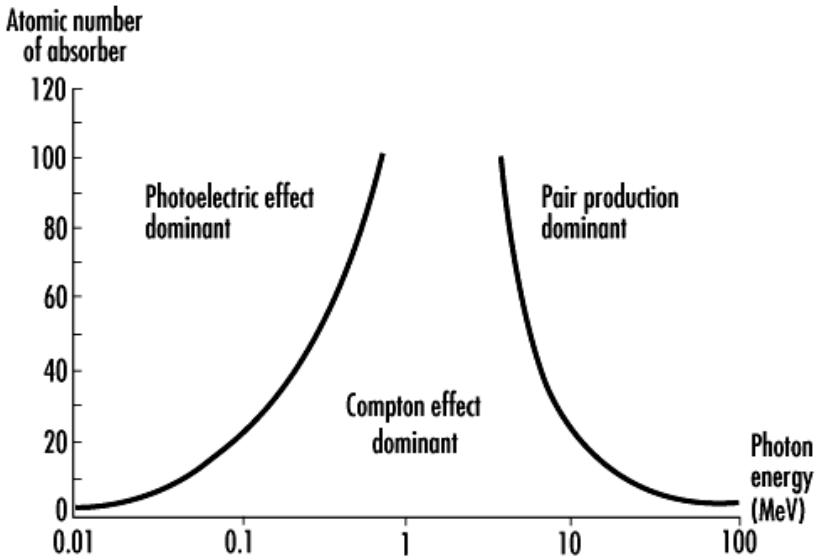


**Figure 2.14:** The three main photon interactions during irradiation for a specific atomic number Z of the absorber, in a specific energy region. The left and the right curves represent where the atomic coefficients for the PE and Compt, and Compt and PP are equal, respectively. The picture is taken from [Cherry (2012)].

In the **photoelectric interaction** a photon transfers all its energy to a tightly bound orbital electron which is ejected from the atom, passing through the surrounding matter with a kinetic energy $E_K = hv - E_B$, where $hv$ is the incident photon energy ($h$ = Placks constant, $v$ = frequency) and $E_B$ is the binding energy of the electron. The energy from the photon is therefore deposited in the matter close to the site of the photoelectric interaction.

In a **Compton interaction** the photon interacts with an orbital electron with incident energy much larger than the binding energy of the electron. The primary photon interacts with an electron in the atom, releasing this electron and scattering a lower energy photon (**fig. 2.15**). The electron deposits its energy locally by ionization while the scattered photon may travel further and undergo additional interactions.

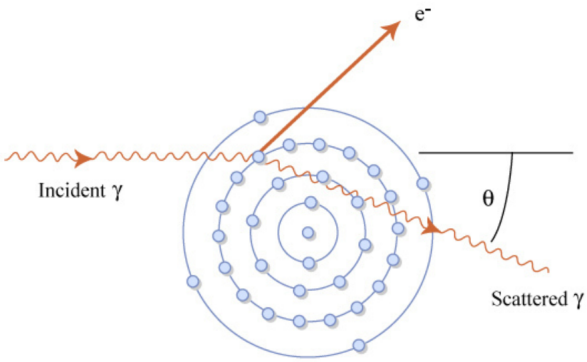


**Figure 2.15:** Compton scattering: an incident gamma ray interacts with an orbital electron, releasing this electron and emiting a lower energy gamma ray. The picture is taken from [Pillalamarri (2006)].

In **pair production** the photon interacts with the nucleus where its energy is converted into matter (an electron and a positron). The incident energy of the photon must therefore exceed two times the rest mass energy of an electron/positron ($2m_ec^2 = 1.02$ MeV).

### 2.3.2 Charged particle equilibrium

Charged particle equilibrium (CPE) is the phenomena when an equal amount of charged particles, $D_e$, are leaving a volume V as the number entering of a given particle type and energy. At CPE $D_e$ is equal to the amount of charged particle kinetic energy that will be deposited, $K_c$: $D_e = K_c$. True CPE is not possible to achieve in practice radiotherapy, though transient charged particle equilibrium (TCPE) is used. At TCPE electrons from "upstream" contribute to the dose and the photon contribution is the collision kerma, so TCPE is true if $D_e$ is proportional to $K_c$. The absorbed dose $D$ increases, during the dose build-up of charged particles, to a maximum $d_{max}$, and then reduces with depth. At depth $t_{max}$ the number of electrons will saturate. $t_{max}$ is the maximum range of the charged particles and the dose then follows the $K_c$. This is called the TCPE and is the same as the dose, only with a shift $X$: $D(x) = K_c(x - X)$.

### 2.3.3 Detectors

A wide range of radiation detectors are available in radiation dosimetry including ion chambers, film, diodes and diamond detector. Detectors are divided in three categories, according to the size of the volume that they are able to detect: standard, mini- and micro-detectors with accompanying volume sizes $\approx 10^{-1}$, $\approx 10^{-2}$, and $\approx 10^{-3}$ cm$^3$, respectively. Ion chambers are common detectors

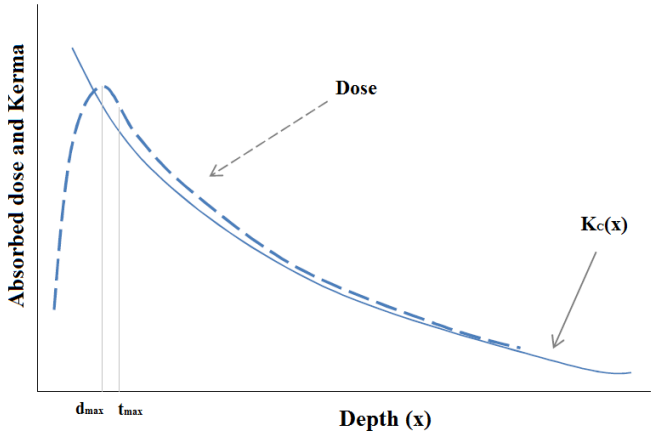


**Figure 2.16:** Illustrating transient CPE (TCPE). The dose builds-up to a maximum at $d_{max}$ and then reduces with depth. The dose follows the collision Kerma after $t_{max}$, which is the maximum range of the charged particles. Picture is taken from lecture of Kissick 2015.

used in radiation dosimetry. They exist in various shapes and sizes, are relatively inexpensive, have a small variation in response to energy, dose, dose rate, and reproducibility [Podgorsak (2005)]. Films are used for dose measurement based on optical density variation and are generally dependent on field size, depth and beam energy, and are divided in two types of films: silver halide and Gafchromic. Silver halide films require processing, whereas Gafchromic films are self-developing. Semiconductor diode detectors are also commonly used for photon and electron beams due to their quick response time, very good spatial resolution, high sensitivity, and absence of external bias. Diamond detectors have a relatively small sensitive volume, making them ideal for small field dosimetry and beam profile measurements. Diamond detectors' response is directly proportional to the absorbed dose rate.

When selecting a detector, the type of application, field size, resolution, and needed time to collect data should be taken into account. Profile measurements for small fields and high gradient regions depend on the choice of detector orientation. Dose profiles depend on the TPS, in terms of field sizes and depths, and may require in-plane, cross-plan, and diagonal profiles.

## 2.4 Definition of volumes

The volume of the organ being irradiated may play a significant role in its radiosensitivity. Different organs have different weightings of parallel and serial functional structure. Organs dominated with parallel structure (e.g. kidney, lung, liver, and tumor) are affected by the total dose to the volume, while damage to small volumes has no clinical toxicity. The opposite is the case for organs with serial structure (e.g. spinal cord), where damage to small volumes may produce toxicity. This affect the total and maximum dose that a certain volume can tolerate and must be taken into account

in the treatment plan optimization.

To get a meaningful 3-D radiotherapy treatment plan, certain volumes and margins must be defined using CT-studies in order to deliver the dose precisely. The radiotherapy planning is divided in three main volumes (GTV, CTV and PTV), plus the volume of the critical tissue structures, known as organs at risk (OARs). These volumes were introduced by the international commission on radiation units and measurements [ICRU (1976) reports 50 and 62]. A schematic of the volumes are shown in **fig. 2.17**.

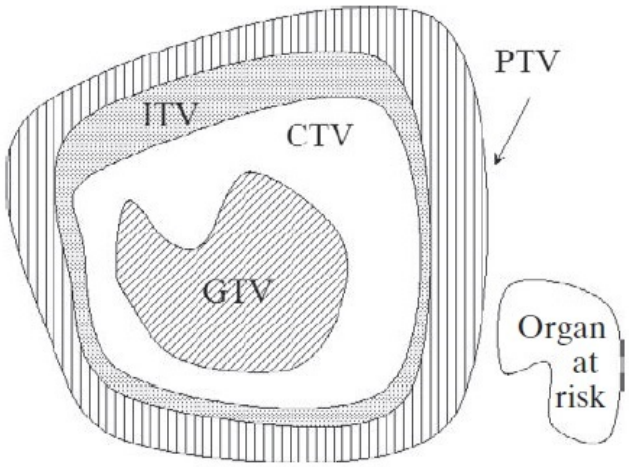


**Figure 2.17:** Schematic illustartion of the relation between the volume-of-interest and the OAR [Podgorsak (2005)]. GTV = gross tumor volume, CTV = clinical target volume, ITV = internal target volum, PTV = planning target volume

### 2.4.1 Target volumes

The physical extent and location of the malignant growth, observed by imaging techniques, is defined as the gross tumor volume (GTV). The clinical target volume (CTV) is the tissue volume including GTV plus an extra margin accounting for microscopic extension of the primary tumor, and/or lymph node spread that cannot be fully imaged.

An internal margin (IM) is added around CTV to compensate for movements and variations in the location, size and shape of the tissue. CTV and IM add up to the internal target volum (ITV), also known as the target volume. Because of patient motion (eg. breathing) and uncertainties in the setup (systematic or random errors) a setup margin (SM) is added. If IM and SM are independent of each other they can add up to a total margin (TM) by the formula TM = $\sqrt{\text{IM}^2 + \text{SM}^2}$. The

TM takes into account all the uncertainties and variations related to the patient and the equipment [Levernes (2012)].

Due to different variations and uncertainties in the treatment setup and delivery, a safety margin around the GTV and CTV must be added. This volume is called the planning target volume (PTV) and fully envelops the GTV and CTV creating a safety margin around them.

### 2.4.2 Organs at risk

Normal tissues with high sensitivity for radiation are called organs at risk (OARs). Many OARs have a defined upper limit of the dose they can tolerate, and limitations are set on the dose to these organs. If the dose deposition exceeds this limit the organ can lose its function, and the end results can, at worst, be fatal. Some examples of common OARs important in this thesis are lens of the eye, brainstem, parotid glands and spinal cord.

## 2.5 Dose computation

Today it is common to use the electron density information from CT images to calculate the dose distribution for a patient. The dose calculation computes the energy absorbed by the media. Various physical processes may occur and must be taken into account by the algorithm. A good algorithm must take into account the various physical processes that may occur, but also needs to be fast enough to be used in the clinic. However, high accuracy must be balanced against speed.

The Monte Carlo (MC) dose calculation is considered to be the most accurate algorithm and used as a benchmark to check the accuracy of other dose calculation algorithms [Tertel et al. (2010), Aarup et al. (2009)]. The accuracy of the MC algorithm is very accurate because it simulates all the real physical processes using interaction probabilities to determine the fate of each particle. However, it is very time-consuming and requires large processing capabilities.

Faster dose calculation algorithms that are more commonly used in the clinic today are Pencil Beam (PB), Collapsed Cone (CC) and Analytical Anisotropic Algorithm (AAA). These algorithms are based on the calculation of TERMA (total energy released per mass unit) combined with energy deposition kernels. TERMA represents the distribution of the primary energy deposited in the absorber. RayStation 4.7 uses the collapsed cone algorithm for photon dose calculation and performs the calculation in three steps: energy fluence computation, TERMA computation and point spread kernel tracing. (**chapter 2.5.5** for description of point kernels.) To be able to calculate different quantities needed for the dose computation the three dimensional human body needs to be discretized. A 3D grid of cubic voxels of equal size is therefore made (**fig. 2.20**), called the dose grid, and the 3D dose can then be computed for the center point of each voxel.

### 2.5.1 Collapsed cone algorithm

The collapsed cone algorithm is based on the tissues' composition and the energy fluence of the photon beam to calculate the distribution of the energy released in the patient [Ahnesjö (1989)]. This is calculated by using a convolution-superposition method: a convolution is done between the TERMA with a superposition of sphere point kernels, finding the dose contribution (**fig. 2.18**). TERMA is calculated from the photon fluence, while the sphere point kernel describes the energy distribution in a 3D spherical grid of the patient.

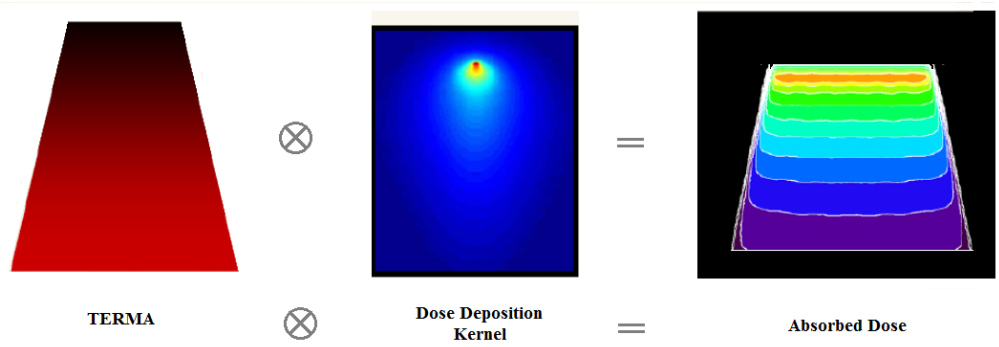


**Figure 2.18:** The absorbed dose is calculated taking the convolution between the TERMA and the dose deposition kernel. Figure taken from a presentation in the course FY8409 at NTNU.

### 2.5.2 The energy fluence computation

The fluence of a beam is defined as the number of photons that enter a voxel in the dose grid. The photons are created in a Bremsstrahlung process which occurs when the electron beam hits the primary target inside the linac head (primary source). Photons of different energies and directions then pass through a flattening filter (secondary source) where the beam is attenuated creating a flatter dose distribution, before the photon fluence is shaped by the collimators (y-jaws and MLC leaves). There are many interactions between the photons and the components in the linac head that must be accounted for in the dose calculation. The applicable geometrical parameters are set at the beam commissioning in RayPhysics, and some of the main parameters will be further described below: flattening filter, primary photon source, and MLC leaves.

The energy fluence is calculated by projecting the primary and secondary source through the collimators and onto the isocenter plane (fluence plane). The amount of monitor units (MU) is counted when the photon beam passes the ionization chamber in the linac head, and sets the global scale of the energy fluence computation and the dose calculation.

**Flattening filter (secondary source)**

The dose distribution is attenuated and flattened by the flattening filter, which is thicker on the beam axis and thinner at larger radii absorbing some of the low energy photons from the central part of the beam. The flattening filter behaves as a scatter source, also called the secondary source, and has a circular Gaussian intensity profile, with a large spot-size and a low intensity. In RayStation 4.7 several parameters are included to take into account the interactions in the flattening filter: the flattening filter photon source, an electron source, the off-axis softening, and a radially varying beam profile correction.

**Primary photon source**

The primary source is most commonly elliptical (as for Elekta) but may vary among vendors and among different linacs from the same vendor. The projection of extended sources through the collimators gives a non-uniform and field-size dependent energy fluence profile in x and y directions. The source's widths can be adapted in beam commissioning, but has not been changed in this thesis. The z-value is given by the source-axis-distance (SAD). For the primary source the spot-size is small and the intensity large, which is opposite as for the secondary source.

The part of the fluence that originates in the primary source is scaled with a radial beam profile correction. The total energy fluence is the sum of the primary Gaussian source projected through the collimators, multiplied with the beam profile correction, and the secondary photon source from the flattening filter without beam profile correction.

In the beam commissioning it is possible to change the weighting of each of the two sources, summing up to 1. This balance determines the sharpness of the penumbra, and influences the dose maximum of small fields.

### 2.5.3 MLC leaves

The collimators are modeled to be 2D instead of 3D in the energy fluence and dose computation. Several parameters are used to correct for this transition: tongue-and-groove parameter, leaf-tip width and fine tuning of the collimator position. These can be adapted in the beam commissioning to get a good fit between the measured and calculated dose distribution.

**Fig. 2.19** shows how the dose distribution curve (red curve) is influenced by the tongue-and-groove extent/tilit. The blue and orange MLC leaves represent two different segments with overlapping placement. The placement of the MLC leaves in the second segment (orange) starts where the first segments (blue) stops. An under-dosage occurs because of the shift in the penumbra due to the tongue-and-groove extent.

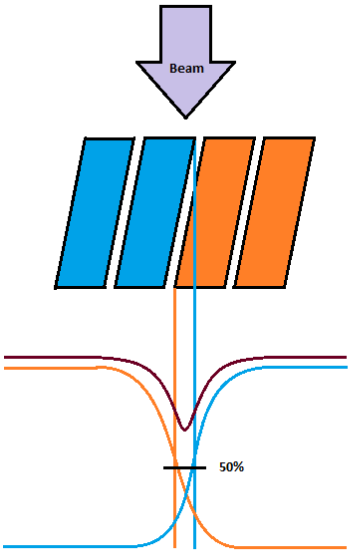


**Figure 2.19:** The penumbra of two following segments (blue and orange) giving rise to the total dose distribution (red curve). An under-dosage occurs in the line where the two segments overlap, which is due to the MLC shape (tilting) causing a tongue-and-groove effect.

### 2.5.4 TERMA computation

A set of calculations including densities, intersection lengths based on the energy, and material dependent mass linear attenuation are performed for each intersected voxel in the dose grid (**fig. 2.20**). The dose grid resolution was set to 0.30 cm/voxel, as used in the dose calculation for clinical treatment plans at St. Olavs Hospital. To compute the TERMA the energy fluence is used, being traced from the primary source to the patient surface and into the patient, taking inhomogeneities into account.

For a photon beam traveling through the patient body the photons that have not interacted follow a negative exponential curve, decreasing with depth. The first interaction for MeV photons in the body is most likely a Compton scattering: the primary photon interacts with an electron in the material, releasing this electron and scattering a lower energy photon. For 6 MeV photons, the free electron will release its energy locally mainly through ionizations, but the secondary photon will travel further portioning the energy deeper inside the body. TERMA is defined as the product of the linear mass attenuation coefficient, $\sigma$, and the energy fluence [Kron et al. (2012)], and depends on the material (spatial dependence) and energy:

$$TERMA(r) = \int \frac{\mu(r,E)}{\rho_m(r)} \cdot \Psi_r(r,E)dE \tag{2.4}$$

The linear mass attenuation coefficient is composed of the four physical effects; coherent scattering, photoelectric effect, Compton scattering and pair production: $\sigma = \sigma_{PE} + \sigma_{PP} + \sigma_{Compt}$, and

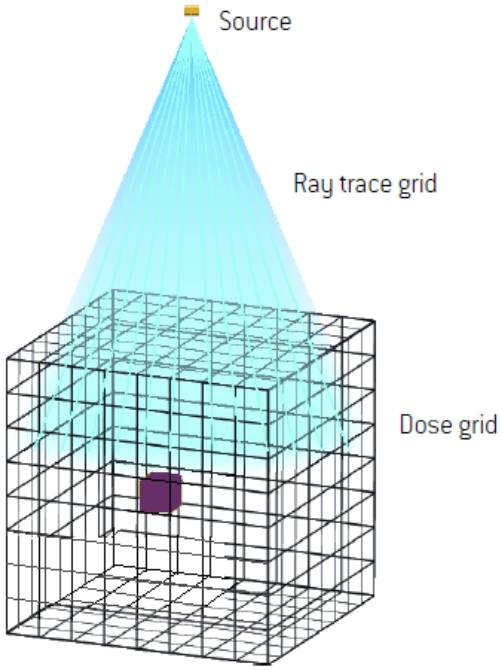


**Figure 2.20:** Illustration of the discretizing of the human body in a 3D grid of cubic voxels called the dose grid. Each ray in the ray trace grid from the primary source is followed and a set of calculations is performed for each intersected voxel. The purple box represtents one single voxel in the dose grid. Modified picture taken from Laboratories (2012b).

represents the probability of interaction. $\Psi$ is the energy fluence.

### 2.5.5 Point spread kernels

The sphere point kernel describes the statistical energy distribution in a 3D spherical grid of the patient around a primary photon interaction point, **fig. 2.21**. The kernels are pre-calculated using Monte Carlo simulations, one simulation per energy level. The photon dose is thereby computed as a two-step process with beam photon interactions leading to TERMA and further spread of secondary particles using the point spread kernels.

### 2.5.6 Dose computation for VMAT

A VMAT plan is separated into segments that present the region at a control point (CP). VMAT consist of CPs that are uniformly distributed throughout one or more arcs, commonly with a separation of 2-4 degrees. At St. Olavs Hospital the commissioned treatment machine has 4 degrees between each CP, though this may be changed in the beam commissioning to 2 or 3 degrees separation. The segment may be sub-divided if the leaf motion exceeds 1.5 cm. In this case, the

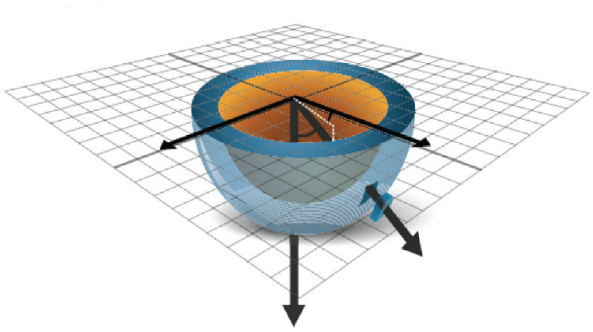

**Figure 2.21:** The point spread kernel describes the spatial energy distribution resulting from a single photon interaction [Laboratories (2012b)].

segment will be divided into sub-segments of equal length and with a maximum leaf travel of 1.5 cm [Laboratories (2012b)]. **Fig. 2.22** shows how a segment is divided into three sub-segments (green segments marked with 1, 2 and 3 in **fig. 2.22**) for a leaf travel of 3 to 4.5 cm. The MU of the segment is distributed over the sub-segments, and the fluence of each sub-segment is calculated and summed at the center position of the segment (at the red marker in **fig. 2.22**). The CC dose is based on the summed fluence and computed at the dose computation point (red marker in **fig. 2.22**).

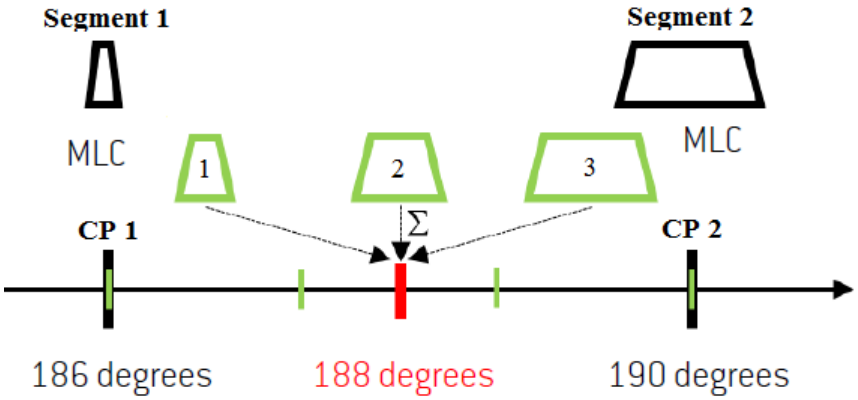


**Figure 2.22:** The creation of three fluence computation sub-segments (green) to obtain a maximum 1.5 cm leaf travel within each sub-segment. A fluence computation is performed for each interpolated MLC shape and summed to the dose computation point (red marker) [Laboratories (2012b)].

## 2.6 Dose volume histogram

A dose volume histogram (DVH) relates the radiation dose to a volume of interest within a 3D radiation therapy plan [Drzymala et al. (2009)]. In RayStation the DVH view represents a cumulative DVH meaning that a volume receives a dose that is equal to or higher than a certain level. The dose is expressed in gray (Gy) and the volume in %. The dose parameters represent the minimum dose to a volume $V$, given by $D_V$.

Definition of doses [Levitt et al. (2012)]:

- $D_{2\%}$ (near $D_{max}$) is the dose level that maximum 2 % of the specified ROI volume receives.
- $D_{50\%}$ (median) is dose level that 50 % of the specified ROI volume receives, meaning that equal volumes get lower and higher dose.
- $D_{98\%}$ (near $D_{min}$) is dose level that minimum 98 % of the specified ROI volume receives.

Considering clinical relevance the $D_{2\%}$ and $D_{98\%}$ are used rather than $D_{min}$ (lowest dose) and $D_{max}$ (highest dose). This is because $D_{2\%}$ and $D_{98\%}$ are not that sensitive to the dose grid placement and resolution, and because 2 % of the volume may be smaller than a voxel of the dose grid (**chapter 2.5.4**). DVH summarizes information about a non-uniform dose distribution and is used for quantitative evaluation of treatment plans, prescribing and reporting doses. However, a big drawback is the loss of spatial information resulting from the condensation of data when DVH is calculated, e.g. about the location of low- or high-dose regions [Podgorsak (2005)]. **Fig. 2.23** shows a cumulative DVH for selected ROIs: orange is an OAR and blue is a PTV. The $D_{2\%}$, $D_{50\%}$ and $D_{98\%}$ are indicated with white lines for the two volumes. A steeper curve, as for the PTV, indicates a more homogeneous dose distribution within the volume.

## 2.7 Treatment planning system

The treatment planning system (TPS) plays an important role in the accuracy of the dose calculations and creating a treatment plan that achieves tumor control and spares normal tissue. A complex plan of how the therapy system will deliver radiation is developed including, among others factors, calculations of expected dose distribution in different types of tissue, avoiding critical structures. There are a variety of TPS, each one having its own characteristics. The software system used at St. Olavs Hospital is RaySearch, as will be further described.

### 2.7.1 Plan optimization

After the clinical volumes have been delineated in the patient CT-images, the radiation beam settings must be set, including type of treatment modality, number of radiation arcs/beams with accompanying gantry angles, radiation output (photons/electrons), and beam energy. The optimization functions are then added to the treatment plan assigning dose requirements to the ROIs with

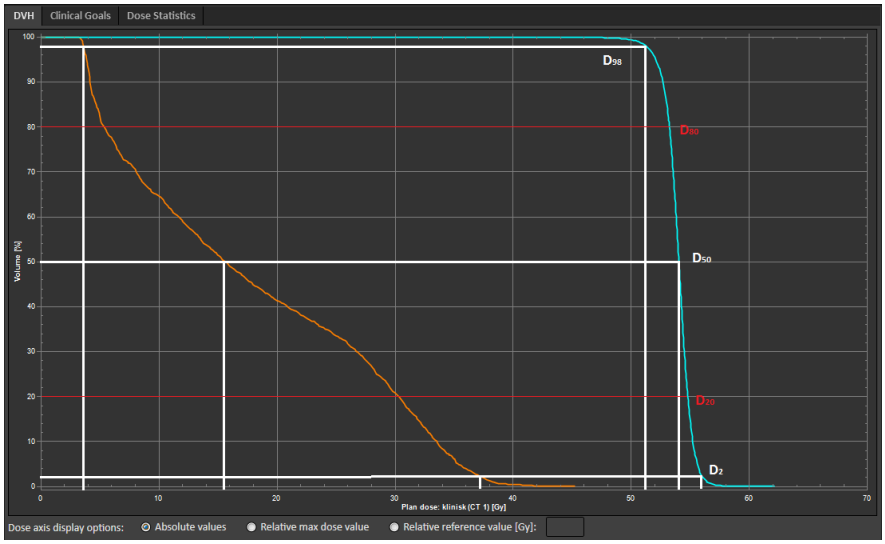


**Figure 2.23:** DVH for selected ROIs: orange dose curve is an OAR and blue is a PTV. Indicated are the three dose parameters $D_{2\%}$, $D_{50\%}$ and $D_{98\%}$, and the $D_{20\%}$ and $D_{80\%}$ that delineate the penumbra region [Laboratories (2012b)].

accompanying weighting factors. After the desired optimization functions are added, an optimization algorithm is run to obtain the desired dose distribution.

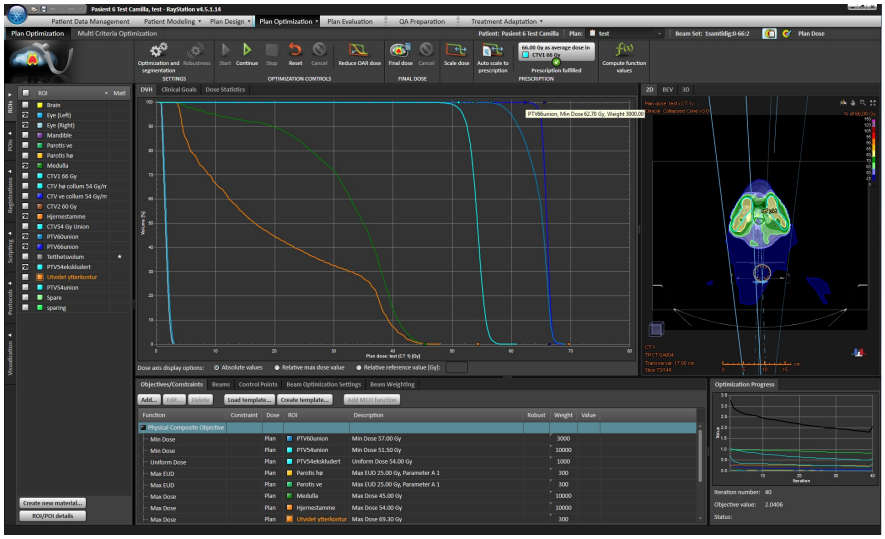

**Figure 2.24:** Workspace of the Plan Optimization tab. The selected ROIs in the DVH can be viewed in the list to the left. The added constriants are in the lower window, the BEV is in the right window, and the optimization progress is in the lower right window.

**Fig. 2.24** shows the workspace in the Plan Optimization tab of RayStation. The objective functions are listed in the lower central window, the DVHs after computation of the final dose are in the

central window, the ROIs are listed in the left window, the image set data in 2D (3D or BEV can also be selected) is in the top right window, and the optimization progress in terms of function values per iteration is in the lower right window.

### Iteration process

In the optimization process a maximum number of iterations can be selected to increase the process time. An iteration process is a procedure of repeating a sequence of computer instruction to get closer to a desired result. The optimization algorithm is divided in two phases [Manual (2012)]. The first phase is an optimization of a fluence map from each beam direction, and the second is a conversion of this map to segments. These segments are then optimized until the desired solution is achieved or the maximum number of iterations is reached.

### Constrain leaf motion

For VMAT it is possible to limit the leaf travel distance per degree of gantry motion (cm/deg). This is to assure that the differences in MLC positions between consecutive control points do not change dramatically, which may affect the accuracy of the dose computation. At St. Olavs Hospital, and for this thesis, the constrain leaf motion is set to 0.5 cm/deg (= 2 cm/4deg).

### Weighting of objective functions

Dose treatment plans are generally designed to administer a high dose to the target volume and an acceptable low dose to the normal tissue and OARs. For a plan to be clinically acceptable it is critical that the demands for the doses to the PTV and the OARs are fulfilled, or within a certain limit. Therefore, the critical PTVs and OARs are weighted high relative to other volumes. The value of the weighting determines the relative priority of the constraint to be fulfilled.

### Algorithm for plan optimization

The different target volumes, their prescribed doses and displacement are determined by the medical doctor, while the constraints (dose and weighting) for the different volumes are applied by the radiation therapist. The final plan is based on individual opinions, meaning that for the same patient case different clinically acceptable plans can be obtained.

A common algorithm for a plan optimization in RayStation is as follows: add the desired objective functions (including wanted ROI, its dose and relative weighting, **fig. 2.25**), start the optimization process with the accompanying number of iterations, and compute the final dose for the objective functions. When computing the final dose, the number of MUs sets the absolute scale for each beam. If the dose distributions were not satisfactory the optimization process can be continued either without any change or by adding/removing/editing objective functions and then continuing the optimization processes based on the already completed optimization. Because the optimization process proceeds from the already completed optimization, the order of adding/removing/editing

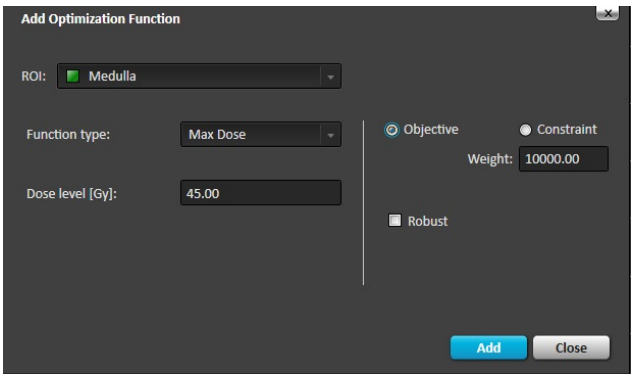


**Figure 2.25:** The box Add Optimization Function in workspace Plan Optimization in RayStation. Here the selected ROI is Medulla with function type Max Dose and dose level 45.00 Gy, with relative weighting 10 000.

objective constraints influences the final dose distribution. In RayStation this order is not listed, and it is therefore not possible to compare orders of the adding/removing/editing objective functions for different treatment plans.

### 2.7.2 Scripting

Scripting in RayStation can be used in the clinical practice to simplify the daily tasks. Scripts can read and write all data in RayStation. It can get and/or set values of properties for an object, and perform an action on an object. The scripting language is IronPython that is a python variety allowing access to .NET. A script is either created using a recording function that records the action being done in RayStation, made in an external editor and imported to RayStation, or may be run through the interactive console in RayStation for direct programming.

### 2.7.3 RayPhysics

Using RayPhysics, LINAC geometry settings can be set, and beam commissioning, CT commissioning and beam 3D modeling activities can be performed. Evaluation can be obtained of machine models and treatment plans for real patients before being commissioned for clinical treatment.

The Fluence tab contains parameters, physical and non-physical, used in the dose computation. Some of the parameters are given by the machine vendor, other need to be set to a value matching the measured dose as good as possible. An overview of the Fluence tab, including some of its changeable parameters, is shown in **fig. 2.26**. The graphic representation in this figure is the dose curves in the x-direction of different field sizes and for different depths, as a function of the position. A total of eleven field sizes are present, ranging from 1x1 $cm^2$ to 40x40 $cm^2$, each with four different depths (1.5 cm, 5 cm, 10 cm and 20 cm).

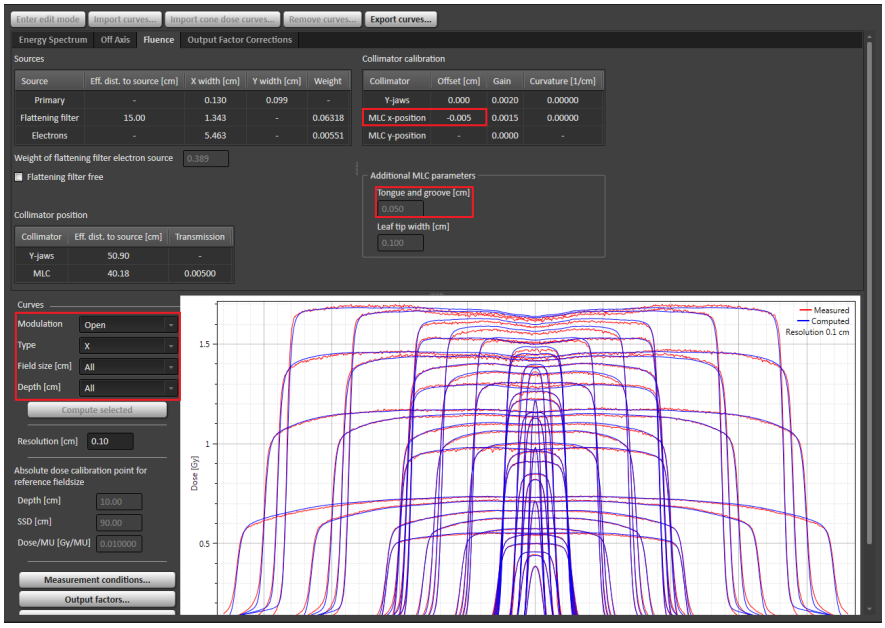


**Figure 2.26:** The Fluence tab in RayPhysics showing editable parameters. The graphical representation is the dose curves using the Modulation Open, the Type X, the Field size All, and the Depth All (as indicated in the red box). Here a comparison of the measured (red curve) and computed curves (blue curve) is done by chaniging the geometric settings of the linac to achieve a good coorespondanse between these two. The two changed geometrical parameters done in this thesis are also indicated in a red box, the *MLC x-position* offset and the *Tongue and groove* offset.

The **output factor** (OPF) represents the correspondence between the doses on the central axis to a specified number of measured beam MUs. OPF varies with the field size due to the photon scatter and head scatter, and usually increases with the field size due to the extra contribution from the secondary scattering. OPF is calibrated so that 1 cGY/MU is delivered at 100 SSD for a field size of 10 x 10 $cm^2$ (as is the case for the clinical treatment machine at St. Olavs Hospital) The OPF has influence on the measured dose curve normalization but is not part of the beam model used in dose computation.

**Penumbra**: The *MLC x-position* parameter in the Fluence tab has effect on the penumbra of the dose curves (red box in **fig. 2.26**). The penumbra is shifted farther away from the central axis as the MLC offset increases, resulting in an enlarged field opening/size. For a VMAT field, a small adjustment of the MLC offset, and thereby the penumbra position, may have a significant influence on the overall dose level. This is because a VMAT plan consist of a summation of all the segments, resulting in a significant contribution to the total dose distribution.

**Tongue-and-groove**: The *tongue and groove* parameter in the Fluence tab (red box in **fig. 2.26**) is the size of the region centered at the leaf side. The transmission has been modeled to be the square root of the MLC transmission [Laboratories (2012a)], and will be twice the size because the parameter will be added on both sides of the MLC leaves.

Chapter 3

# Materials and methods

## 3.1 Patient selection

After the transition from Oncentra MasterPlan to RayStation TPS at St. Olavs Hospital (spring 2015) a dosimetric verification was done of the first 66 patient plans with the Delta4 phantom. The 9 patient cases with poorest verification outcome were selected and has been further studied in this thesis. Among these 66 clinical cases the diagnosis were distributed as follow: 25 with cancer pelvic with lymph nodes and 9 without lymph nodes, 11 with cancer in part of the brain, 16 within otolaryngology, and 5 with cancer in the abdomen. **Tab. 3.1** shows the 9 selected patient cases together with the corresponding diagnosis, verification values (median to the dose deviation, $\gamma$-index), total amount of MU and which linac the QA was done on.

**Table 3.1:** Data set from the clinical treatment plan: $\gamma$-index, median to the DD, total amount of delivered MU/fx (monitor units per fraction).

| Patient | Diagnosis | Median (%) | $\gamma$-index (%) | Total MU (MU/fx) | QA done on linac |
|---|---|---|---|---|---|
| 1 | Otolaryngology | 1.9 | 90.2 | 493.78 | SB3 |
| 2 | Part of brain (frontal lobe) | 1.4 | 92.0 | 404.90 | SB2 |
| 3 | Otolaryngology | 2.0 | 92.5 | 470.93 | SB6 |
| 4 | Abdomen (esophagus) | 1.2 | 99.3 | 549.23 | SB3 |
| 5 | Otolaryngology (floor of mouth) | 1.5 | 94.0 | 553.09 | SB3 |
| 6 | Otolaryngology (uvula) | 1.9 | 94.9 | 499.93 | SB3 |
| 7 | Otolaryngology (lips) | 1.1 | 96.1 | 426.17 | SB4 |
| 8 | Otolaryngology (tonsil) | 1.4 | 96.2 | 472.78 | SB2 |
| 9 | Otolaryngology (tonsil) | 1.4 | 96.2 | 490.00 | SB2 |

## 3.2 Medical oncology software

### 3.2.1 Delta4 phantom

At St. Olavs Hospital the Delta4 phantom from ScandiDos is used to verify the prescribed dose delivered to the patient, and can be used for different treatment modalities. **Fig. 3.1** shows the presentation of the phantom as the patient body, receiving the delivered dose at gantry angle 182° with respect to the coordinate system described in **chapter 2.1.3**.

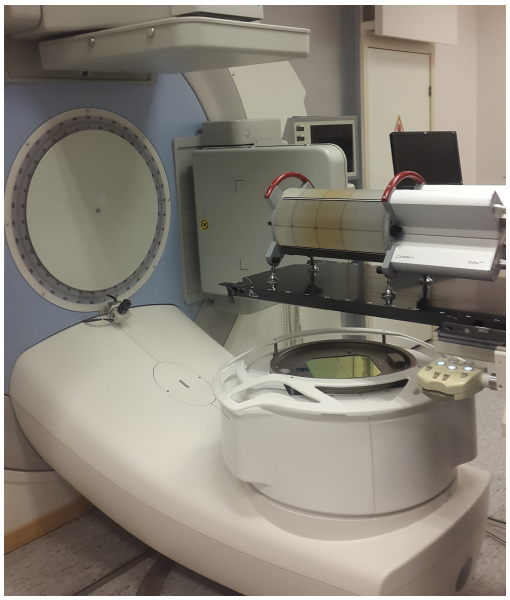

**Figure 3.1:** Setup of the Delta4 phantom representing the human body. Gantry angle is here at 182°.

#### Setup

The Delta4 phantom has alignment guides to get a precise position of the isocentre. Three laser guides positioned in the treatment room are defining the isocentre. The phantom is manually placed so that the lasers are within the guidelines, ensuring an agreement of $< 1$ mm, as shown in **fig. 3.2**. The cylindrical PMMA phantom is connected to the treatment machine in order to synchronize the measurements taken with the radiation pulses emitted from the linac.

#### Delta4 software and quality assurance

A quality assurance (QA) is instantly analyzing treatment plans for approval. The QA preparation is obtained by exporting a verification plan via DICOM to the Delta4 software. The verification plan is created in the TPS by recalculating the original patient plan onto the cylindrical Delta4

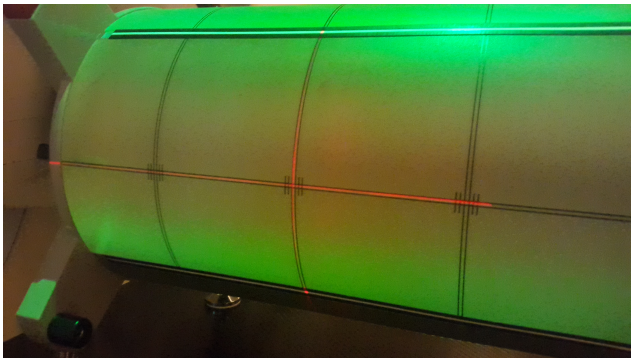

**Figure 3.2:** The alignment of two of the three lasers in the treatment room, placed within the phantom's guidelines.

phantom.

The measured dose obtained by the phantom is reconstructed to a full volumetric dose computed by the Delta4 software. The 3D dose distribution can then be compared with the calculated dose checking the assurance between the DD, DTA and the gamma-index. The setup window for the Delta4 software is shown in **fig. 3.3**. Here the measured dose is represented by the two orthogonal detector planes of the phantom, indicating the dose level at each detector. The three evaluation methods available in the Delta4, presented at the bottom of **fig. 3.3**, are DD, DTA and gamma evaluation. The selected criterion for each of these is presented as a red vertical line in the histograms: 3 % deviation in the local dose, 3 mm spatial deviation and at least 90 % of the detectors must have a gamma-index of $\leq 1$. A cutoff limit has also been used that only includes points receiving at least 50 % of the maximum dose. These criterions are being used in the clinic today to assure that the clinical impact of radiation delivery errors are within an acceptable low level.

### 3.2.2 RayStation

RayStation is a software program for radiation treatment planning. Volumes of interest in the body, together with certain demands of the dose delivered to the volumes, are added to the treatment plan. RayStation tries to find the optimal solution, with the given objects and constraints. Dose calculations are based on the collapsed-cone algorithm (see **chapter 2.5.1**).

#### Dose volume histogram

A dose volume histogram (DVH) relates the radiation dose to the ROI, and summarizes a 3D dose distribution in a graphical 2D format. A comparison of different plans for the same patient can be done in the Plan Evaluation workspace in RayStation (**fig. 3.4**). Information of the selected plans is here compared, making it easy to evaluate two or three different plans relative to each other for a specific patient. In **fig. 3.4** the DVH is visualized in the upper right window, but may be switched to obtain other information of the treatment plans. The two windows in the middle of **fig. 3.4** are

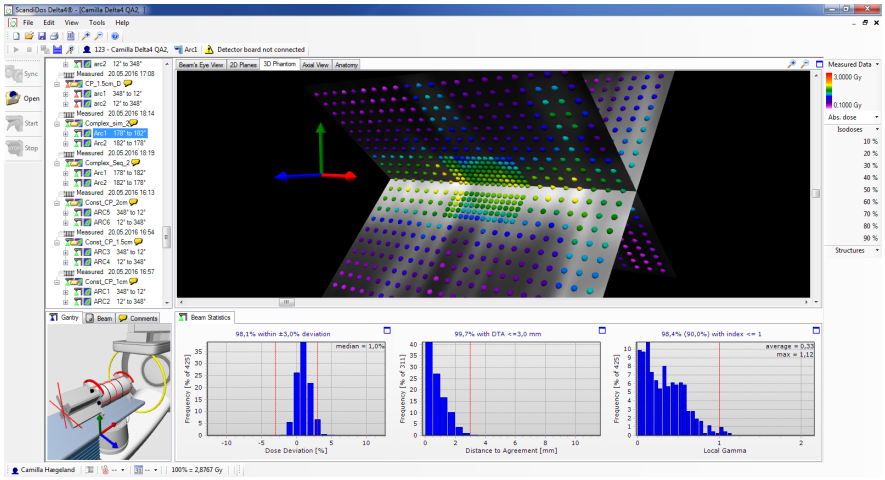

**Figure 3.3:** The upper panel shows the two crossing plans of diodes in the phantom and the amount of dose received at each detector. The lower panel shows the histograms of the dose difference, distance to agreement, and $\gamma$-index for the measured dose, with respect to the planned dose. The red vertical lines in the histograms indicate the selected pass/fail criteria for the verification values: 3 % deviation in the local dose, 3 mm spatial deviation and at least 90 % of the detectors must have a gamma-index of $\leq 1$ for a plan to be verified.

showing each of the dose distribution to the plans, while the lower right window shows the dose distribution difference between the two plans.

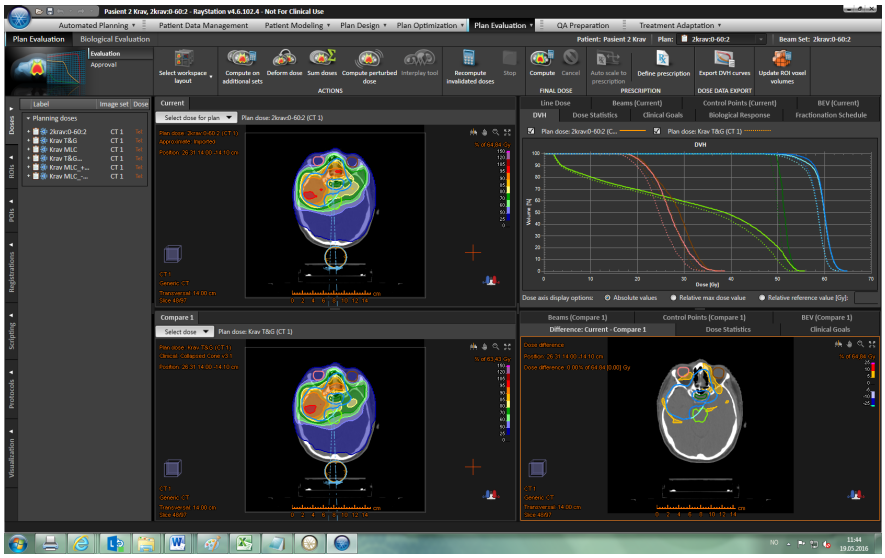

**Figure 3.4:** Comparison of two different plans of patient case no. 2, in the Plan Evaluation tab in RayStation. The dose distribution for each of the plans is shown in the middle windows, and the difference of these dose distributions is presented in the lower right window. Difference in the DVH are showed in the upper right window.

### Clinical approval

After the optimization of the object functions is completed the plan needs to be clinically approved. To achieve a clinical approval by the medical physicist it is especially important that the critical PTVs achieve at least the minimum dose required, and that the dose to the critical OARs not exceed the tolerance dose limit. **Fig. 3.5** compares two treatment plans; both are approved but the (- - - - -) plan-curve is preferred due to lower dose levels to the OARs, while the dose levels to the PTVs are approximately the same.

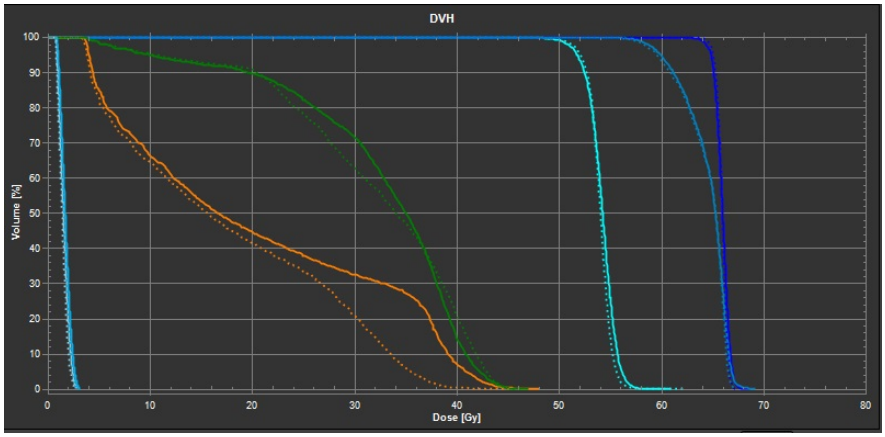


**Figure 3.5:** Comparing the dose distributions of two different plans of the same patient. (- - - - -) plan-curve is preferred over (——) due to the lower dose to the OARs (green, orange and left blue dose distributions). The dose distribution to the PTVs are approximately the same for the two plans (the 3 blue curves to the right).

## 3.2.3 Mosaiq

Mosaiq is a medical oncology software that provides documentation of patient information and is used to control the radiation treatment, provided by Elekta [Software (2010)]. Support of document scanning and import makes it possible to import DICOM and DICOM RT, and thereafter radiation oncology plans. An accurate treatment prescription can be created together with a review and approval documentation. A patient plan has certain control points for the treatment field. A control point is a specific point at which the Mosaiq system controls that the linac parameters, i.e. gantry and collimator angles together with MLC and collimator positions, is correct and that the correct amount of MUs are delivered. The control points must be achieved for the dose delivery to take place.

## 3.3 Algorithm for plan optimization

A basic algorithm for optimizing a treatment plan is described in **Background 2.7.1**, resulting in an individual optimization algorithm. To keep track of the adding/removing of objective functions two new treatment plans were made, for each of the eight clinical patient cases, with a specific order regardless of the original optimization sequence of the clinical treatment plans. Both the new plans had the basic sequence: an optimization with 20 iterations was followed by a final dose calculation, which was done three times for each plan.

**Simultaneous optimization**:
All the volumes and their constraints were included before the first optimization, and were not changed during the remaining optimizations and final dose calculations.

**Sequential optimization**:
Including only the target volumes with accompanying constraints for the first optimization sequence and final dose computation. The OARs were added for the remaining two sets of optimization and final dose computation, including all the constraints of the treatment plan.

## 3.4 Scripting in RayStation

Scripting in RayStation can be used to get and/or set values of properties for an object, and perform an action on an object. In this thesis two main types of scripts have been made: 1) the MLC positions were changed to achieve a wanted leaf movement/placement, 2) treatment plans were analyzing based on extract information, mainly from the placement of the MLC leaves. (Recall **chapter 2.1.4** for the definition of the MLC leaf position.) All the used scripts are included in the appendix. CT-images of the Delta4 phantom were used for dose calculations of the created script-plans with specific MLC positions. The only objective functions added were a cylindrical PTV and the outer contour of the phantom (**fig. 3.6**). The constraint to the PTV was set to 48.0 Gy as minimum dose with weighting 10 000, and to the outer contour was a dose fall-off from 50.0 Gy to 25.0 Gy with weighting 300.

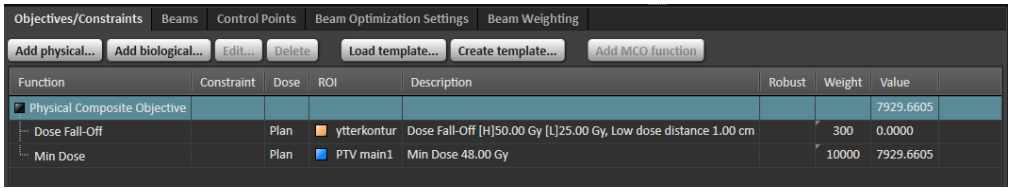


**Figure 3.6:** Overview of the added objective functions used by the script-plans.

### 3.4.1 MLC position

The definition of the MLC position in the x-y plan is defined as the placement of the MLC leaf tip relative to the isocenter. When the edge of the MLC leaves is positioned to the right of the isocenter axis, its position reading value is positive, while to the left the value is negative. Referring to an specific MLC leaf the notation leaf_positions[i][j] will be used. i indicating the left or the right MLC leaf bank taking the values 0 or 1, respectively. j is the number of the MLC leaf pair going from 1 to 80. E.g. in **fig. 3.7** the MLC leaf pair no. 51 of the right MLC bank (i = 1) takes the value 0.56 cm (x-direction) and is presented as leaf_positions[1][51] = 0.56 cm, and the left MLC bank takes the value -2.91 cm presented as leaf_[0][51] = -2.91 cm.
The upper y jaw (Y2) is marked with blue in **fig. 3.7**, placed in the intersection between MLC leaf no. 56 and 57. Its position is 8.0 cm (y-direction) above the isocenter.

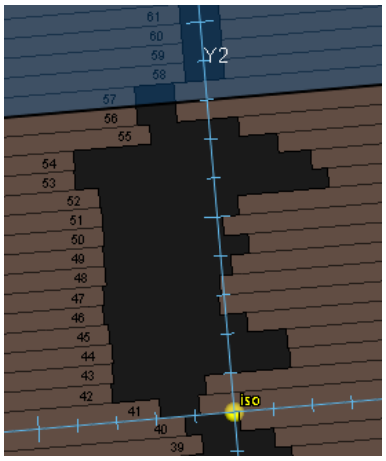


**Figure 3.7:** The numbering of the MLC leaf pairs presented on the left MLC bank. The limitation by the upper y-jaw (Y2) is marked with blue, placed 8 cm from the isocenter (iso).

### 3.4.2 Selection of specific MLC positions

#### Finger-pattern MLC shape

A plan consisting of many MLC flanks was needed to test the tongue-and-groove effect. The script that provokes MLC flanks is based on an open field (20 cm x 27 cm) where MLC leaves are systematically placed to the opposite side, making a finger pattern (**fig. 3.8**). The amount of MLC leaves moved over to the other side can be selected in the script. In this thesis the number of MLC leaves moved to the opposite side have been selected to 1, 2 and 4 MLC leaves, resulting in a width of the MLC protrusion of 0.5 cm, 1 cm and 2 cm, respectively (1 MLC leaf width = 0.5 cm, called 1LP). **Fig. 3.10** illustrates these three plans. The MLC positions were kept fixed during the whole beam arc. Start and stop gantry angle was set to 178°/182° giving a gantry rotation of 356°, accompanied with 90 segments.

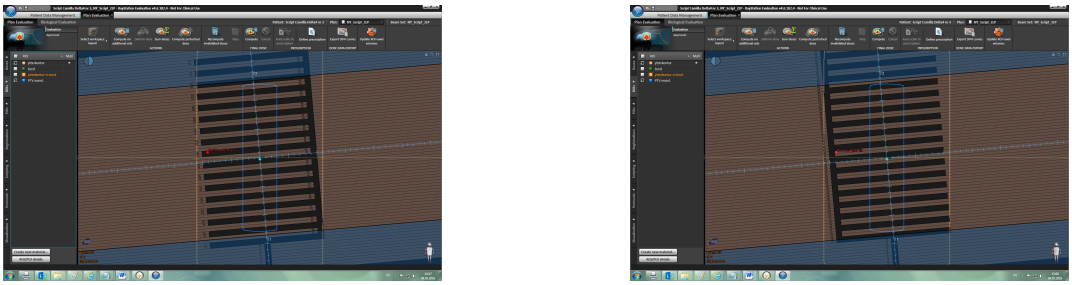

**(a)** First arc. **(b)** Second arc.

**Figure 3.8:** A plan, checking the T&G effect, consisting of two beams with opposite placement of the MLC finger-pattern of width 1 cm, resulting in an open field opening of size 20 cm x 27 cm.

The plans consisted of 2 arcs with overlapping MLC positions. The open region in the first arc was covered by the MLC protrusion in the second arc, totally covering a field area of 20x27 $cm^2$. **Fig. 3.8** shows a MLC protrusion with 1 cm width (2 MLC leaves, plan 2LP), and how the second beam (**fig. 3.8b**) has overlapping MLC protrusions relative to the first beam (**fig. 3.8a**).

The overlap of the MLC openings between different beams was set so that the MLC flanks will occur in the same line. The dose distribution should then become even, also in the radial direction, due to the fact that the MLC openings of the beams sum up to an open MLC field opening. Though, this is not the case because of the tongue-and-groove effect, which is due to the shape of the MLC leaves. This effect has further been studied using the three plans with different finger-pattern-widths.

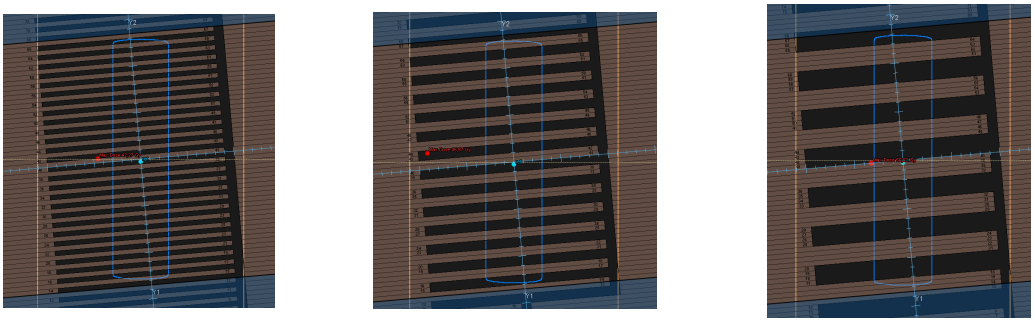

**(a)** 0.5 cm (1LP) **(b)** 1 cm (2LP) **(c)** 2 cm (4LP)

**Figure 3.10:** Illustration of three plans with finger-pattern of different protrusion widths, seen from the BEV.

### Dynamic MLC movement

A script was made setting both MLC leaf banks in a line with a fixed opening between them. From one segment to the next, the leaf banks were moved a certain distance, resulting in a dynamic movement of the arc with a fixed opening of the moving slit. The plans consisted of 1 or 2 arcs, where

for the plans with 2 arcs the second beam arc had the same dynamic movement as the first, only moving in the opposite direction.

**Fig. 3.11** represent one beam with 24 degrees gantry rotation consisting of 7 segments (4 degrees per control point). Here, the MLC opening is fixed to 2 cm and the MLC travel distance between two segments is 0.5 cm/deg (= 2 cm/4deg). The start position of the right MLC leaf-bank is $-7$ cm, with a travel distance of 0.5 cm/deg the end position (left leaf-bank) is at 5 cm. Totally the segments fully cover a continuous region from $-7$ cm to 7 cm, in the x-direction.

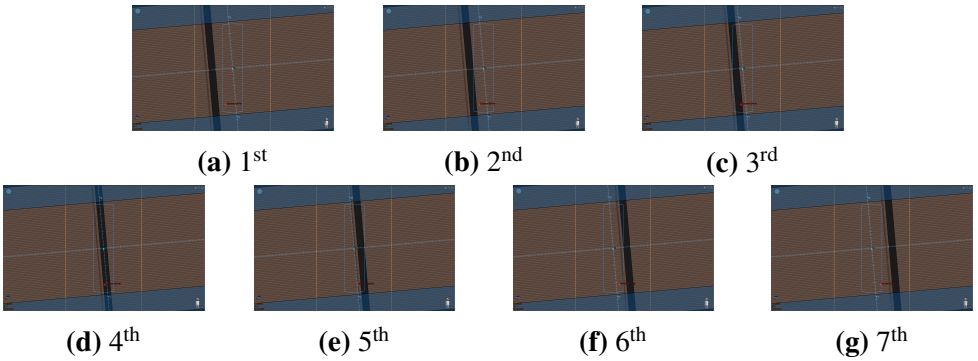

**(a)** 1st **(b)** 2nd **(c)** 3rd

**(d)** 4th **(e)** 5th **(f)** 6th **(g)** 7th

**Figure 3.11:** A plan with one beam consisting of 7 segments, where a fixed MLC opening of 2 cm moves 2 cm per segment (0.5 cm/deg).

Various selections of MLC openings (1 cm to 5 cm), MLC travel distance (0.25 cm/deg to 1.2 cm/deg) and number of beams (1 or 2) were combined to measure the dose distribution of the plans with dynamic moving MLC leaves. All the beams had start/stop angle of 348°/12°, unless otherwise stated in the text.

#### Static fields

Three plans were made with a fixed field size without MLC movement during the beam arc. The three different field sizes were 1.0 cm, 1.5 cm and 2.0 cm, which is the three smallest fields used in this thesis. The middel point of the field size was along the central axis. These plans were made to check the dosimetric accuracy of small field sizes. Each plan consisted of two arcs of 24° gantry rotation with middle point at 0°.

### 3.4.3 Scripts for plan information readout

For all the scripts that extract information a start and stop index were set in the y-direction at the position of the y-jaws (**fig. 3.7**). The start/stop index was found for each segment to assure that no MLC-information outside the y-jaws was included. The standard deviation of the MLC positions was also calculated, an average for each MLC leaf, for all the following scripts (included in appendix).

#### MLC opening

Concerning the field opening, the information of the MLC tips were extracted to find the distance between two opposing leaves, leaf_positions[0][j] and leaf_positions[1][j].

The main step of the script:
distances = [rp – lp for lp, rp in zip(leaf_positions[0][start:stop], leaf_positions][1][start:stop])]

leaf_positions[i][start:stop] is a sequence of the leaf positions between the leaf no. j = start and j = stop, for leaf bank i. rp and lp stands for right and left element in the 2-tuple created by the zip() function. The zip() function is a building python function that returns a list of tuples (here a 2-tuple), where the n-th tuple contains the n-th element from each of the leaf position sequences. lp represents the left leaf bank at first position in the 2-tuple, and its value is always smaller than the rp (right leaf bank). Hence, by subtracting lp form rp the MLC opening is found.

#### MLC travel distance

The MLC speed (cm/deg) is defined as the travel distance of the same MLC leaf between two subsequent segments (**chapter 2.1.4**). As for the MLC opening the zip() function was used to find this distance, but now between the same MLC leaf of subsequent segments.

The main step of the script:
distances = [abs(rp – lp) for lp, rp in zip(segments[k].leaf_positions[0][start:stop],
segment[k+1].leaf_positions][0][start:stop])]

k is the segment number, and k+1 is therefore the following segment. The absolute value of the left and right element in the 2-tuple must be applied because the leaf position [i][j] in segment k can be both negative/positive and/or smaller/larger compared to segment k+1.

### 3.4.4 MLC flanks

A MLC flank is where the long side of the MLC leaf is exposed to an open field (**fig. 2.6**). To find this distance one need to check how the neighboring MLC leaves are placed. Whether or not there is a difference in the MLC position between leaf [i][j] and [i][j+1], if the placement of leaf [0][j] is larger than [1][j+1], or [0][j+1] is larger than [1][j]. All combinations of these differences have been accounted for in this script. Also the amount of MLC "islands" was counted, which occurs when there is an overlap between the MLC leaves, happening when leaf_positions[0][j] > leaf_positions [1][j+1] or leaf_positions [0][j+1] > leaf_positions [1][j].

### 3.4.5 Robustness-index

Based on the previous scripts a robustness-index was suggested. The index was defined after numerical analyzes were done of the differences in MLC positions and studying the effect of different offsets. Parameters were high values make a treatment plan more vulnerable for external influences

were divided on parameters were low values make a plan more vulnerable, presented in **eq. 3.1**. A low *RI* (robustness-index) therefore corresponds to a robust treatment plan, meaning robust against external influences.

$$RI = \frac{\text{flank} \times \text{speed} \times \text{island} \times \text{MU}}{\text{opening} \times 1000}. \tag{3.1}$$

## 3.5 Creation of new machine models in RayPhysics

(The graphics for all the new treatment machines are presented in appendix.) Parameters of the machine geometry can be changed in RayPhysics. In this thesis some of the beam model parameters, the MLC offset and the tongue-and-groove parameter, were changed when creating new machine models. Dose calculations were done in RayStation for both the original clinical treatment machine and the new created machine model, and a comparison between these two machines was then obtained.

The original clinical treatment machine has MLC parameters: MLC x-position = -0.005 cm and Tongue and groove = 0.05 cm. **Fig. 3.12** shows the cross-plane dose curve profiles (in x-direction) for different field sizes as a function of position. The MLC parameters have been tuned to match the measured dose curves for different field sizes, at different depths.

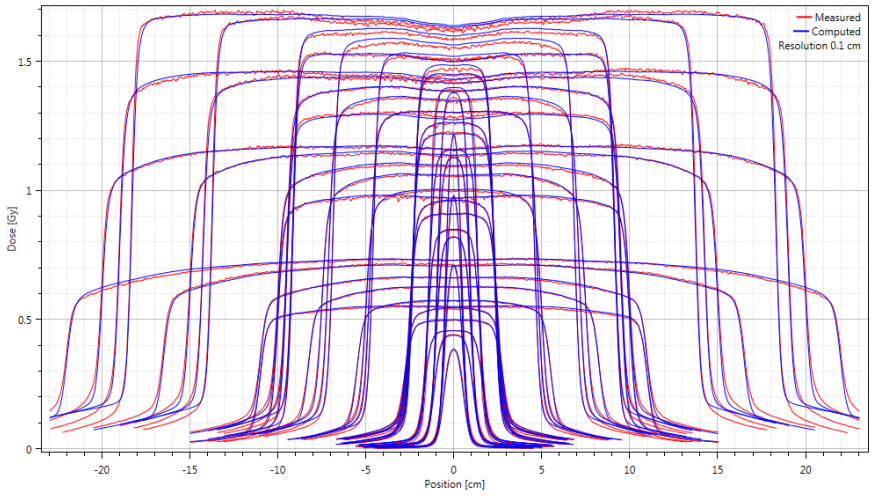


**Figure 3.12:** Cross-plane profiles, for different field sizes at different depths, showing the match between the measured (red) and calculated (blue) data in the RayPhysics modeling section.

### 3.5.1 Tongue and groove parameter

The tongue-and-groove calibration coefficient is defined at the projection onto the isocenter plane and may take values from 0.000 cm to 0.250 cm (half of the leaf width). In the new machine model

called *new_machine_T&G* the tongue-and-groove parameter was changed from 0.05 cm to 0.20 cm, meaning that the MLC leaf flange is expected extend further into the open field or, for the case of the Agility MLC model, the degree of tilting is expected to be larger.

### 3.5.2 MLC offset

The parameter MLC x-position in RayPhysics affects the MLC position which has an influence on the penumbra position (**fig. 2.6**). Three new machine models were made with different values of the MLC x-position, taking values of +0.200 cm, +0.100cm, and –0.100 cm, called *new_machine_2mm*, *new_machine_+1mm*, and *new_machine_-1mm*, respectively.

**Fig. 3.13** shows the dose distributions as a function of position (cm) presented for the measured and calculated dose profiles for the new machine model, with MLC x-position offset of 0.200 cm. Compared to the dose profiles in **fig. 3.12** the calculated penumbra is shifted further away from the central axis due to an increase in the field size when changing the MLC x-position from -0.005 cm to 0.200 cm.

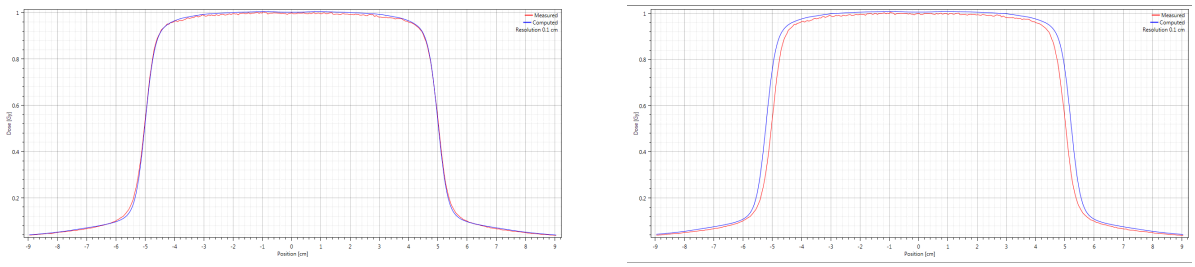

**(a)** MLC x-position offset = -0.05 mm

**(b)** MLC x-position offset = 2 mm

**Figure 3.13:** Graphical comparison of computed (blue) and measured (red) dose distribution (Gy) as a function of position (cm), for field size 10x10 $cm^2$ at 10 cm depth. The computed penumbra is shifted further from the central axis when the offset of MLC x-position is changed from -0.005 cm to 0.200 cm (an increment of the field size).

## 3.6 Plans checking the gravitation effect

Whether or not the gravitation force influence the MLC leaf movement could be checked by measuring the dose distribution for various gantry and collimator angles. Three gantry angles were chosen with two different collimator angles. The most exposed and deviating angles were chosen, taking the values 0°, 90° and 270° for gantry angles, and 0° and 90° for collimator angle. (Gantry angle 180° was not chosen due to limitations in the gantry rotation between $178° - 182°$.) With collimator angle 0°, at gantry angles 90° and 270°, the MLC leaves are at the most vulnerable stage with a travel distance direction along the direction of the gravitational force. For the same gantry

angles with collimator angle 90° the MLC travel distance direction is perpendicular to the gravitational direction.

The optimization process in RayStation was the same for the six plans, except for the values of the collimator and gantry angle. An optimization was followed by a script setting the MLC positions before the final dose was calculated. This sequence was done twice for the six plans. Each of the plans consisted of two arcs of 24°, the second arc going in opposite direction as the first, with middle point at the three gantry angles (0°, 90° and 270°), presented in **fig. 3.14**. The MLC leaf travel had a dynamic movement, as described in **chapter 3.4.2**, with 4 cm fixed MLC opening and 1 cm/deg travel distance.

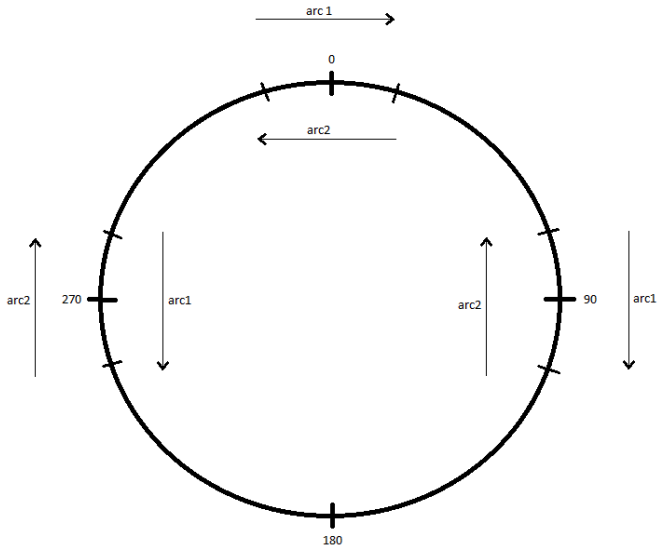


**Figure 3.14:** Directions of the two arcs with 24° gantry rotation and middle point at gantry angle 0°, 90° or 270°.

## 3.7 Diamond detector

A diamond detector is considered to be a good detector for measurements of photon beams with small field sizes, due to the small size, good spatial resolution and good tissue equivalence. Used in this thesis was the microDiamond detector type 60019 from PTW, with a sensitive volume of 0.004 $mm^3$ measuring the relative dosimetry. Photon depth-dose curves, normalized to the dose at a reference detector, were measured for three 3D-CRT plans with finger-pattern fields of protrusion widths 5 mm, 10 mm and 20 mm. Each plan consisted of two beams with overlapping field patterns

(**fig. 3.8b**). The reference was in a field opening for the first beam and in a field closure for the second. Therefore, the dose curves for the two beams (of the same plan) obtained a different reference and had to be normalized before being summarized, finding the total dose distribution. Information about the total absolute dose was therefore absent. Though, it was the shape of the penumbra region that was of main interest, and the information regarding the total dose was not needed.

## 3.8 Gafchromic film

Gafchromic EBT film (International Specialty Products, Wayne, NJ) is a self-developing dosimetry film used for accurate two-dimensional dosimetry, and was in this thesis used for measurements of the MLC flank and penumbra region. The film is near tissue-equivalent and composed of radiation-sensitive organic microcrystal monomers that react with the ionizing radiation, creating a blue polymer. The strength of the blue colour depends on the amount of delivered dose to the film. Darker blue indicates higher radiation dose. The dose range of the film is between 1 cGy to 800 cGy [Ashland (2005)].

The same three 3D-CRT plans as used for the diamond detector were also used for measurements on the EBT films, consisting of two segments with overlapping finger-print patterns and different protrusion widths (5 mm, 10 mm and 20 mm).

The set-up of the EBT film measurements followed the previous study by Saur and Frengen (2008). The films were placed in a SolidWater slab phantom at 3 cm depth with SSD of 100 cm. Irradiation of 6 MV photons was performed perpendicularly to the film. A calibration curve was made irradiating eight gafchromic films with a 10 x 10 $cm^2$ field with doses ranging from 0.2 Gy to 2.5 Gy. All the irradiated films were then scanned with the Epson Expression V750 Professional scanner (Seiko Epson Corporation, Nagano, Japan), a flatbed scanner with 6400 dpi resolution. The scanner consists of anti-reflective lens coatings and a high-reflection mirror providing a image of very good quality. It is important that the orientations of the films are the same during scanning because the polymers tend to align parallel with the coating direction of the film. The profiles used in this context were profiles along the scan direction, no correction for the nonuniformity response over the scanner area was therefore needed.

The software tool for dose verification and evaluation 418 VerA [Wasbø et al. (2005)] was used to read out the data from the scanned gafchromic films, obtain a calibration curve and compare the calculated and measured dose-profiles. **Fig. 3.15** shows the work-window of VerA, comparing the calculated dose-profiles from RayStation with the measured dose-profiles obtained from the scan of a gafchromic film.

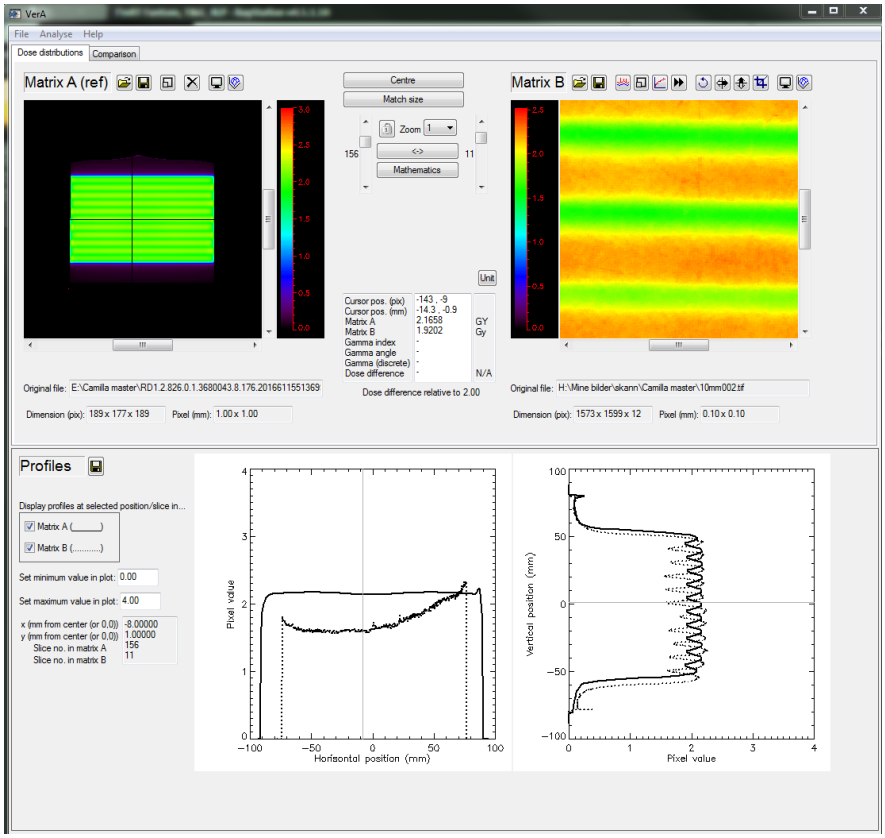


**Figure 3.15:** The software program VerA [Wasbø et al. (2005)] used to compare the scanned gafchromic films with the calculated dose distribution of the same plan in RayStation. The upper left window shows the calculated doseplan-matrise, and the upper right window shows a clipart of the scanned film. The horizontal (left) and vertical (right) dose-profiles are presented in the lower window. (——) is calculated dose-profile from RayStation and (.....) is the measured dose-profile from the gafchromic film scan.

Chapter 4

# Results

The present assignment builds on the project thesis done in the fall 2015 at St. Olavs Hospital [Hægeland (2015)]. Main results of the project thesis are included in the appendix. The two optimization sequences, sequential and simultaneous, were first made in the project thesis, and showed that the end result may differ depending on how the optimization process has been performed. For the sequential case the system was allowed to do an optimization without the OARs and the system was then able to set the base for the demands of the target volumes. By then continuing the optimization from the current state the system seemed to be able to keep the constraints of the target volumes while sparing the dose to the OARs. In this thesis the robustness of the two sequences was checked, by introducing different types of offsets. Also, information of the patient plans with the two sequences were extracted from the TPS and analyzed.

## 4.1 Optimization sequence

Three measurements were done of the eight patient plans with sequential and simultaneous optimization sequence to check the robustness against a physical MLC offset. The first measurement was without any calibration errors, while in the second two a physical MLC offset of +1 mm and -1 mm was introduced to each MLC bank creating a total gap error of $\pm 2$ mm. The three different measurements are presented in **fig. 4.1** (sequential plans) and **fig. 4.2** (simultaneous plans).

Without calibration error the sequential optimization had a slightly better verification value than the simultaneous, with average values of 99.6 % and 95.0 %. The sequential plan also showed a greater robustness against the introduced MLC offset of $\pm 1$ mm. A negative MLC offset (smaller field size) showed a better verification degree than a positive MLC offset (larger field size) for both the sequential and simultaneous plans, though a much greater difference for the simultaneous opti-

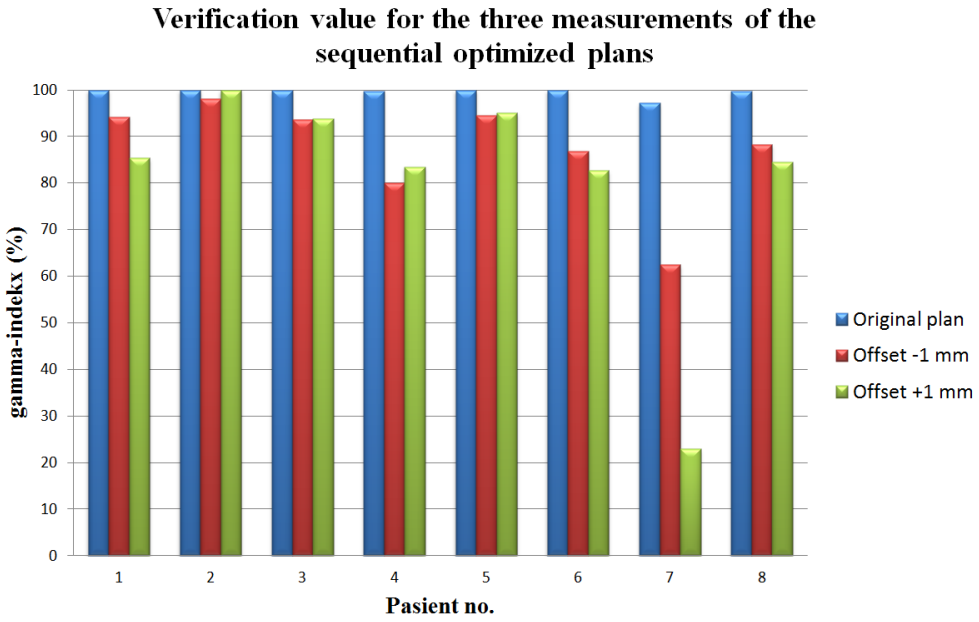


**Figure 4.1:** Comparison of the verification value of the three measurements, where no calibration error was included and $\pm 1$ mm MLC offset was included for the sequential optimized plans.

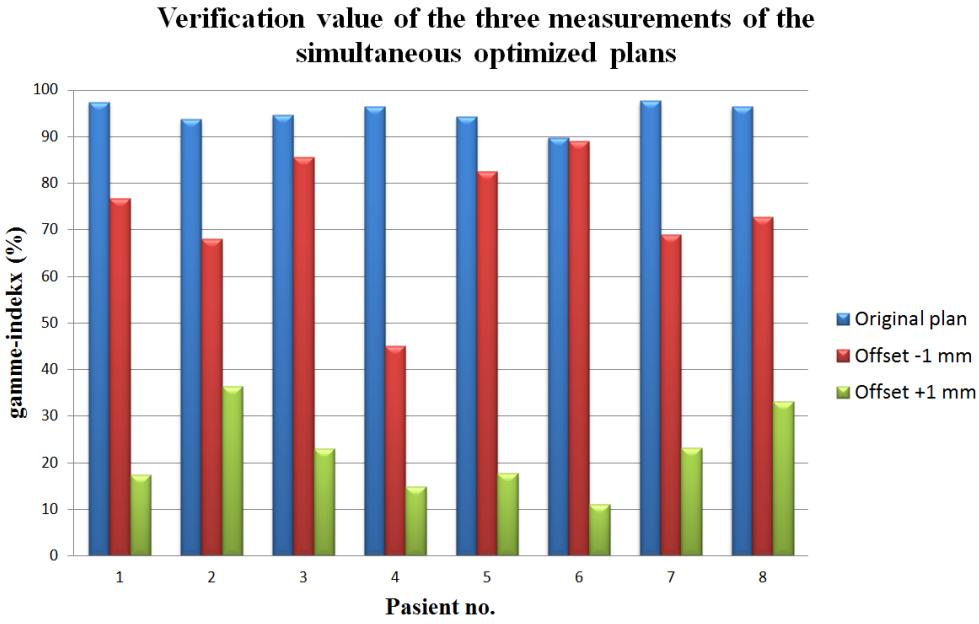


**Figure 4.2:** Comparison of the verification value of the three measurements, where no calibration error was included and $\pm 1$ mm MLC offset was included for the simultaneous optimized plans.

mization.

The average median to the dose deviation was 0.2 % and 1.6 % for the sequential and simultaneous, respectively (**fig. 4.3 and 4.4**). The simultaneous plan also showed a larger deviation when introduced the $\pm 1$ mm MLC offset of approximately $\pm 4.2$ %, while the sequential only deviated with approximately $\pm 2.2$ % with respect to the original plan. **Tab. 4.1** and **4.2** present the verification values (median to the DD, DTA and $\gamma$-index), all given in %.

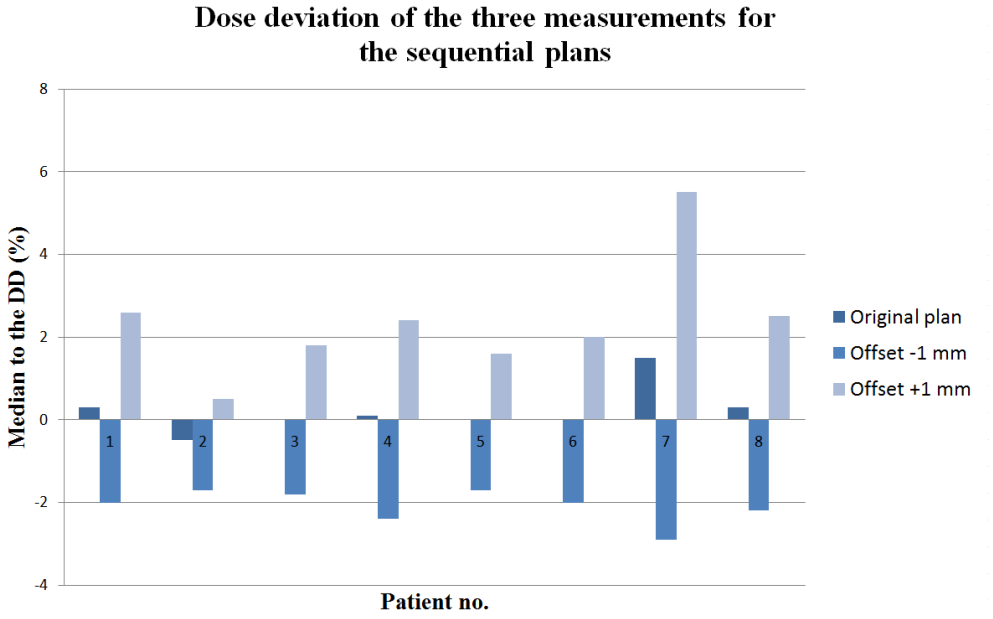


**Figure 4.3:** Median to the dose deviation for the three measurements of the sequential optimized plans.

The measured plans without MLC offset, for the sequential and simultaneous optimization, were set as a reference in ScandiDos Delta4 software to compare the relative difference to the plans with introduced MLC offset (**fig. 4.5**). An approximately equal deviation was present for the positive and negative offset, relative to the plans without MLC offset.

### 4.1.1 Monitor units

Amount of MU for the simultaneous and sequential optimized plans and the original clinical plans were collected from Plan Design in RayStation. All the patient plans consisted of two arcs, delivering different amounts of MU/fx (monitor units per fraction). The total amount of MU/fx delivered

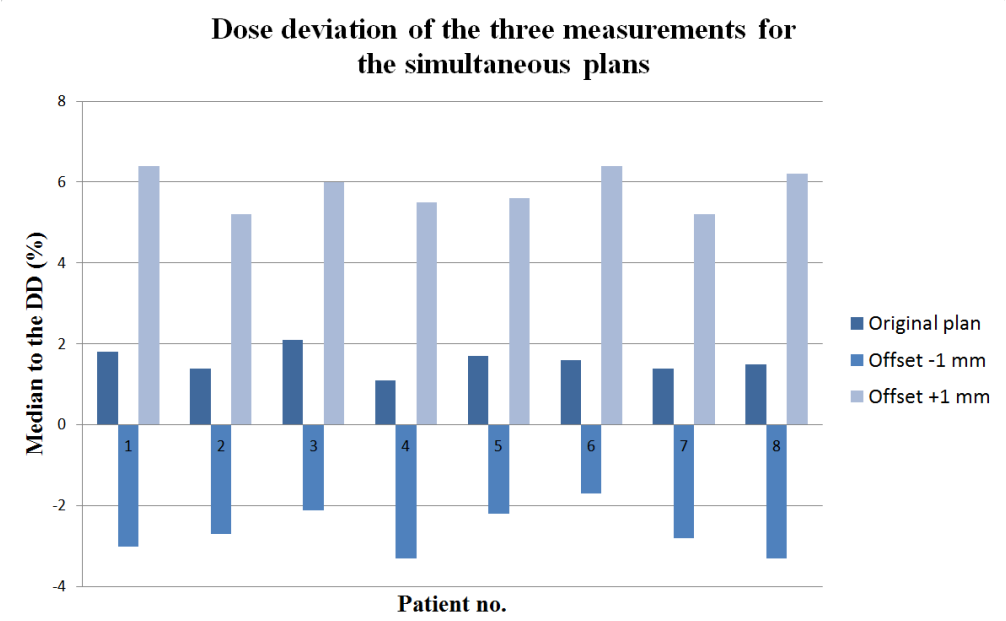


**Figure 4.4:** Median to the dose deviation for the three measurements of the simultaneous optimized plans.

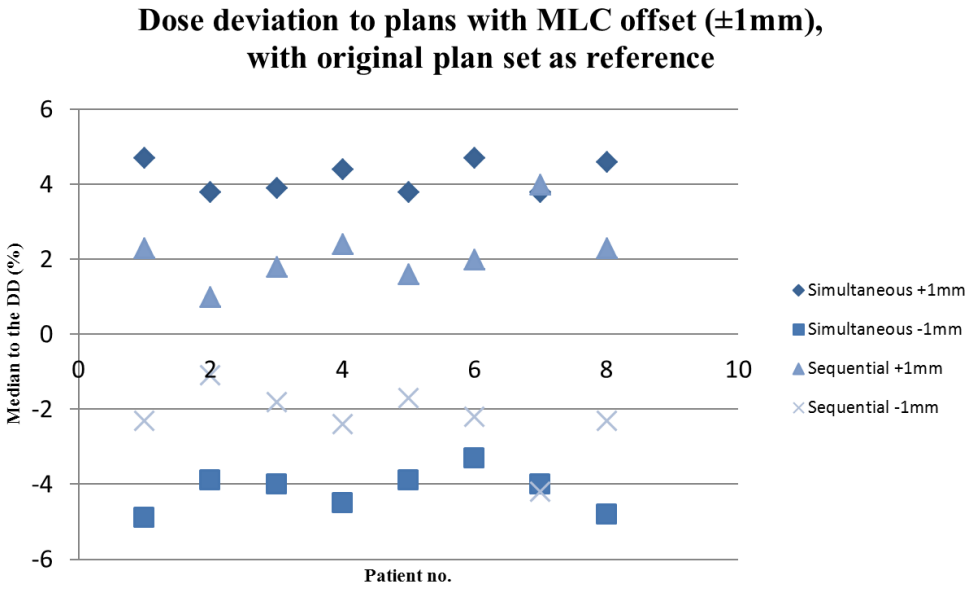


**Figure 4.5:** Median to the dose deviation with the original plans set as reference in the Delta4 software.

for each plan is presented in **fig. 4.6**. The simultaneous optimized plan and clinical plan had similar amount of delivered MU, with a significantly higher value than for the sequential plan.

**Table 4.1:** Verification values for the sequential plans with MLC offset ±1 mm

| | + 1 mm | | | - 1 mm | | |
|---|---|---|---|---|---|---|
| **Patient no.** | **Median** | **DTA** | **gamma** | **Median** | **DTA** | **gamma** |
| **1** | 2.3 | 97.4 | 87.8 | -2.3 | 98,7 | 87.4 |
| **2** | 1.0 | 100 | 100 | -1.1 | 100 | 100 |
| **3** | 1.8 | 98.2 | 98.4 | -1.8 | 100 | 97.1 |
| **4** | 2.4 | 97.4 | 86.1 | -2.4 | 100 | 92.9 |
| **5** | 1.6 | 100 | 96.7 | -1.7 | 100 | 97.6 |
| **6** | 2.0 | 100 | 84.5 | -2.2 | 100 | 88.2 |
| **7** | 4.0 | 89.3 | 31.9 | -4.2 | 90.9 | 33.6 |
| **8** | 2.3 | 99.1 | 87.2 | -2.3 | 99.1 | 87.4 |
| **Average** | 2.2 | 97.7 | 84.1 | -2.3 | 98.6 | 85.5 |

**Table 4.2:** Verification values for the sequential plans with MLC offset ±1 mm

| | + 1 mm | | | - 1 mm | | |
|---|---|---|---|---|---|---|
| **Patient no.** | **Median** | **DTA** | **gamma** | **Median** | **DTA** | **gamma** |
| **1** | 4.7 | 65.8 | 30.3 | -4.9 | 66.4 | 36.5 |
| **2** | 3.8 | 94.8 | 46.6 | -3.9 | 95.8 | 49.8 |
| **3** | 3.9 | 78.8 | 37.0 | -4.0 | 78.8 | 41.2 |
| **4** | 4.4 | 78.3 | 24.4 | -4.5 | 86.7 | 32.4 |
| **5** | 3.8 | 70.1 | 29.4 | -3.9 | 73.2 | 42.1 |
| **6** | 4.7 | 78.8 | 15.8 | -3.3 | 97.3 | 45.8 |
| **7** | 3.8 | 91.2 | 35.8 | -4.0 | 92.2 | 38.9 |
| **8** | 4.6 | 75.0 | 37.6 | -4.8 | 76.7 | 49.5 |
| **Average** | 4.2 | 79.1 | 321 | -4.2 | 83.4 | 42.0 |

### 4.1.2 Clinical approval

The dose volume histogram (DVH) in RayStation was used to compare the dose distribution for the two plans. **Fig. 4.7** shows the dose distribution to selected ROI (brainstem, medulla, parotis and four PTVs) for the simultaneous (——) and the sequential optimized plan (- - - -). The latter plan has a higher dose distribution to the OARs, but do not exceed the constraint of maximum dose sat for the OARs. The plan also has a more curved dose fall off to the PTVs, than for the simultaneous optimized plan.

Generally the coverage of the PTV did not deviate much between the two plans (simultaneous and sequential), which also was the case for patient no. 1 (**fig. 4.7**). The dose distribution of the OARs had a larger deviation, some OARs with a significantly difference. Still the constraints for

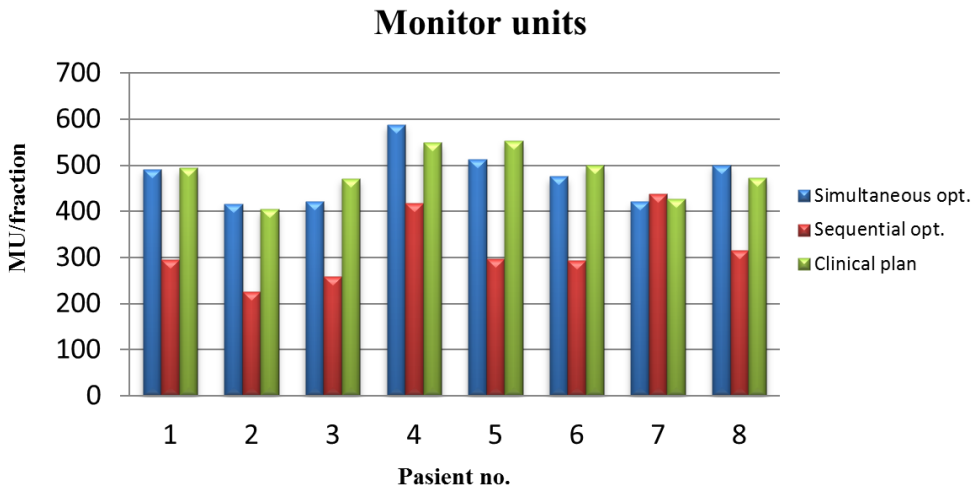


**Figure 4.6:** Total amount of MU/fx for the sequential, simultaneous and clinical plans.

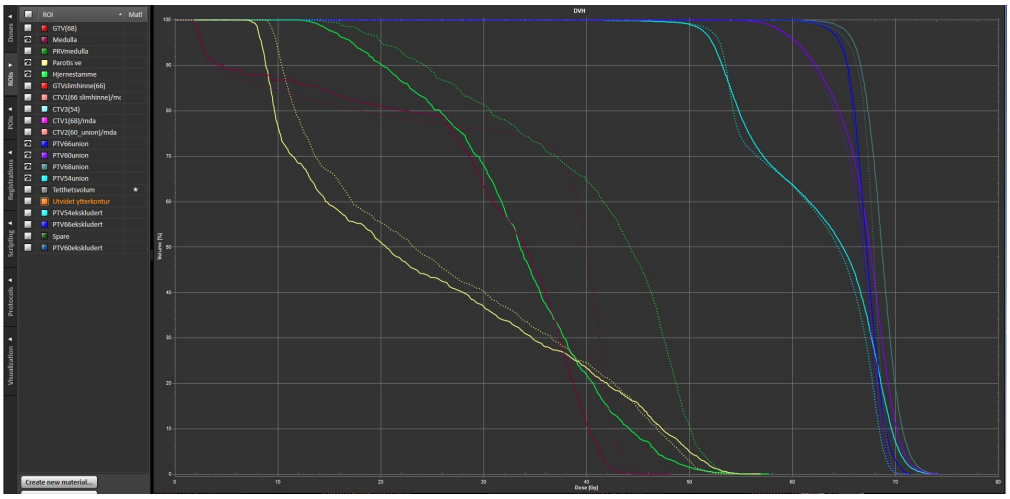

**Figure 4.7:** Comparison of the DVH to the simultaneous (——) and the sequential (- - - -) optimized plan, for patient case no. 1, in the Evaluation tab in RayStation.

the maximum dose to the OARs were obtained for all the patient cases in the two plans.

## 4.2 Simulation of MLC-parameter modifications in RayStation

The graphical comparisons of the measured and calculated dose distribution in RayPhysics are presented in the appendix, together with the values of the median dose ($D_{50\%}$) to the patients' PTVs. **Tab. 4.3** presents the $D_{50\%}$ to the specific PTV volume for the sequential and simultaneous optimized plans, with the clinical original linac applied.

An easier way of investigating the robustness to small errors in the MLC parameters of dose-plans,

is to simulations within the RayStation doseplanning system, instead of physically dislocating the MLC leaves. **Tab. 4.3** shows the median dose ($D_{50\%}$) for the main PTVs of the eight investigated patient cases.

**Table 4.3:** PTV $D_{50\%}$ to the sequential and simultaneous optimized plans, with the clinical treatment machine applied.

| Patient no. | PTV region | Sequential, $D_{50\%}$ | Simultaneous, $D_{50\%}$ |
|---|---|---|---|
| 1 | PTV66union | 66.85 | 67.20 |
| 2 | PTV60 | 59.97 | 59.87 |
| 3 | PTV60 | 59.98 | 59.96 |
| 4 | PTVboost | 14.09 | 14.07 |
| 5 | PTV60union | 60.57 | 60.09 |
| 6 | PTV60union | 65.02 | 65.30 |
| 7 | PTV60union | 67.67 | 67.68 |
| 8 | PTV60union | 67.50 | 67.48 |

### 4.2.1 Change of the MLC offset

The parameter *MLC x-position* offset in the Fluence tab, as described in **Background 2.7.3**, was changed from -0.005 cm to 0.200 cm. The positive offset corresponds to a movement of both MLC leaf banks 0.205 cm thus enlarging the total field opening by 0.410 cm. The simultaneous plans had an average increase in the $D_{50\%}$ to the PTV of 9.04 %, while the sequential plans had an average difference of 4.32 % (as presented in the summarized table, **tab. 4.15**).

**Fig. 4.8** compares the DVHs for the plan of patient case no. 1 with original treatment machine and the same plan with linac model *new_machine_MLC*, for both sequential and simultaneous optimization. **Tab. 4.4** and **4.5** list the $D_{50\%}$ for a specific PTV volume of the sequential and simultaneous optimized plans for the eight patient cases, together with the difference from the original $D_{50\%}$.

#### MLC offset, $\pm$1 mm

A comparison was done between a physical introduced MLC offset and a simulated offset done in the TPS. This was done to check that the dose calculation system agreed with the actual measurements when a MLC offset was introduced.

***Simulations in the TPS:***

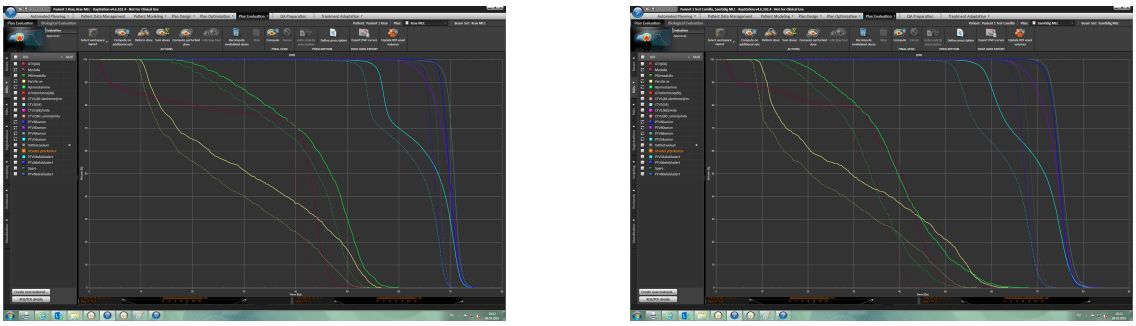

**(a)** Sequential optimization **(b)** Simultaneous optimization

**Figure 4.8:** Patient case no. 1. (——) is the plan with new machine (*new_machine_MLC*), (. . . . .) is the original clinical plan. An increase in the dose level is observed when the MLC offset increases. A larger increase was observed for the simultaneous plans, compared to the sequential plans.

**Table 4.4:** PTV $D_{50\%}$ for sequential plans with linac *new_machine_MLC*

| Patient no. | PTV region | $D_{50\%}$ | Difference from original (%) |
|---|---|---|---|
| 1 | PTV66union | 69.76 | 4.35 |
| 2 | PTV60 | 61.22 | 2.08 |
| 3 | PTV60 | 61.48 | 2.50 |
| 4 | PTVboost | 14.89 | 5.68 |
| 5 | PTV60union | 62.53 | 3.24 |
| 6 | PTV60union | 68.11 | 4.75 |
| 7 | PTV60union | 72.69 | 7.42 |
| 8 | PTV60union | 70.55 | 4.52 |
| Average | | 60.15 | 4.32 |

**Table 4.5:** PTV $D_{50\%}$ for simultaneous plans with linac *new_machine_MLC*

| Patient no. | PTV region | $D_{50\%}$ | Difference from original (%) |
|---|---|---|---|
| 1 | PTV66union | 74.73 | 11.21 |
| 2 | PTV60 | 65.05 | 8.65 |
| 3 | PTV60 | 64.34 | 7.30 |
| 4 | PTVboost | 15.75 | 11.94 |
| 5 | PTV60union | 65.33 | 8.72 |
| 6 | PTV60union | 70.63 | 8.16 |
| 7 | PTV60union | 72.41 | 6.99 |
| 8 | PTV60union | 73.93 | 9.56 |
| Average | | 63.08 | 9.07 |

MLC x-position offsets of +1 mm and -1 mm were introduced to different linacs in the beam com-

missioning (RayPhysics), called *new_machine_+1mm* and *new_machine_-1mm*. A comparison of the linacs together with the clinical linac was then done in RayStation TPS for the eight clinical patient cases. The comparison of the DVHs to patient case no. 1 in RayStation are shown in **fig. 4.9**. Rest of the DVH comparisons are presented in the appendix. **Tab. 4.6** (sequential) and **4.7** (simultaneous) list the $D_{50\%}$ of a specific PTV region for plans with linac model *new_machine_+1mm*. **Tab. 4.8** (sequential) and **4.9** (simultaneous) list the $D_{50\%}$ of a specific PTV region for plans with linac model *new_machine_-1mm*. The difference between these plans and the plans with original clinical linac are also presented in the same tables.
For the eight patient cases the average difference in $D_{50\%}$, with +1 mm MLC offset, for the sequential optimized plan was 2.26 %, and for the simultaneous optimized plan 4.67 %. The average difference in $D_{50\%}$, with -1 mm MLC offset, for the sequential optimized plan was -2.61 %, and for the simultaneous optimized plan was -4.38 %. **Tab. 4.10** summarizes the average differences, of the $D_{50\%}$, calculated in the TPS.

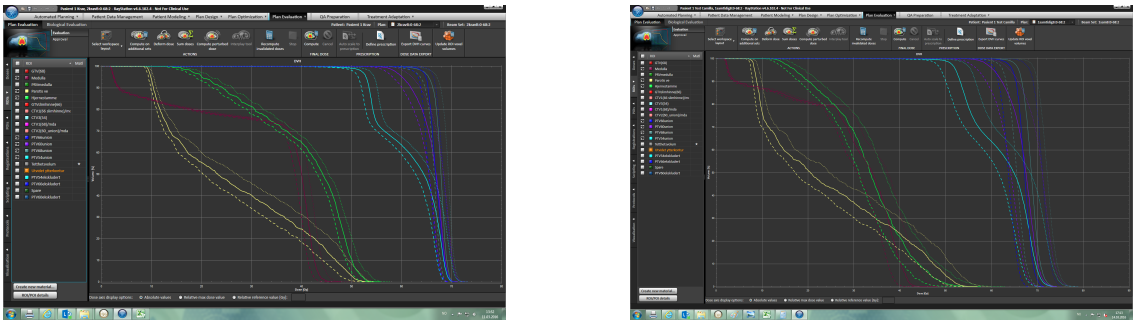

**(a)** Sequential optimization **(b)** Simultaneous optimization

**Figure 4.9:** Patient case no. 1. (——) is the plan with original machine, (- - - - -) is the plan with the machine *new_machine_-1mm*, (.....) is the plan with the machine *new_machine_+1mm*.

**Table 4.6:** PTV $D_{50\%}$ for sequential plans with linac *new_machine_+1mm*

| Patient no. | PTV region | $D_{50\%}$ | Difference from original (%) |
|---|---|---|---|
| 1 | PTV66union | 68.35 | 2.24 |
| 2 | PTV60 | 60.62 | 1.08 |
| 3 | PTV60 | 60.75 | 1.28 |
| 4 | PTVboost | 14.52 | 3.05 |
| 5 | PTV60union | 61.57 | 1.65 |
| 6 | PTV60union | 66.65 | 2.51 |
| 7 | PTV60union | 70.28 | 3.86 |
| 8 | PTV60union | 69.11 | 2.39 |
| Average | | 58.98 | 2.26 |

**Table 4.7:** PTV $D_{50\%}$ for simultaneous plans with linac *new_machine_+1mm*

| Patient no. | PTV region | $D_{50\%}$ | Difference from original (%) |
|---|---|---|---|
| 1 | PTV66union | 71.09 | 5.79 |
| 2 | PTV60 | 62.57 | 4.51 |
| 3 | PTV60 | 62.20 | 3.74 |
| 4 | PTVboost | 14.93 | 6.11 |
| 5 | PTV60union | 62.79 | 4.49 |
| 6 | PTV60union | 68.08 | 4.26 |
| 7 | PTV60union | 70.15 | 3.65 |
| 8 | PTV60union | 70.87 | 5.02 |
| Average | | 60.34 | 4.67 |

**Table 4.8:** PTV $D_{50\%}$ for sequential plans with linac *new_machine_-1mm*

| Patient no. | PTV region | $D_{50\%}$ | Difference from original (%) |
|---|---|---|---|
| 1 | PTV66union | 62.78 | -2.05 |
| 2 | PTV60 | 59.37 | -1.00 |
| 3 | PTV60 | 59.27 | -1.18 |
| 4 | PTVboost | 13.71 | -2.70 |
| 5 | PTV60union | 59.67 | -1.49 |
| 6 | PTV60union | 63.42 | -2.46 |
| 7 | PTV60union | 65.19 | -3.66 |
| 8 | PTV60union | 65.94 | -2.31 |
| Average | | 56.17 | -2.11 |

**Table 4.9:** PTV $D_{50\%}$ for simultaneous plans with linac *new_machine_-1mm*

| Patient no. | PTV region | $D_{50\%}$ | Difference from original (%) |
|---|---|---|---|
| 1 | PTV66union | 63.67 | -5.25 |
| 2 | PTV60 | 57.31 | -4.28 |
| 3 | PTV60 | 57.89 | -3.45 |
| 4 | PTVboost | 13.28 | -5.61 |
| 5 | PTV60union | 57.64 | -4.08 |
| 6 | PTV60union | 62.69 | -4.00 |
| 7 | PTV60union | 65.35 | -3.44 |
| 8 | PTV60union | 64.15 | -4.93 |
| Average | | 55.25 | -4.38 |

***Physical MLC offset:***

**Table 4.10:** Average changes in the $D_{50\%}$ between the different linac models, with MLC offsets of $\pm 1$ mm, and the original linac. The comparison was done in the TPS.

| | **Sequential** | **Simultaneous** |
|---|---|---|
| **-1 mm** | -2.61 % | -4.40 % |
| **+1 mm** | +2.26 % | 4.67 % |

Verification values (median to the DD, DTA and $\gamma$-index) were obtained for measurements done of the eight patient plans with physical MLC offset of $\pm 1$ mm MLC. The median to the DD could then be used in the comparison to the calculated values from RayStation, presented in **tab. 4.11**. The average differences, in percentage points, between the original plans and the plans with MLC offset were -4.22 (simultaneous) and -2.3 (sequential) for the negative offset, and 4.23 (simultaneous) and 2.15 (sequential) for the positive offset (**tab. 4.12**).

Comparing the average differences of the $D_{50\%}$ from the TPS calculation (**tab. 4.10**) and the median in the DD from the measured plans (**tab. 4.12**), the changes from the original plans were very similar and had an agreement within 0.5 percentage points.

**Table 4.11:** Median to the DD (%) for the measured plans with physical MLC offset $\pm 1$ mm

| **Patient no.** | **Original** | | **-1 mm** | | **+1 mm** | |
|---|---|---|---|---|---|---|
| | **Sim** | **Seq** | **Sim** | **Seq** | **Sim** | **Seq** |
| **1** | 1.8 | 0.3 | -3.0 | -2.0 | 6.4 | 2.6 |
| **2** | 1.4 | -0.5 | -2.7 | -1.7 | 5.2 | 0.5 |
| **3** | 2.1 | 0.0 | -2.1 | -1.8 | 6.0 | 1.8 |
| **4** | 1.1 | 0.1 | -3.3 | -2.4 | 5.5 | 2.4 |
| **5** | 1.7 | 0.0 | -2.2 | -1.7 | 5.6 | 1.6 |
| **6** | 1.6 | 0.0 | -1.7 | -2.0 | 6.4 | 2.0 |
| **7** | 1.4 | 1.5 | -2.8 | -2.9 | 5.2 | 5.5 |
| **8** | 1.5 | 0.3 | -3.3 | -2.2 | 6.2 | 2.5 |
| **Average** | 1.58 | 0.21 | -2.64 | -2.09 | 5.81 | 2.36 |

**Table 4.12:** Change in the measured median to the DD between the physical MLC offsets of +1 mm and -1mm and the original linac

| | **Sequential** | **Simultaneous** |
|---|---|---|
| **-1 mm** | -2.30 % | -4.21 % |
| **+1 mm** | +2.15 % | 4.24 % |

### 4.2.2 Tongue-and-groove offset

The T&G offset in RayPhysics was changed from 0.05 cm to 0.20 cm, and this linac model was called *new_machine_T&G*. Comparison of the two linac models, the clinical linac and *new_machine_T&G*, are shown in **fig. 4.10a** and **4.10b**, for the sequential and simultaneous optimized plans of patient case no. 1 (remaining DVHs to the eight patients are included in appendix). The T&G offset contributes to the total dose to the volumes (**Background 2.1.5**), resulting in a reduction in the dose level when the offset is increased. For the eight patient cases the average difference in $D_{50\%}$ for the sequential optimized plan is -4.29 %, and for the simultaneous optimized plan -7.42 % when the modified machine is used. This shows that with a rise in the T&G offset the total dose is reduced, due to the larger extent in the MLC leaf causing a higher under-dosage at the MLC flanks.

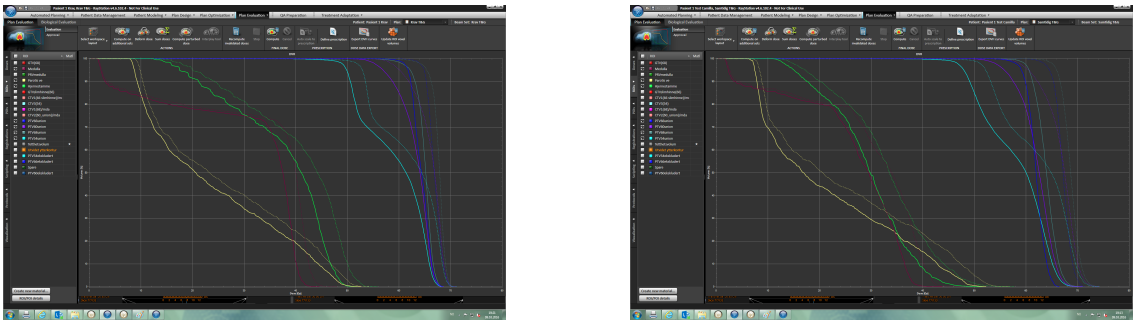

**(a)** Sequential optimization **(b)** Simultaneous optimization

**Figure 4.10:** Patient case no. 1. (——) is the plan with new machine model applied (*new_machine_T&G*), (.....) is the plan with the original linac.

**Tab. 4.13** and **4.14** present the $D_{50\%}$ to the main PTV for the eight patients. The difference to the original linac was a reduction of $\approx$4.2 $\pm$1.5 % for the sequential plans, and $\approx$6.9 $\pm$1.5 % for the simultaneous plans.

### 4.2.3 Summarized changes between the different machine models

**Tab. 4.15** shows a summary of the average difference in $D_{50\%}$ between the original machine and the four new machine models. The simultaneous optimized plans have approximately twice the difference for all the four new machines, compared to the sequential optimized plans, meaning that the simultaneous plans are more exposed to changes in both the MLC x-position parameter and in the tongue-and-groove parameter.

## 4.3 Numerical analyzes of differences in the MLC positions

Three scripts were made to extract information regarding the MLC positions in RayStation TPS, presented in **Materials and methods 3.4.3**. They were used to analyze differences between treat-

**Table 4.13:** PTV $D_{50\%}$ for sequential plans with linac *new_machine_T&G*

| Patient no. | PTV region | $D_{50\%}$ | Difference from original (%) |
|---|---|---|---|
| 1 | PTV66union | 64.32 | -3.78 |
| 2 | PTV60 | 58.58 | -2.32 |
| 3 | PTV60 | 58.44 | -2.57 |
| 4 | PTVboost | 13.34 | -5.32 |
| 5 | PTV60union | 58.81 | -2.91 |
| 6 | PTV60union | 61.53 | -5.37 |
| 7 | PTV60union | 63.91 | -5.56 |
| 8 | PTV60union | 63.72 | -5.60 |
| **Average** | | | -4.18 |

**Table 4.14:** PTV $D_{50\%}$ for simultaneous plans with linac *new_machine_T&G*

| Patient no. | PTV region | $D_{50\%}$ | Difference from original (%) |
|---|---|---|---|
| 1 | PTV66union | 61.97 | -7.78 |
| 2 | PTV60 | 55.64 | -7.07 |
| 3 | PTV60 | 56.64 | -5.54 |
| 4 | PTVboost | 13.14 | -6.61 |
| 5 | PTV60union | 55.53 | -7.59 |
| 6 | PTV60union | 60.76 | -6.95 |
| 7 | PTV60union | 64.08 | -5.32 |
| 8 | PTV60union | 62.00 | -8.12 |
| **Average** | | | -6.87 |

**Table 4.15:** Differences in the $D_{50\%}$ between the original and the new linac, with the original linac set as reference.

| | Sequential | Simultaneous |
|---|---|---|
| **MLC (-0.005 → 0.200 cm)** | +4.32 % | +9.40 % |
| **T&G (0.05 → 0.20 cm)** | -4.18 % | -6.89 % |
| **+1 mm (-0.005 → 0.100 cm)** | +2.26 % | +4.99 % |
| **-1 mm (-0.005 → -0.100 cm)** | -2.61 % | -4.40 % |

ment plans and study the MLC behavior during an irradiation. The scripts are included in the appendix together with a test-plan used to verify scripts. The scripts were run on the three treatment plans of the eight clinical patient cases: the clinical original plan, the sequential optimized plan and the simultaneous optimized plan. Graphical comparison of the verification degrees for the three plans and the total amount of MUs are shown in **fig. 4.11** and **4.6**. The sequential plans had consistently better verification value and lower amount of MUs.

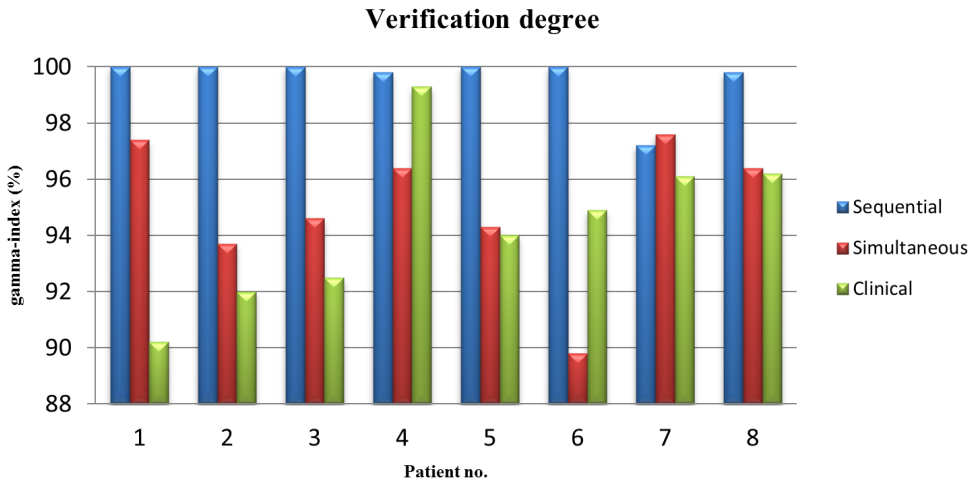


**Figure 4.11:** Verification value ($\gamma$-index) for the 8 patient cases with three different optimization sequences.

### 4.3.1 MLC flanks and islands

A slightly deviation was present between the distance between neighboring MLC leaf tips for the sequential and simultaneous optimized plans, **fig. 4.12**. Average distance of exposed MLC flanks for the two plans was 0.72 cm (STD = 0.054 cm) for the sequential optimized plans, and 0.62 cm (STD = 0.037 cm) for the simultaneous. The clinical and simultaneous plans had approximately the same MLC flank, and were within a 0.03 cm deviation.

In the same script where the information about the MLC flanks was extracted the amount of MLC islands was found. This is a total amount of MLC islands for all the arcs in a plan, presented in **fig. 4.13**. For all eight patient cases each plan consisted of two arcs with 90 segments. The sequential plan had the lowest amount with average of 279 islands. The simultaneous and clinical plans had an average number of 352 and 369 islands, respectively, and a maximum difference of 63 islands for patient case no. 5.

### 4.3.2 MLC opening

The sequential optimized plans had the largest distances between opposing MLC leaves (MLC opening), ergo the largest field sizes relative to the simultaneous and clinical plans (**fig. 4.14**). Average MLC opening for the sequential plans was 5.39 cm with average STD of 1.60 cm, while the

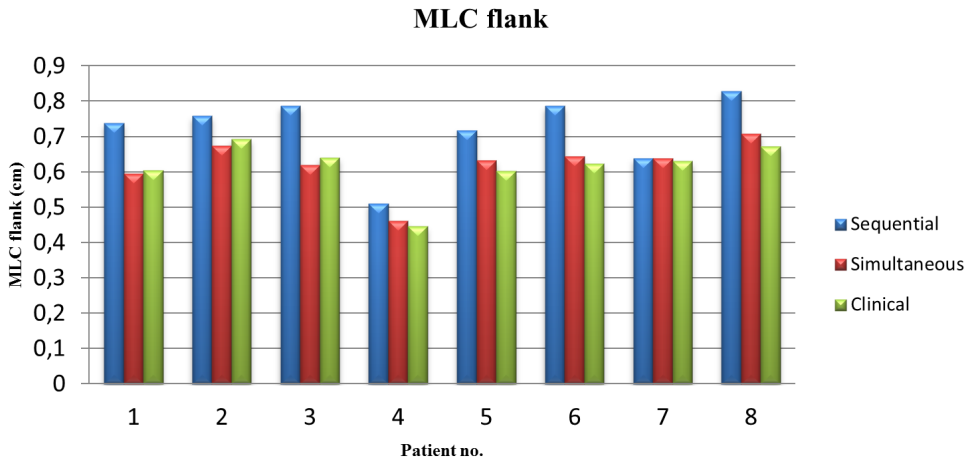


**Figure 4.12:** Average MLC flank per leaf for the three plans with different optimization sequences for the eight patient cases.

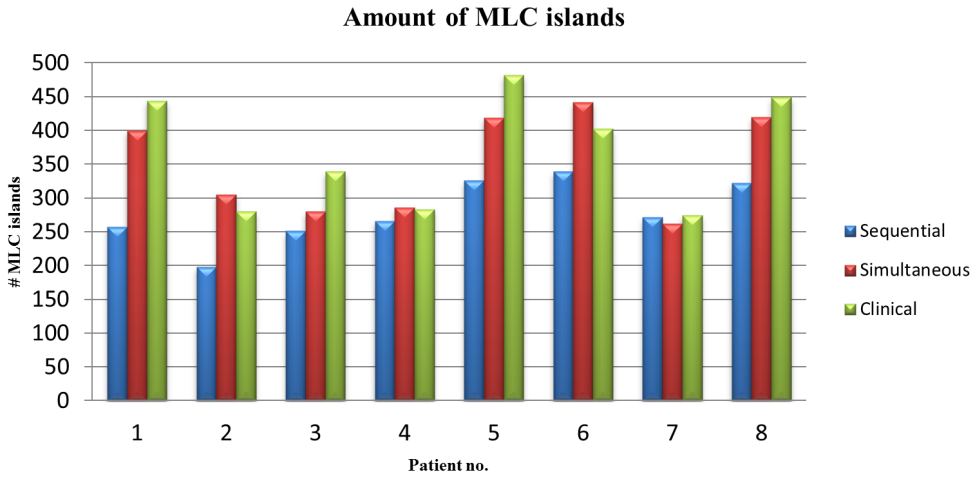


**Figure 4.13:** Average MLC islands for the three different optimization sequences for the eight patient cases.

simultaneous plans had average MLC opening of 3.13 cm with average STD of 0.81. Clinical and simultaneous plans had very similar MLC openings.

### 4.3.3 MLC speed

The travel distance of the MLC leaf tips between two segments/control points (MLC speed) was largest for the simultaneous plan, meaning that the leaf tips travel faster and are more exposed to uncertainties regarding MLC motions. The average travel distance for the simultaneous plan was 0.25 cm/deg (STD = 0.07), and for the sequential plan 0.17 cm/deg (STD = 0.06) (**fig. 4.15**).

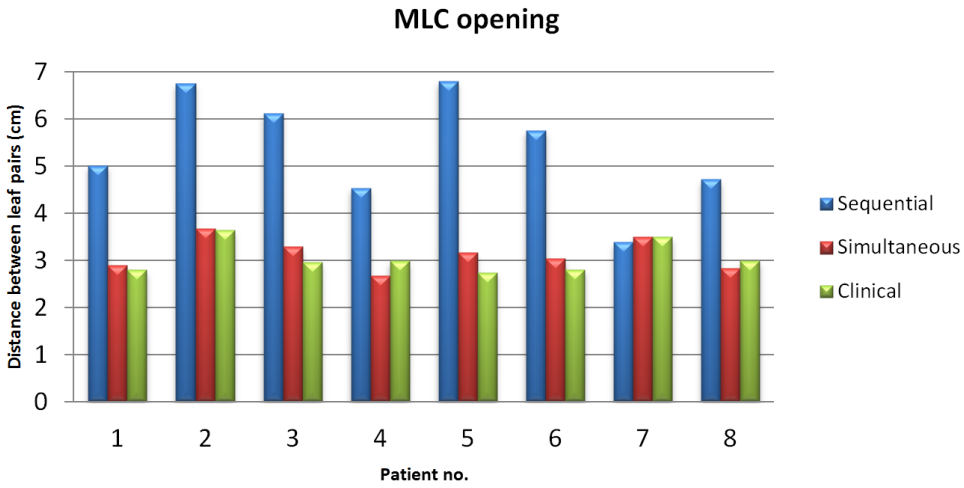


**Figure 4.14:** Average MLC opening of the three different optimization sequences for the eight patient cases.

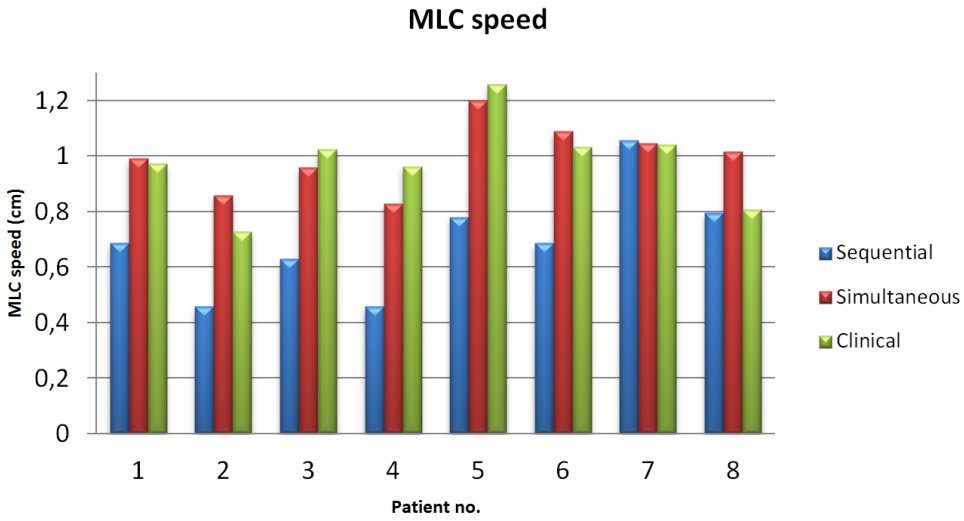


**Figure 4.15:** Average MLC speed of the three different optimization sequences for the eight patient cases.

### 4.3.4 Comparison of the extracted MLC information

**Tab. 4.16 - 4.18** compares the total MU, the MLC opening, the MLC flank and the difference to the original clinical patient cases. Also the difference of the MLC flank relative to its MLC opening is calculated, showing that the relative MLC flank is larger for the simultaneous plans than for the sequential.

**Table 4.16:** Sequential plans: comparison of achieved information and calculation of the relative difference between the MLC flank and opening.

| Patient no. | Total MU | MLC opening (cm) | MLC flank (cm) | Relative difference (%) | Difference to the original (Gy) |
|---|---|---|---|---|---|
| **1** | 294.70 | 5.01515 | 0.73855 | 14.73 | -3.78 |
| **2** | 226.25 | 6.75993 | 0.75831 | 11.22 | -2.32 |
| **3** | 258.89 | 6.11997 | 0.78630 | 12.85 | -2.57 |
| **4** | 417.57 | 4.53661 | 0.51010 | 11.24 | -5.32 |
| **5** | 296.52 | 6.80614 | 0.71721 | 10.54 | -2.91 |
| **6** | 293.38 | 5.75781 | 0.78652 | 13.66 | -5.37 |
| **7** | 438.42 | 3.38212 | 0.63850 | 18.88 | -5.56 |
| **8** | 315.79 | 4.72007 | 0.82851 | 17.55 | -5.60 |
| **Average** | 317.69 | 5.3872 | 0.7205 | 13.37 | -4.18 |

**Table 4.17:** Simultaneous plans: comparison of achieved information and calculation of the relative difference between the MLC flank and opening.

| Patient no. | Total MU | MLC opening (cm) | MLC flank (cm) | Relative difference (%) | Difference to the original (Gy) |
|---|---|---|---|---|---|
| **1** | 490.91 | 2.89090 | 0.59425 | 20.56 | -7.30 |
| **2** | 416.75 | 3.67088 | 0.67433 | 18.37 | -7.22 |
| **3** | 421.81 | 3.28664 | 0.61923 | 18.84 | -5.57 |
| **4** | 588.60 | 2.67686 | 0.46015 | 17.19 | -6.74 |
| **5** | 512.53 | 3.16445 | 0.63239 | 19.98 | -8.32 |
| **6** | 475.53 | 3.04312 | 0.64448 | 21.18 | -6.55 |
| **7** | 421.23 | 3.49824 | 0.63779 | 18.23 | -5.31 |
| **8** | 500.33 | 2.82766 | 0.70762 | 25.02 | -8.15 |
| **Average** | 478.46 | 3.1323 | 0.62128 | 19.83 | -6.89 |

### 4.3.5 Clinical patient cases

Ten random clinical patient cases with 100 % verification value were selected for a comparison with the obtained information from the eight patient plans, used in this thesis. The extracted MLC information are present in **tab. 4.19** and **4.20**. The clinical plans with 100 % verification value showed, in general, a low amount of MU, slow MLC speed, and small amount of MLC flank relative to the MLC opening.

### 4.3.6 Robustness-index

A robustness-index was suggested based on the previous extracted MLC-information and the amount of MUs of a plan. **E.q. 3.1** presents the index. The index was tested on the eight patient cases with

**Table 4.18:** Original clinical plans; comparison of achieved information and calculation of the relative difference between the MLC flank and opening.

| Patient no. | Total MU | MLC opening (cm) | MLC flank (cm) | Relative difference (%) |
|---|---|---|---|---|
| **1** | 294.70 | 2.79905 | 0.60451 | 21.60 |
| **2** | 226.25 | 3.64075 | 0.69334 | 19.04 |
| **3** | 258.89 | 2.96052 | 0.64000 | 21.62 |
| **4** | 417.57 | 2.98642 | 0.44560 | 14.92 |
| **5** | 296.52 | 2.73948 | 0.60160 | 21.96 |
| **6** | 293.38 | 2.80847 | 0.62247 | 22.16 |
| **7** | 438.42 | 3.49210 | 0.63008 | 18.04 |
| **8** | 315.79 | 2.98963 | 0.67232 | 22.49 |
| **Average** | 317.69 | 3.0520525 | 0.61374 | 20.23 |

**Table 4.19:** Clinical cases with 100 % verification degree

| **Plassering** | **MU** | **Flanke** | STD | **Opening** | STD | **Speed** | STD |
|---|---|---|---|---|---|---|---|
| $Brain_1$ | 212.78 | 0.45568 | 0.06034 | 6.33893 | 0.65092 | 0.13038 | 0.15507 |
| $Brain_2$ | 230.16 | 0.58553 | 0.04078 | 6.62701 | 1.44866 | 0.46475 | 0.34295 |
| $Otolaryngologi_1$ | 234.20 | 0.35507 | 0.01648 | 4.74435 | 1.24680 | 0.30608 | 0.28368 |
| $Otolaryngologi_2$ | 460.95 | 0.70163 | 0.03519 | 3.34049 | 0.60112 | 1.00780 | 0.22058 |
| Prostate | 389.57 | 0.80534 | 0.08227 | 6.30515 | 1.68821 | 0.78309 | 0.27909 |
| Ani | 271.89 | 0.61752 | 0.04606 | 6.84201 | 1.03309 | 0.41492 | 0.24308 |
| Recti | 314.42 | 0.59141 | 0.08512 | 5.29908 | 1.38750 | 0.38069 | 0.20197 |
| NH lymfom | 253.74 | 0.49073 | 0.05626 | 8.17337 | 1.41306 | 0.16476 | 0.11575 |
| Bile duct | 384.95 | 0.47582 | 0.02538 | 3.98593 | 1.66734 | 0.72339 | 0.37815 |

**Table 4.20:** Clinical cases with 100 % verification degree

| **Plassering** | **# open fields** | **# segments** | **# leaves (average)** |
|---|---|---|---|
| $Brain_1$ | 180 | 180 | 18.0 |
| $Brain_2$ | 100 | 94 | 25,5 |
| $Otolaryngologi_1$ | 94 | 92 | 20.0 |
| $Otolaryngologi_2$ | 324 | 180 | 34.0 |
| Prostate | 302 | 180 | 36.0 |
| Ani | 198 | 180 | 33.5 |
| Recti | 202 | 180 | 27.5 |
| NH lymfom | 184 | 180 | 33.0 |
| Bile duct | 319 | 180 | 38.0 |

different optimization sequences, presented in **tab. 4.21**

**Table 4.21:** Robustness-index for the 8 patient cases with different optimization sequence; clinical, simultaneous and sequential.

| Patient | Clinical | Simultaneous | Sequential |
|---|---|---|---|
| **1** | 41.5 | 34.9 | 7.1 |
| **2** | 15.1 | 19.6 | 2.3 |
| **3** | 33.1 | 21.4 | 5.2 |
| **4** | 20.9 | 24.3 | 5.8 |
| **5** | 62.7 | 48.5 | 7.4 |
| **6** | 43.7 | 43.7 | 8.8 |
| **7** | 20.5 | 19.7 | 22.0 |
| **8** | 34.1 | 50.6 | 13.2 |
| **Average** | 34.0 | 32.8 | 9.0 |

## 4.4 Tongue and Groove effects with different model settings

Three plans were made with fixed finger-patterns of different widths (0.5 cm, 1 cm and 2 cm), shown in **fig. 3.10**. Each of the plans consisted of two arcs with opposite leaves withdrawn. A comparison were done of two different machine models for each of these plans, observing the effect of the change in the T&G offset. The clinical linac was compared to the linac model (*new_machine_T&G*), with T&G offset changed from 0.05 cm to 0.20 cm. **Fig. 4.16** shows the comparison of the DVHs to the different machine models, with T&G offset equal 0.05 cm (clinical) and 0.20 cm (*new_machine_T&G*), for the three finger-pattern plans (1LP, 2LP and 4LP, LP = leaf position).

**Table 4.22:** Median dose ($D_{50\%}$) delivered to the PTV for the three plans with the original linac and the same three plans with linac model *new_machine_T&G*.

| Plan | PTV (Gy) |
|---|---|
| 1LP | 30.98 |
| 2LP | 34.01 |
| 4LP | 35.78 |
| 1LP_T&G | 11.54 |
| 2LP_T&G | 24.24 |
| 4LP_T&G | 31.88 |

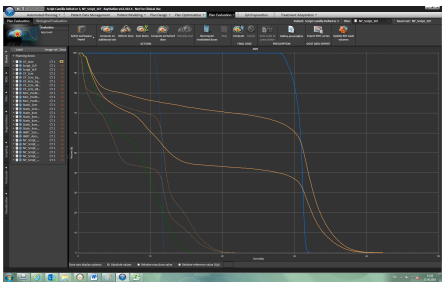

**(a)** 1LP

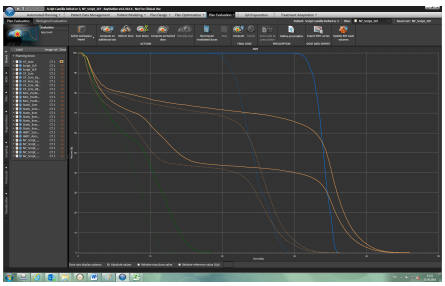

**(b)** 2LP

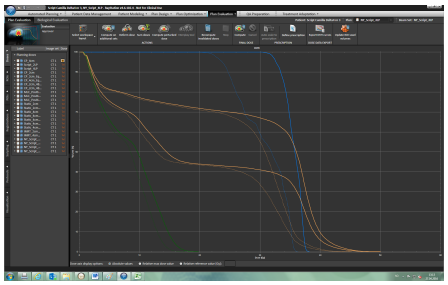

**(c)** 4LP

**Figure 4.16:** Comparison of the DVHs to two linac models with different T&G parameter: (——) has T&G offset = 0.05 cm and (. . . . .) has T&G offset = 0.20 cm.

For the plan with finger-pattern width of 0.5 cm (1 MLC leaf, 1LP) the reduction in $D_{50\%}$ PTV when applying the linac model *new_machine_T&G* was 62.75 %. The plan clearly shows that the T&G parameter has a significant contribution when many MLC flanks are present.

For the plan with finger-pattern width of 1.0 cm (2 MLC leaves, 2LP) the reduction in $D_{50\%}$ PTV when applying the linac model *new_machine_T&G* was 28.73 %. The T&G parameter has also here a significant contribution when several MLC flanks are present.

For the plan with finger-pattern width of 2.0 cm (4 MLC leaves, 4LP) the reduction in $D_{50\%}$ PTV when applying the linac model *new_machine_T&G* was 10.90 %.

### 1LP vs. 2LP vs. 4LP with linac model *new_machine_T&G*

**Fig. 4.17** compares the DVHs for the three finger-pattern plans with *new_machine_T&G* as applied linac model. A 12.7 Gy deviation between $D_{50\%}$ to the PTV was present between the 1LP plan (——) and the 2LP plan (. . . . .). A 7.64 Gy deviation between $D_{50\%}$ to the PTV was present between the 2LP plan (. . . . .) and the 4LP plan (- - - - -).

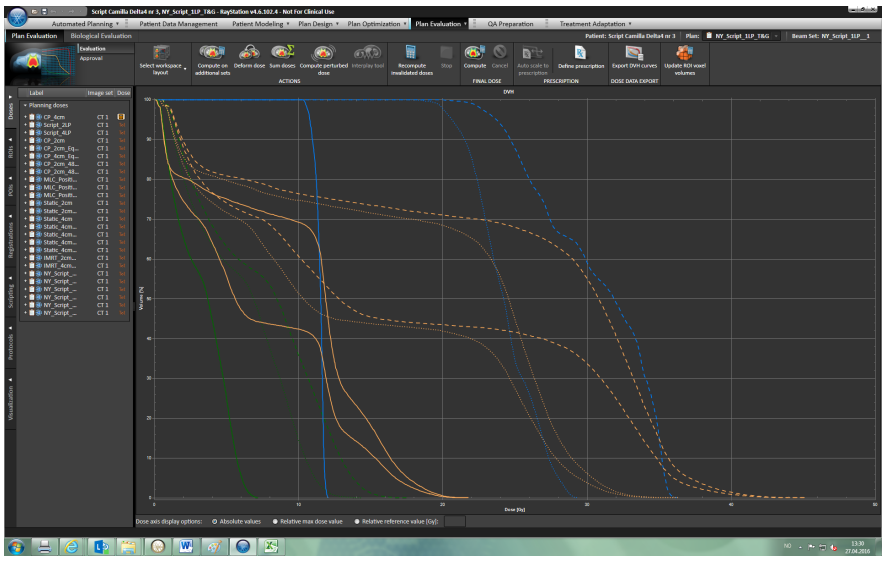

**Figure 4.17:** The three finger-pattern plans with new machine model: (——) 1LP, (.....) 2LP, and (- - - - -) 4LP.

## 4.5 Analyzes of MLC position characteristics

Several plans were made with three main types of the MLC position. **Material and methods 3.4.2** includes all the different types made for testing the tongue-and-groove effect and the MLC travel distance.

### 4.5.1 Tongue-and-groove plans

Two of the same finger-print plans used to compare the two different machine models were used to check the actual dose output, with the clinical treatment machine applied. The first plan had 1 cm finger-width (2LP), while the second had 2 cm finger-width (4LP). Both plans consisted of two arcs with gantry rotation of 356°. Measurements were done on the Delta4 phantom on two different linacs (SB2 and SB3), presented in **tab. 4.23** and **4.24**.
The first plan with finger-width 1 cm consist of twice as many protrusions as for the plan with finger-width of 2 cm, and was therefore expected to be more exposed to the T&G effect. Both plans had a significant under-dosage due to the T&G effect, where the plan with 1 cm protrusion width had the largest under-dosage.

**Table 4.23:** Verification values for the plan 2LP

| Linac | Median | DTA | $\gamma$-index |
|---|---|---|---|
| **SB3** | -5.0 | 58.5 | 13.6 |
| **SB2** | -6.8 | 27.7 | 3.7 |

**Table 4.24:** Verification values for the plan 4LP

| Linac | Median | DTA | $\gamma$-index |
|---|---|---|---|
| **SB3** | -2.2 | 88.7 | 62.1 |
| **SB2** | -2.8 | 75.5 | 46.1 |

### 4.5.2 Dynamic movement of a constant field opening

The first measurements of the dynamic MLC movement were done with a constant field size of 2 cm, with MLC speed (traveling distance) 0.5 cm/deg, and of a 4 cm field size with 1 cm/deg MLC speed. The latter plan showed a larger over-dosage and a poorer DTA resulting in a lower $\gamma$-index. The first plan also had a little larger dose than calculated, thereby an average $\gamma$-index of 89.9 %. The two plans were measured on three of the four linacs, showing a larger deviation for the plan with the fastest MLC speed (1 cm/deg).

**Table 4.25:** Plan with a 2 cm fixed field opening moving with MLC speed 0.5 cm/deg

| Linac | Median | DTA | Gamma |
|---|---|---|---|
| **SB3** | 1.0 | 100 | 87.0 |
| **SB2** | 1.0 | 100 | 91.3 |
| **SB4** | 1.2 | 100 | 91.3 |

**Table 4.26:** Plan with a 4 cm fixed field opening moving with MLC speed 1 cm/deg

| Linac | Median | DTA | Gamma |
|---|---|---|---|
| **SB3** | 2.8 | 84.2 | 49.9 |
| **SB2** | 2.2 | 94.7 | 60.7 |
| **SB4** | 2.7 | 94.7 | 53.5 |

Several different field sizes were then measured with various MLC travel distances to analyze the dynamic movement of the MLC leaves. The measurements were done twice on linac SB2. The agreement in the $\gamma$-index between the two measurements was a little deviating, especially for two of the plans (5 cm field opening with MLC speed of 1.2 cm/deg and 1 cm field opening with MLC speed of 0.5 cm/deg), which deviated with 9.3 and 10 percentage points. The median to the DD had a good agreement and deviated with maximum 0.6 percentage points for the 2 cm field size with speed of 1.2 cm/deg. The DTA had more spread values. For both the 1$^{st}$ and 2$^{nd}$ measurement the mean verification value was poorest for the MLC speed of 1 cm/deg, with 77.6 % and 76.6 %, respectively. The best mean verification result was for the lowest MLC speed of 0.5 cm/deg. **Tab. 4.27 - 4.32** present all the measured data of the measurements.

Generally all the field sizes received more dose than calculated, except the smallest field size (1

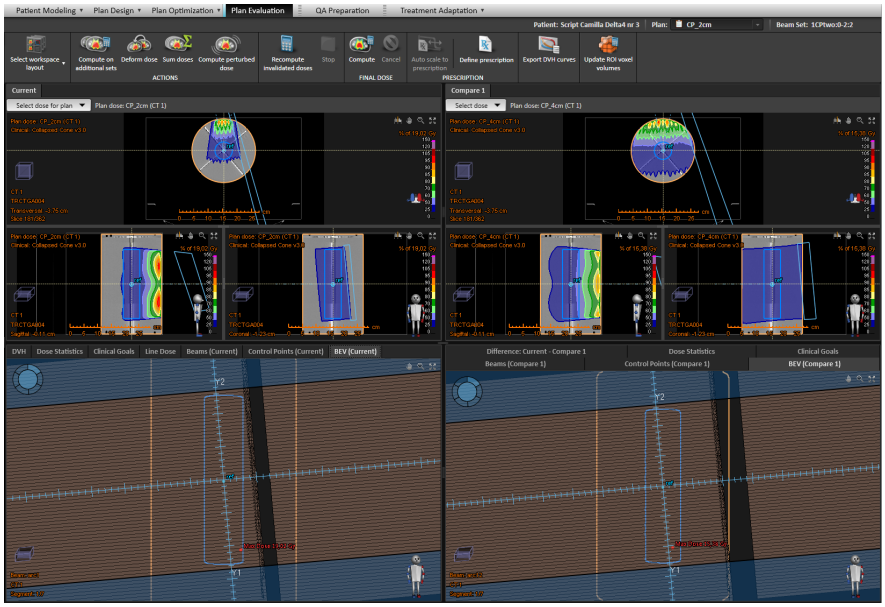

**Figure 4.18:** Comparison in the Plan Evalutaion in RayStation of the two plans with fixed field opening and travel distance of 2 cm & 0.5 cm/deg (left), and 4 cm & 1 cm/deg (right).

cm) which had an under-dosage for all the MLC speeds. This under-dosage was most prominent for the two lowest MLC speeds, with a median to the DD of approximately -3 %. The opposite was the case for field sizes $\leq$ 2 cm, the over-dosage decreased as the MLC speed got slower.

The field size 1.5 cm did not behave as either the 1 cm or as larger field sizes. At the fastest travel distance (1.25 cm/deg) an over-dosage occurred, which increased for the MLC speed of 1 cm/deg, while decrease for the slowest speed (0.5 cm/deg).

**Table 4.27:** 1$^{st}$ measurement of various MLC openings with MLC speed 1.25 cm/deg

| Field opening | Median | DTA | Gamma |
|---|---|---|---|
| 1 cm | -1.1 | 95 | 87 |
| 1.5 cm | - | - | - |
| 2 cm | 2.3 | 92.5 | 84.6 |
| 4 cm | 2.5 | 92.4 | 73.2 |
| 5 cm | 1.5 | 91.5 | 83.9 |

### 4.5.3 Constant field

It is challenging to accurately calculate the dose of small fields in the TPS. Therefore, the three smallest field sizes (1.0 cm, 1.5 cm and 2.0 cm) used in this thesis were measured to verify the agreement of a static field (**Materials and methods 3.4.2**). The measurements, **tab. 4.33**, showed

**Table 4.28:** 2nd measurement of various MLC openings with MLC speed 5cm/4deg

| Field opening | Median | DTA | Gamma |
|---|---|---|---|
| 1 cm | -0.6 | 95.7 | 89.7 |
| 1.5 cm | 1.6 | 96.9 | 84.2 |
| 2 cm | 1.7 | 95.2 | 82.8 |
| 4 cm | 2.6 | 96.2 | 77.2 |
| 5 cm | 1.8 | 98.6 | 93.2 |

**Table 4.29:** 1st measurement of various MLC openings with MLC speed 4cm/4deg

| Field opening | Median | DTA | Gamma |
|---|---|---|---|
| 1 cm | -2.9 | 88.4 | 66.7 |
| 1.5 cm | - | - | - |
| 2 cm | 0.7 | 94.1 | 80.3 |
| 4 cm | 1.5 | 97.2 | 85.8 |

**Table 4.30:** 2nd measurement of various MLC openings with MLC speed 4cm/4deg

| Field opening | Median | DTA | Gamma |
|---|---|---|---|
| 1 cm | -3.1 | 87.8 | 67.1 |
| 1.5 cm | 2.5 | 86.7 | 66.7 |
| 2 cm | 0.8 | 96.7 | 81.8 |
| 4 cm | 1.8 | 99.1 | 90.6 |

**Table 4.31:** 1st measurement of various MLC openings with MLC speed 2cm/4deg

| Field opening | Median | DTA | Gamma |
|---|---|---|---|
| 1 cm | -2.8 | 99.4 | 95.0 |
| 1.5 cm | - | - | - |
| 2 cm | 0.3 | 98.7 | 97.3 |

**Table 4.32:** 2nd measurement of various MLC openings with MLC speed 2cm/4deg

| Field opening | Median | DTA | Gamma |
|---|---|---|---|
| 1 cm | -3.1 | 100 | 85.0 |
| 1.5 cm | 0.3 | 99.5 | 100 |
| 2 cm | 0.3 | 100 | 98.6 |

a good agreement to the calculated dose. The smallest field size of 1 cm had a tiny under-dosage while the 2 cm field size had a tiny over-dosage. Still, both had a 100 % QA-value.

**Table 4.33:** Verification values for measurements of three small field sizes

| Field opening | **Median** | **DTA** | **Gamma** |
|---|---|---|---|
| **1.0 cm** | -0.4 | 100 | 100 |
| **1.5 cm** | 0.0 | 100 | 100 |
| **2.0 cm** | 0.6 | 100 | 100 |

### 4.5.4 Effect of the gravitation field on MLC leaves

To check whether there is an effect of the gravitation field on the MLC leaves, measurements were done for gantry angles 0°, 90° and 270°, with collimator angles 0° and 90°. The plan used for the measurements was the same as previous used, a 4 cm fixed field opening moving with a travel distance of 1 cm/deg. Totally 6 measurements were done where each of the three gantry angle consisted two plans with different collimator angle. At gantry angles 90° and 270° the MLC leaves will be placed perpendicular to the gravitation field for collimator angle 90°, and along the gravity axis for collimator angle 0°.

For gantry angle 0° the difference of the $\gamma$-index between the collimator angles 0° and 90° was 4.8 percentage points, which was the smallest difference between the two collimator angles. For gantry angles 90° and 270° the difference of the $\gamma$-index in percentage points was 38.7 and 28.3, respectively, and significantly higher than for the gantry at 0°. The $\gamma$-index had also considerably better verification for gantry angle 0°. All of the six plans measured a higher dose than calculated.

**Table 4.34:** Measurements of the six plans with different gantry and collimator angle checking the gravitational effect

| **Gantry angle (deg)** | **Collimator angle (deg)** | **Median (%)** | **DTA (%)** | **Gamma (%)** |
|---|---|---|---|---|
| 0 | 0 | 2.1 | 100 | 65.9 |
| 0 | 90 | 2.0 | 100 | 61.1 |
| 90 | 0 | 3.0 | 100 | 52.1 |
| 90 | 90 | 3.5 | 100 | 13.4 |
| 270 | 0 | 2.8 | 63.5 | 40.0 |
| 270 | 90 | 3.2 | 100 | 11.7 |

For beams at gantry angles 90° and 270° one arc is going with the gravitation force and the other arc against. **Tab. 4.35** and **4.36** show the measurements for each of the arcs. For collimator angle 0°: arc1 is going with the gravitational field, while the MLC leaves are moving against the field. Arc2 is going against the field, while the MLC leaves are moving with it. For coll. angle 90° the MLC travel direction are perpendicular for both arcs.

The approach of the optimization process was equal for all the 6 plans except for the collimator angle (0° or 90°) and the gantry angle (0°, 90° or 270°). An equal dose distribution was therefore

**Table 4.35:** Arc1 moving with the gravitational field

| Gantry angle (deg) | Collimator angle (deg) | Median (%) | DTA (%) | Gamma (%) |
|---|---|---|---|---|
| 90 | 0 | 2.9 | 100 | 51.1 |
| 90 | 90 | 3.5 | 100 | 15.5 |
| 270 | 0 | 2.8 | 63.5 | 41.5 |
| 270 | 90 | 3.1 | 100 | 16.7 |

**Table 4.36:** Arc2 moving with the gravitational field

| Gantry angle (deg) | Collimator angle (deg) | Median (%) | DTA (%) | Gamma (%) |
|---|---|---|---|---|
| 90 | 0 | 3.0 | 100 | 54.0 |
| 90 | 90 | 3.4 | 98.9 | 11.1 |
| 270 | 0 | 2.9 | 60.3 | 37.9 |
| 270 | 90 | 3.4 | 100 | 11.5 |

expected for the 6 plans after dose calculation in RayStation. **Tab. 4.37** and **4.38** show the dose for the $\text{PTV}_{average}$, $\text{PTV}_{D50\%}$, the outer structure (periphery) and total amount of MU for each of the collimator angles and gantry angles. Gantry angle 0° and 90° had very similar dose distribution and the same amount of total MU, though gantry angle 270° had a significant higher value of total MU and thereby also a larger value of the dose to the volumes. **Fig. 4.19** shows the comparison of the three plans in the Evaluation tab in RayStation: for **fig. 4.19a** the three plans have collimator angle 0° and for **fig. 4.19b** the three plans have collimator angle 90°.

**Table 4.37:** Dose distribution for three plans with different gantry angles, all with collimator angle 0°

| Gantry angle | PTV average | PTV (D50) | Periphery | Total MU |
|---|---|---|---|---|
| 0 | 13.11 | 13.05 | 8.05 | 280 |
| 90 | 13.11 | 13.06 | 8.06 | 280 |
| 270 | 13.70 | 13.70 | 12.23 | 400 |

**Table 4.38:** Dose distribution for three plans with different gantry angles, all with collimator angle 90°

| Gantry angle | $\text{PTV}_{average}$ | $\text{PTV}_{D50\%}$ | Periphery | Total MU |
|---|---|---|---|---|
| 0 | 9.23 | 11.42 | 4.59 | 280 |
| 90 | 9.23 | 11.40 | 4.59 | 280 |
| 270 | 12.74 | 13.14 | 9.92 | 400 |

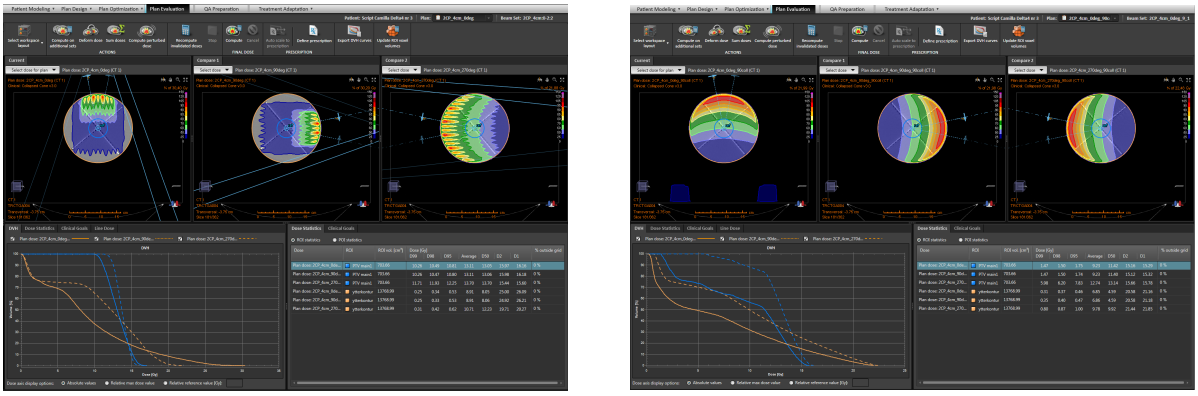

**(a)** Collimator angle 0°

**(b)** Collimator angle 90°

**Figure 4.19:** Comparison of the dose distribution in the Evaluation tab (RayStation) of the three plans with gantry angle 0°, 90° and 270°.

## 4.6 Measurements of the T&G effect

### 4.6.1 Diamond detector

Finger-pattern plans with three different protrusion widths of 5, 10 and 20 mm were measured using a diamond detector placed at 10 cm depth in a water phantom. For each plan, the dose curves from the two beams were added together finding the total dose curves for the plans with overlapping finger-patterns. The tongue-and-groove effect was prominent for all three plans at the line where the overlap of the MLC flanks occurred.

**Fig. 4.20 - 4.22** show the dose curves of the three plans consisting of two beams (blue and red curves), and the sum giving the total dose curve (green). The depth of the wells is deeper for the largest protrusion widths, because the field size is large enough for CPE to be obtained. The effect of small fields is presented in **fig. 2.10b**, showing that the penumbra from opposing field edges may overlap resulting in an under-dosage. This will result in shallower wells, as the case for the 5 mm width protrusion.

Since the reference detector was placed in a open field for the first beam, and was not moved in the second beam (thereby shielded by a MLC leaf), the beams needed to be normalized before a summation. Therefore, the dose level is not to scale and the y-axis of the **fig. 4.20 - 4.22** are presented in relative dose. Since the main interest was of the shape of the dose curves the dose level was not pursued in this experiment.

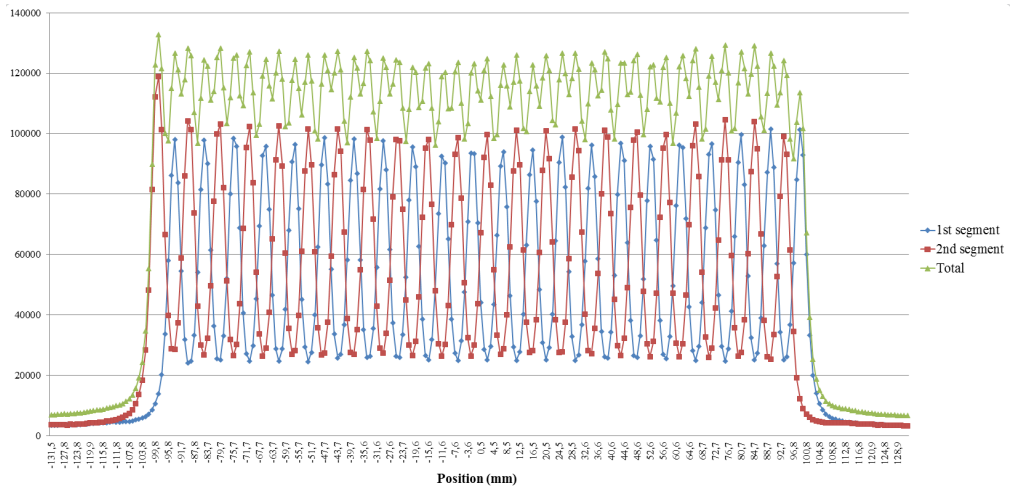


**Figure 4.20:** Cross-plane profiles for 3D-CRT T&G plan with protrusion width of 5 mm, measured with a diamond detector. Sum of 1st (blue) and 2nd (red) beam add up to the total dose distribution (green).

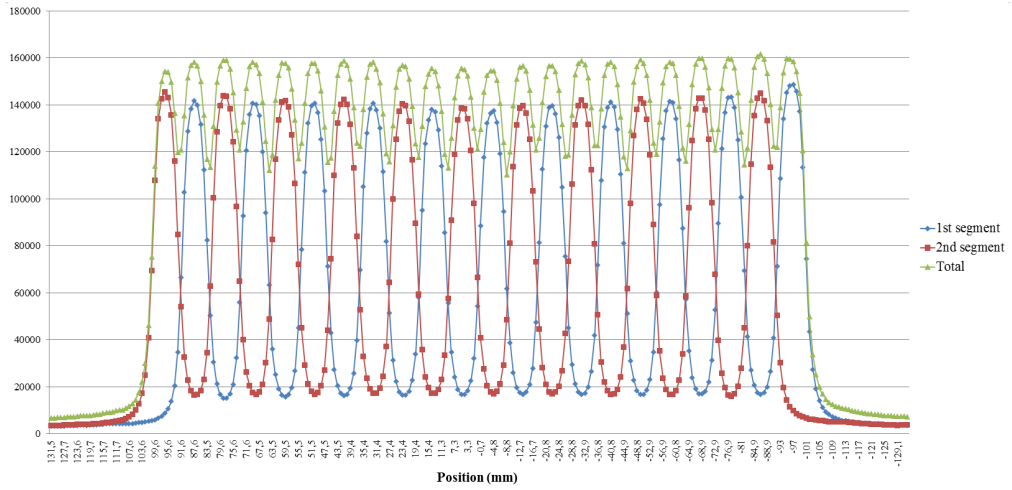


**Figure 4.21:** Cross-plane profiles for 3D-CRT T&G plan with protrusion width of 10 mm, measured with a diamond detector. Sum of 1st (blue) and 2nd (red) beam add up to the total dose distribution (green).

### 4.6.2 Gafchromic films

The same three 3D-CRT plans with MLC finger-patterns of different protrusion widths (5, 10 and 20 mm) used for the diamond detector were also measured using gafchromic radiotherapy films. The comparison of the calculated vertical dose-profile in RayStation and the measured vertical dose-profile from the gafchromic films was done in the software program VerA, presented in **fig. 4.23 - 4.25**.

The measured profiles had significantly deeper wells than the calculated profiles. The depths of the measured wells were approximately 22 %, 31 % and 25 % of the mean dose between position -5 cm to 5 cm (**tab. 4.39**), while the calculated wells amounted approximately 4 %, 10 % and 15

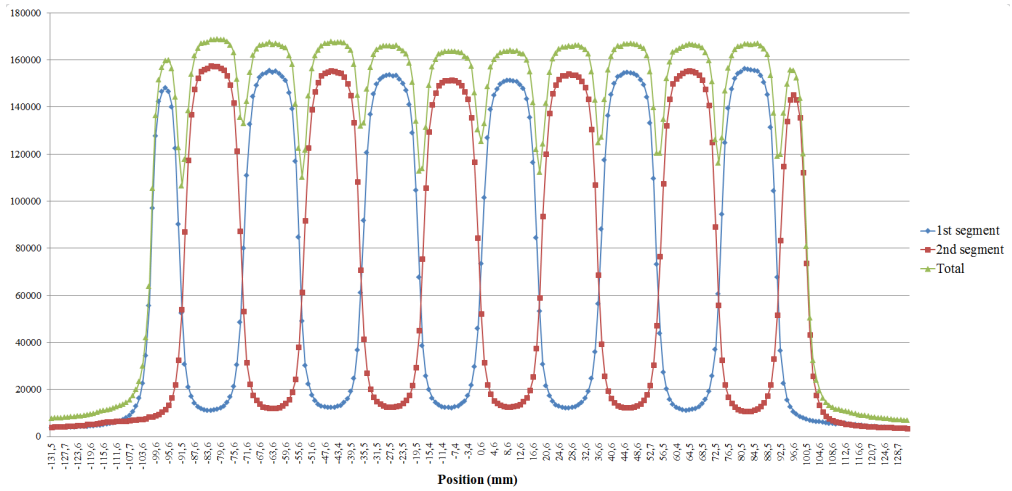


**Figure 4.22:** Cross-plane profiles for 3D-CRT T&G plan with protrusion width of 20 mm, measured with a diamond detector. Sum of 1st (blue) and 2nd (red) beam add up to the total dose distribution (green).

%. The tongue-and-groove effect has obviously larger contribution on the dose distribution than accounted for in the dose calculation done by RayStation TPS. The dose was normalized to 2 Gy in RayStation, as can be observed by the sinusoidal dose curve having 2 Gy as mean dose. The mean dose in the middle region (from -5 cm to 5 cm) was slightly lower for the measured plans, **tab. 4.39**. The average calculated mean dose was ≈2.04 ±0.02 Gy, while the average measured mean dose was ≈1.93 ±0.08 Gy.

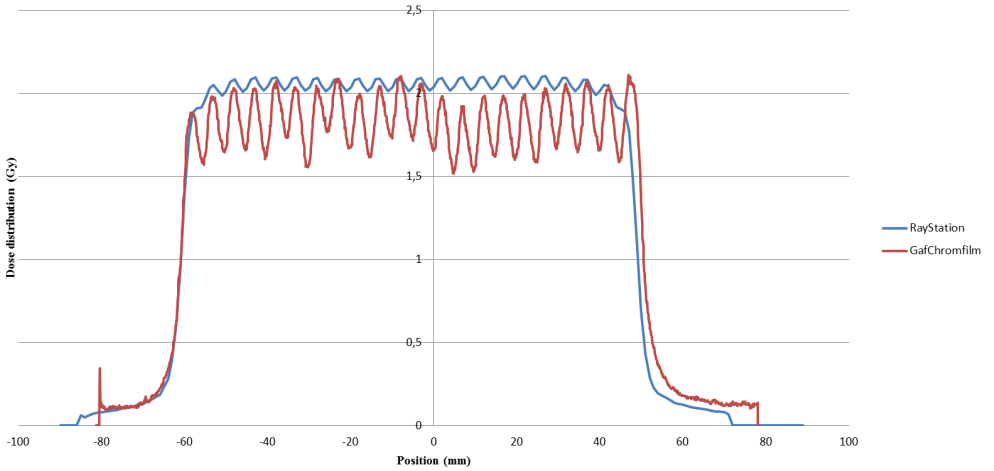


**Figure 4.23:** Dose-profile comparison for the finger-pattern-plan with 5 mm protrusion width. Blue graph is the calculated profile from RayStation and red graph is the measured profile from the gafchromic film.

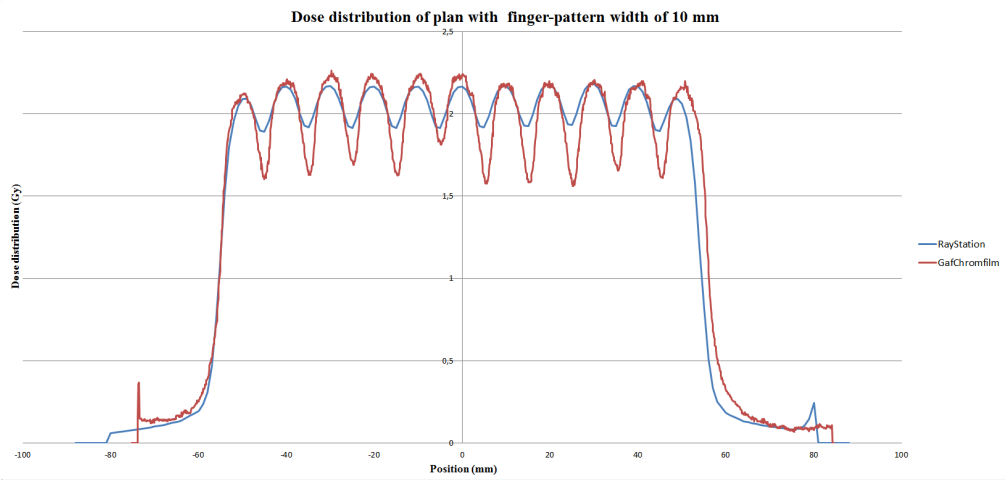


**Figure 4.24:** Dose-profile comparison for the finger-pattern-plan with 10 mm protrusion width. Blue graph is the calculated profile from RayStation and red graph is the measured profile from the gafchromic film.

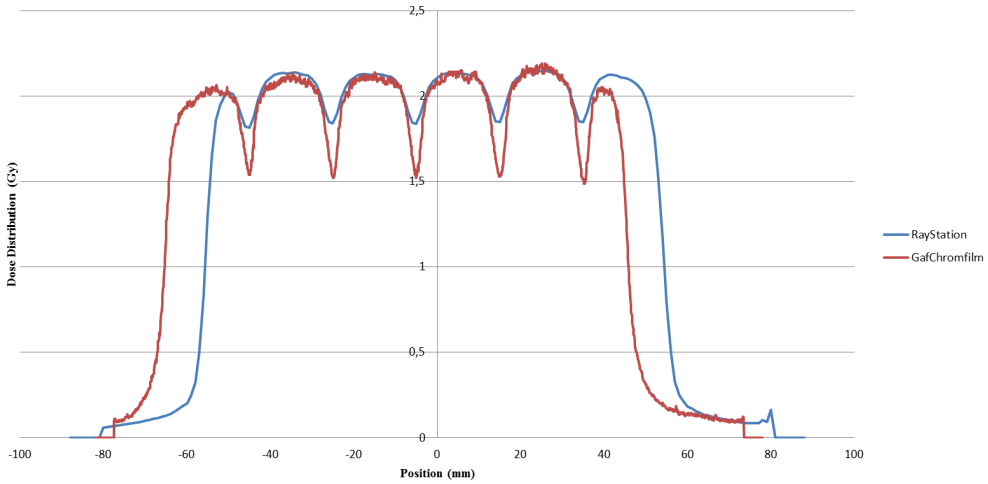


**Figure 4.25:** Dose-profile comparison for the finger-pattern-plan with 20 mm protrusion width. Blue graph is the calculated profile from RayStation and red graph is the measured profile from the gafchromic film.

**Table 4.39:** Mean dose to the three dose curves between position -5 cm and 5 cm.

| Protrusion width | RayStation | Gafchromic film |
|---|---|---|
| 5 mm | 2.01851 Gy | 1.83728 Gy |
| 10 mm | 2.04888 Gy | 1.94027 Gy |
| 20 mm | 2.05614 Gy | 1.99978 Gy |

Chapter 5

# Discussion

As the treatment techniques become more complex, as for IMRT and VMAT, some physical characteristics may increase in importance while others decrease. There are limited researches on MLC positional errors for arc modulated therapy. This study has therefore focused on some of these parameters trying to get a better understanding of how dosimetric predictability of VMAT plans is influenced both by the quality of linac model parameters in the treatment planning system (TPS) and the physical calibration presicion of linac MLC. A robustness-parameter is suggested based on the extracted information of individual treatment plans. An overall goal has been to be able to localize doseplans with high complexity and direct those to a full dosimetric QA with the Delta4 phantom, while less complex plans could pass directly to treatment without further QA.

## 5.1 Linac reproducibility

From the project thesis [Hægeland (2015)] it was concluded that the reproducibility of two of the linacs was satisfying and with a mean error in the $\gamma$-index within 0.62 %. Two deviations excelled from the rest: patient case no. 1 with deviation 2.5 % measured at SB2 and patient case no. 2 with deviation 1.9 % measured on SB6. Because of a satisfying reproducibility of the linacs reported from the project, and also from other studies, it was not tested directly in this thesis. Thompson et al. (2014) evaluated the leaf positioning using 24 x 2 $cm^2$ fields with offset $\pm$9 cm, $\pm$7 cm, $\pm$5 cm, $\pm$3 cm and $\pm$1 cm from the central axis, with 6 MV photons and step and shoot IMRT. They reported that the Agility MLC had a very good repeatability with an uncertainty of 0.02 mm.

Despite good reproducibility of the linacs, some measurements were done twice to ensure that the comparisons were done with data sets from the same day. For the two measurements done on SB2 of the dynamic MLC movement with different field sizes and travel distances (**Results 4.5.2**), the reproducibility was not satisfying. In this thesis the MLC travel distance and MLC opening were sat close to the limit of constraints, making the plans more exposed to uncertainties of the MLC behavior. This may be the reason for a more unstable end result, compared to the previous measurements of the linac reproducibility. In addition, a technical update and calibration were done in the period between the two measurements on SB2, and may have contributed to the poorer

reproducibility.

## 5.2 MLC characteristics

The MLC have a variety of characteristics, both geometrical and physical, that play an important role in the final outcome. The two main parameters that have been studied in this thesis are the tongue-and-groove effect and the MLC leaf position. For the tongue-and-groove (T&G) effect the MLC flank, T&G offset and penumbra have been evaluated. For the MLC leaf positions an investigation of the leaves' dynamic movement, field opening, MLC offset and effect of the gravitation field was performed.

### 5.2.1 MLC movement

The leaf banks in an Agility collimator are mounted on dynamic leaf guides (DLGs) and enables rapid leaf moment through simultaneous leaf and DLG movement, resulting in a potential effective leaf speed of up to 65 mm/s [Vorwerk et al. (2008)]. Different plans were made with various combinations of MLC field openings, travel distances, collimator angles and gantry angles, measuring the MLC behavior at extreme positions (**Results 4.5.2**).

Two field sizes, 2 cm and 4 cm, with various MLC speed, 0.5 cm/deg and 1.0 cm/deg, resulted in different verification values (median to the DD, DTA, $\gamma$-index). The largest field size (with the fastest speed) gave a substantially higher dose distribution and a poorer placement than the field size of 2 cm (with 0.5 cm/deg). How the MLC leaves move between two segments is not known, only how they will be placed at each control point. A faster MLC movement will possibly increase the uncertainty of the MLC motion between two control points. A delay in the movement of rearmost leaf bank would result in a larger MLC opening, which could explain the over-dosage for the fastest MLC speed (1 cm/deg) of these two measurements.

To further study the MLC motion different combinations of MLC speeds (0.5, 1.0 and 1.2 cm/deg) and MLC openings (1.0, 1.5, 2, 4 and 5 cm) were measured. Because of a large deviation between the field size of 1.0 cm and 2.0 cm a second measurement was done including a field size of 1.5 cm. The measurements gave a distinct change in the dosimetric results for field sizes $\leq$ 1.5 cm: the 1 cm field had a designating under-dosage, while fields $\geq$ 1.5 cm achieved a too high dose. The over-dosage was most prominent for the fastest speed (1.2 cm/deg). This result supports the assumption of a delay in the rearmost MLC leaf bank due to the fast MLC motion. The uncertainties regarding the increased MLC speed agrees with the study done by Ghandour et al. (2015). This study reported good agreement for leaf motions equal to 0.3 and 0.5 cm/deg, but for motions greater than 0.8 cm/deg showed poor agreement between the measured and calculated dose distribution.

The 1 cm field size had a significant under-dosage for all MLC speeds, where the slowest speed (0.5 cm/deg) gave the most prominent under-dosage. Compared to the static measurement of the 1 cm field size the error in the DD-median was approximately zero, indicating that the output factor (OPF) for field size 1x1 $cm^2$ is most likely correct. Therefore, uncertainties in the dynamic MLC

motion is suggested to cause the under-dosage for the movement of the fixed 1 cm field size. Because of higher uncertainties in small field size dosimetry static measurements were done for all the three smallest field sizes used in this thesis. The static plans showed good correspondence to the calculated data, suggesting that the OPFs for the these field sizes are set to an approximately correct values. Hence, incorrect OPFs are probably not the reason for the over- and under-dosage of the dynamic moving fields, rather a dynamic movement will make fields more exposed to external influences.

A 1 cm field size is also characterized as a small field [Charles et al. (2014)] and is therefore more vulnerable of influence by geometrical factors and offsets due to the small openings. This corresponds to the measurements of the 1 cm field in this thesis, where the dosimetric results had deviating verification values. The 1.5 cm field size was the threshold for the practical definition of small field sizes by Charles et al. (2014), which also corresponds to the obtained measurements in this task. The dosimetric results to the 1.5 cm field was more equal to larger field sizes, and may indicate a separation between small and large field sizes. Though, more measurements of field sizes between 1 cm and 1.5 cm should be done to confirm this hypothesis.

Regarding the choice of MLC speed, both 1.0 cm/deg and 1.2 cm/deg, exceeded the leaf motion constraint set to 0.5 cm/deg in the clinical optimization settings in RayStation at St. Olavs Hospital. The MLC leaves were therefore tested at extreme situations, with the slowest speed equal the clinical constraint for leaf motion. Using a limit for the leaf travel per degree of gantry motion may have a negative impact on plan quality, but the delivery may by more accurate. Selecting high MLC speeds may therefore have a huge effect on the accuracy of the dose distribution, as shown in the present result. Several studies have reported good accuracy for dose delivering of VMAT plans. Darryl et al. (2012) studied VMAT plans for an Elekta linac and found that the gantry, MLC, and backup jaw maximum speed were internally consistent and that the linac can accurately deliver VMAT plans. The dose rate, gantry speed, and MLC speed were accurately controlled and within clinical acceptability. Hence, the different speeds used in the study of Darryl et al. (2012) were not tested at extreme speeds, as in this thesis. For complex treatment plans fast movements may occur, making it relevant to observe how different components of the linac behave at extreme situations. Relative to other studies this task has looked into the worst case scenario, giving valuable information regarding dynamic movements at extreme situations. Though, for further testing of the MLC motion, MLC speeds below 0.5 cm/deg should also be tested due to clinical relevance. As seen for the sequential and simultaneous plans, the average MLC speed was 0.17 cm/deg and 0.24 cm/deg. And in general for plans with the leaf motion constraint set to 0.5 cm/deg, the MLC speed may not exceed this limit. Even though several studies have reported good accuracy of the MLC collimator, different combinations of hardware and software, delivering and calculating the dose distribution, could result in individualities between hospitals.

### Gravity effects

Different gantry and collimator angles were selected to assess the effect of gravity on the MLC motion: collimator angles at 0° (MLC length with the gravitational field) and 90° (MLC length perpendicular to the gravitational field), at gantry angles 0°, 90° and 270°. For all six gravity-plans

a significant over-dosage occurred. The plans had a 4 cm fixed field opening and a MLC speed of 1 cm/deg with a 24° gantry rotation around the middle points 0°, 90° and 270°. As previous discussed, the MLC speed is a possible explanation for this over-dosage.

At gantry angle 0° the influence from the gravitational field should be at a minimum, which also was the case for the measurements. The difference in the $\gamma$-index between the two collimator angles was here at its smallest, of 4.8 percentage points, compared to the other two gantry angles. Why the difference between collimator angle 0° and 90° was not zero may be explained by the elliptical shape of the source. The extents of the source in the x- and y-width differ, and have been set to a specific value in the beam commissioning in RayPhysics, comparing the calculated and measured data. The widths used at the clinical treatment machine at St. Olavs Hospital are 1.3 mm (x-width) and 0.99 mm (y-width). Correspondingly, a dose error could occur between two different collimator angles.

The gantry angle of 90° had the largest difference in the $\gamma$-index between the collomator angles, with 38.7 percentage point, while the gantry angle of 270° had a difference of 28.3 percentage points. At gantry angles 90° and 270° with collimator angle 0° the gravitational force is at the largest for both the collimators and gantry head. Hence, the collimator angle 90°, where the MLC leaves are not affected by the gravitational field, gave poorer $\gamma$-index than 0° and a higher DD-median. Again the difference in the source width may contribute to a dose difference for the two collimator angles.

Relative to gantry angle 0° the median to the DD increased with 1.2 and 1 percentage points for gantry angles 90° and 270°, respectively. How the gravity may affect the MLC leaves and gantry head may be difficult to predict. From previous done studies Darryl et al. (2012) concluded that the gravity was negligible, which partly disagrees with the result here. The measurements done in this task showed that the median to the DD increased when the gantry head was more exposed to the gravitation field. This disagreement may be due to the individuality of how the gravitational effect was checked. Boylan et al. (2012) reported that the gravity was difficult to determine, corresponding with the result found in this context. Whether or not RayStation TPS accounts for the gravity in the dose calculation is not known and remain for further investigations. The gravity may also have an affect on the MLC placed perpendicular to the field, dragging the MLC leaves closer to each other, which may result in more friction between the leaves. Though, this is not an issue for a fixed MLC opening, which has been used in this context.

From a clinical point of view the total affect of the gravity would most probably be smeared out due to the many field directions of a VMAT plan. The tested gravity-plans seemed to be affected by the gravity, but other than poor verification values it is difficult to predict what the main contributions for the uncertainties are. Further studies need to be done to evaluate the gravity effect more precisely. In this thesis the gravity effect was not further investigated due to the potentially small relevance for the clinical patient cases' outcome.

### 5.2.2 MLC offset

Different MLC offsets were introduced within the RayStation doseplanning system instead of physically dislocate the MLC leaves. As expected, a positive MLC offset of +0.200 cm for the *new_machine_MLC* enlarged the field size by shifting the penumbra farther from the central axis. The median dose to the PTVs increase for all the eight patient plans, though the shape of the dose distribution was not be affected. The average increment of the simultaneous plans was approximately twice as large as for the sequential plans, indicating that the MLC openings of the simultaneous plans were smaller. The relative effect of an enlargement in the MLC offset is greater for a small field size compared to a larger one. The extracted information of the average MLC openings for the simultaneous and sequential plans corresponded well with this result: the average MLC opening of the simultaneous plans was 58 % smaller than for the sequential plans.

Two linac models were created with an MLC offset of $\pm$0.1 cm, called *new_machine_+1mm* and *new_machine_-1mm*. The difference in MLC offset to the original offset (-0.005 cm) was smaller for the negative offset (-1mm) than for the positive offset (+1mm), with differences 0.095 cm and 0.105 cm. This difference is not that significant but, one would still expect a larger deviation for the positive offset with the largest MLC offset deviation. For the sequential plans the average difference in the $D_{50\%}$ of the PTV was slightly greater for the negative than the positive offset. But, since the sequential plans had large MLC openings the relative difference between the positive and negative offset is negligible. For the simultaneous plans the difference in the PTV $D_{50\%}$ was slightly larger for the positive MLC offset, as expected.

Regarding the dose calculation accuracy, which is critical for an accurate dosimetry evaluation, Mzenda et al. (2014) studied the beam models for Elekta Synergi digital accelerators with MLCi and Agility collimators. Comparisons were done with the Pinnacle TPS. Challenging geometries and complex clinical applications were applied to the RayStation TPS, and the overall performance was found to be satisfying. Wang et al. (2016) reported that the plan quality robustness was associated with beam complexity for IMRT plans, and that plans with simple beams were more robust to MLC errors. The sequential optimization sequence appears to result in the simplest treatment plan, compared to the simultaneous sequence, based on the extracted MLC-information (fewer MUs and MLC islands, larger MLC opening, and slower MLC speed). Corresponding to the study done by Wang et al. (2016) the sequential optimization, resulting in the simplest plans, was more robust to MLC errors, compared to the simultaneous (more complex) plans which showed a poorer robustness.

### 5.2.3 Tongue-and-groove effects

The T&G-parameter in the beam commissioning of RayPhysics was changed to 0.20 cm for a machine model called *new_machine_T&G*. Simulations could then be done within the RayStation TPS for the clinical linac (0.05 cm T&G offset) and the *new_machine_T&G*, both linac models applied on the same patient plan. The two identical plans with different linac models could be compared in the Evaluation tab of RayStation, and the effect of the change in T&G offset could then be observed. The *new_machine_T&G* was applied for the simultaneous and sequential optimized

plans, and for the script-plans with MLC finger-patterns.

### Robustness to T&G offset for the sequential and simultaneous optimized plans

For the eight patient cases the average difference in $D_{50\%}$ of the PTV was -4.18 % for the sequential plans and -6.89 % for the simultaneous plans, when comparing the linac model *new_machine_T&G* to the clinical linac in RayStation TPS. Increased T&G offset will result in a decrement of the total dose, due to a larger extent/tilting of the MLC leaf flank causing a higher underdosing at the MLC flank field matching. Since the sequential plans had smaller reduction in total dose than the simultaneous plans, and thereby more robust against errors in the T&G offset, one would assume that the simultaneous plans had a higher amount of MLC flanks than the sequential plans. However, the result from the T&G-script, checking the amount of MLC flanks (**Results tab. 4.12**), showed that the sequential plans had 16 % more MLC flanks than the simultaneous plans. The explanation for this disagreement is that the amount of MLC flanks must be correlated to its field size: for a small field opening the MLC flank will have a relative bigger influence on the dose than for a larger field opening. E.g. a 1 cm MLC flank constitutes 20 % of a 5 cm MLC field opening, while only 10 % for twice the MLC opening (10 cm). Also the amount of MUs will be greater for a small compared to large field size.

**Results tab. 4.16 - 4.18** summarize the extracted information regarding the amounts of MU, MLC opening and MLC flank, and are presented together with the relative difference between the MLC flank and the MLC opening. The average MLC opening for the simultaneous plans was 3.13 cm, and 5.39 cm for the sequential plans. The relative average MLC flank constitutes 19.8 % for the simultaneous plans and 13.4 % for the sequential plans. In addition the simultaneous plans consisted of more separated fields for each segment (MLC islands) and thereby possible MLC flanks got equalized. A lower robustness against the T&G offset for the simultaneous plans corresponds well to the relative amount of MLC flanks.

### T&G offset for the script-plans with finger-pattern

Totally six plans were made checking the effect of T&G offset. The plans consisted of three different finger-pattern widths (0.5, 1 and 2 cm), each with two different linac models (clinical linac and *new_machine_T&G*). All the plans consisted of two arcs of 356° with overlapping finger-pattern (**3.4.2**). Simulations were done in RayStation for the six plans, and measurements were done on the Delta4 phantom of plans (with clinical linac applied) with protrusion widths of 1 and 2 cm.

A comparison was done in the Evaluation tab (RayStation) of two linac models with different T&G offset for the three finger-pattern plans (for illustration of the plans see **fig. 3.10**). A significant reduction in the dose occurred due to the change in the T&G offset, as expected when a high amount of MLC flanks were introduced. This shows that a plan consisting of a high amount of MLC flanks is very sensitive to changes in the T&G offset set at beam commissioning. The reduction in the $D_{50\%}$ relative to the amount of MLC flanks was largest for the plan with 1LP, and decreased as the amount of MLC flanks decreased. Several factors may deviate between the field sizes: the output factor, leaf-tip width and a potential calibration error may have larger influence

on a small field sizes and contribute to a larger reduction in the $D_{50\%}$ when the T&G offset was changed.

The two finger-pattern plans measured on the Delta4 phantom consisted of two arcs with overlapping MLC leaf . The plan with finger-width of 1 cm consists of twice as many protrusions as the plan with finger-width of 2 cm, and was therefore expected to be more exposed to the T&G effect. The measurements agreed with this expectation, showing a larger underdosing for the plan with 1 cm protrusion width. The medians to the dose deviation were -5 % (SB3) and -6.8 % (SB2) for the 1 cm width, while the plan with 2 cm protrusion width had DD-medians of -2.2 % (SB3) and -2.8 % (SB2). The DD-median was reduced (absolute value) by 56 % (SB3) and 58.8 % (SB2) when the width of the protrusion was halved, going from 2 cm protrusion width to 1 cm. Why the reduction in the median was above 50 % could again be explained by the small fields dosimetry, where other MLC parameters may have a larger contribution to the dose distribution for a small field size. There is also a difference in the OPF (output factor) between different field sizes that may contribute to this difference. As previous discussed, a field sizes below 1.5 cm are accounted as small fields and are more exposed to external disturbances like the T&G effect, leaf-tip width, output-factor and calibration error in the MLC leaves. That external factors may have large contribution on small fields may also be seen from the DTA value, which is considerably lower for the 1 cm finger-width than for the 2 cm width.

### 5.2.4 MLC leaf width and MLC transmission

With modern delivery techniques, as for IMRT and VMAT, the effect of the leaf width has been reported by several studies to be very small and has therefore not been focused on in this thesis. Mohan (1995) did a study on the field shaping for 3D conformal radiation therapy and MLC already in 1995, and identified the smearing effect produced by multiple beam fields from many different directions. Therefore, the effect of the leaf width will be smeared out for complex clinical techniques using many treatment fields, as for VMAT. The dose distribution is calculated from the average of the leaf positions from all the different shaped fields, summarized for all field directions. The optimization algorithms for IMRT and VMAT account for the physical parameters of the collimator, thereby minimizing the effect of these in the final dose distribution. Mohan also discussed the effect of the patient motion that could reduce the leaf width effect on the plan. Topolnjak et al. (2007) acknowledged that the patient set-up error could potentially remove the predicted benefits of finer leaves then 0.5 mm by increasing the effective penumbra.

Also, the MLC transmission was not taken into account in this thesis due to the previous studies showing a minimal transmission. Cosgrove et al. (2009) reported a leakage of less than 0.5 % across the entire field.

## 5.3 Dosimetry

Calibration dosimetry has been performed measuring a radiation reference field of 10 x 10 $cm^2$, at 10 cm depth in water, with 100 cm SSD. When measuring output factors (OPF) relative dosimetry

is measured and the dose measured in a field size is normalized to the dose at the reference field. The OPFs are applied to the absolute dose calibration value to obtain the dose to a patient under the patient specific conditions. The source widths were not taken to account in this thesis. Though, one should be aware of that the output and the dose distribution of small fields can be significantly changed by X-Y-jaw settings due to the fact that the radiation source has finite size and is not a point source.

### 5.3.1 Radiation delivery & dose calculation

There is a variety of vendors delivering hardware for radiation therapy planning, and different dose calculation algorithms ranging from simple correction-based algorithms to complex Monte Carlo calculations. The delivery of radiation via many small beamlets makes it challenging to accurately calculate dose in the TPS. This challenge arises due to the difficulty in modeling the MLC in the TPS [Laboratories (2012b)]. RayStation TPS has developed the MLC model by modeling the MLC leaf-end transmission using the leaf-tip width, and using the average transmission factor to model the MLC leaf radiation transmission. The calculated dose difference when introducing a simulated offset in the *MLC x-position* parameter of $\pm 1$ mm in RayPhysics, showed good correspondence to the dose difference of measurements done with physical MLC offset of $\pm 1$ mm.

In this study plan-sets (plans compared with each other) did not obtain equal dose rate/weighting of each control point. This would have been favorable for comparison of the dynamic MLC movement and gantry effects. In RayStation TPS the dose rate and weighting of each CP are changeable and it was possible to make equal plans where only one parameter was different (e.g. collimator angle, gantry angle, or MLC speed). Though, the transfer of the changed plans would not be accepted by the software Mosaiq. Thus, the analysis of the measured plans had to be done with uneven amounts of total MU and different weightings/dose rates of the CPs. E.g. for the gravity-plans the total amount of MUs for plans with $0^\circ$ and $90^\circ$ gantry angle and $0^\circ$ collimator angle were 280 MU, while for the gravity-plan with $270^\circ$ gantry angle it was 400 MU (**fig. 4.19**). The weighting of the CPs also differed between the plans resulting in a higher and smoother dose distribution to the latter plan. A comparison of the dose distribution was therefore difficult to achieve between the plans with different amount of MUs.

The gantry speed and the leaf-travel slow down if the dose to be delivered is too high. The dose rate is calculated to be the maximum that can be used without exceeding any of the constraints of the movement speeds of leaves, jaws and the gantry. If the required MU per degree exceeds what can be delivered at maximum dose rate (600 MU/min), the gantry speed will slow down to accommodate the required MU per degree [Cozzi et al. (2008)]. Again, when comparing different plans with various weightings/dose rates of the CPs another uncertainty factor regarding the gantry speed must be taken into account. A difference in the gantry speed may influence the accuracy of the dose delivery and the amount of dose delivered from different angles. Also, in analysis within the same plan with a gantry moving at different speeds give rise to an extra uncertainty parameter. How much the gantry speed affects the final result and accuracy of a plan has not been studied here, and remains for future work.

### 5.3.2 Field sizes and output factor (OPF)

The challenge of small field dosimetry is due to the lack of charged particle equilibrium (CPE), the geometrical penumbra overlap, detector choice and that small fields are more affected by geometrical parameters of the linac. When the field size is smaller than the lateral range of the electrons contributing to the dose the field is generally defined as a small field [Alfonso et al. (2008)]. This is commonly the case when the OPF changes by $\pm 1.0$ %, given a change in either field size or detector position of up to $\pm 1.0$ mm, then the field size should be considered very small. The consequences of lack of secondary electron equilibrium are still in scientific discussion.

Especially for small field sizes, could a tiny variance in the OPF cause a deviation in the final result. In this thesis, small field sizes were frequently measured. Therefore, measurements were done of the three smallest static fields used in this thesis (1.0, 1.5 and 2.0 cm MLC opening). The measurements showed good agreement with the calculated data, with small deviations: a slightly under-dosage was present for the 1 cm field size, while a slightly over-dosage occurred for the 2 cm field size. The deviations were not significant and the OPFs were concluded to be approximately correct.

The study done by LoSasso et al. (1998) reported that a 1.0 mm position error for a 1.0 cm wide field resulted in a 10 % dose error for sliding window based IMRT. Kron et al. (2012) showed that for a field size of 1.0 x 1.0 $cm^2$ the output changed 15 % due to a 2.0 mm offset in the field size for 6 MV photon, while only a 2 % change appeared for a 2.0 x 2.0 $cm^2$ large field size. The conclusion was that the output factor is sensitive to field size deviation for small fields. Also, using two different dose calculation algorithms, AAA and Acuros XB, the prediction of the output for field sizes smaller than 2.0 x 2.0 $cm^2$ differed [Kron et al. (2012)].

In a clinical context the incidence of very small fields is generally not common. Even if the present of small fields are many, the total effect will be smeared out due to the many segments and field directions of a VMAT plan. For the discussion regarding the different optimization sequences, sequential and simultaneous, the OPFs can with high certainty be excluded.

### 5.3.3 Measurements done with different detectors

Three T&G-plans with overlapping finger-patterns of protrusion widths 5 mm, 10 mm and 20 mm were measured using a diamond detector and a gafchromic EBT film. The dose distribution and penumbra shape were then analyzed comparing the different measurements.

The depth of the wells had a good correspondence between the diamond detector and the gafchromic films, where the depth increased with the field size. Though, the calculated dose distribution had both shallower wells and a different shape than the measured dose curves. The calculated shape is sinusoidal-like around dose level 2 Gy, while the measured curves are steeper with defined turning-points at the bottom of the wells. For protrusion width of 20 mm the calculated top curve broadens,

matching the curves of the film, but still with an underestimated depth of the wells. These comparisons clearly show that the calculated dose distribution underestimates the T&G effect. Tuning the T&G offset for the machine model to a higher value would probably give a more precisely estimate of the T&G effect, and increase the dose level of the measurements.

The diamond detector showed a poor resolution for the smallest protrusion width (5 mm). 5 x 5 $mm^2$ is the minimum field size possible to obtain by the linac, so the gafchromic film is perhaps better for measurements of very small field sizes. Though, several uncertainties are present for the gafchromic films. The films that measured the doses used for the calibration curve did not all have a perfect fit to the calibration curve. This may be due to the film-to-film variation, which is the major source of the dose uncertainty [Saur and Frengen (2008)]. A reduction of the dose uncertainty may be possible by averaging multiple irradiated films, including the films used for calibration. Scanning and image analysis procedure are also relevant film uncertainties. Saur and Frengen (2008) only scanned the films one time due to the optical density for EBT film increases when the number of scans increases.

Another problem associated with small field dosimetry is that the detector itself produces a perturbation due to a difference between the detector and the medium in both composition and density. This perturbation was found hard to quantify in a reliable way by Ding et al. (2007).

## 5.4 Difference in optimization sequence

Two different optimization sequences (sequential and simultaneous) were made and applied to the eight clinical patient cases, evaluating the plan optimization sequences' robustness against different introduced offsets.

### 5.4.1 Analyze of extracted MLC position-information

The extracted information of the MLC positions from the sequential and simultaneous optimized plans showed considerable higher MLC speed (**Results tab. 4.15**) and smaller MLC opening (**Results tab. 4.14**) for the simultaneous plans. The previous hypothesis that a high MLC speed produces a delay in the rearmost MLC leaf bank, causing a larger MLC opening, may contribute in the explanation of the over-dosage for the simultaneous plans (**Results fig. 4.4**). The average MLC speed to the eight simultaneous plans was 0.25 cm/deg and 47 % higher than the sequential plans, with average MLC speed of 0.17 cm/deg. A smaller MLC opening generally results in a larger amount of MUs for the target volume to obtain the same dose. The average MLC opening of the eight patient cases was 42 % smaller for the simultaneous plans relative to the sequential plans, and had 50 % more MUs. An increased amount of MUs makes a plan more vulnerable to calibration errors and MLC flanks. As previous discussed a small field size is also more affected by various parameters such as output factors, penumbra, lateral electronic disequilibrium, and source occlusion.

The extracted information regarding the MLC flank must be seen in relation to the MLC opening for a treatment plan: how much the flank constitutes relative to the field size, and thereby the amount of MUs. The average flank-percentage per MLC leaf pair opening was 13.8 % for the sequential plans and 19.9 % for the simultaneous plans, which corresponds to the fact that the simultaneous plans were more influenced by changes in the T&G parameter. Also with higher amount of MUs for the simultaneous plans the MLC flanks will constitute even more to the final dose distribution. This was also observed when comparing the simulated linac model with T&G offset of 0.2 cm (*new_machine_T&G*) with the clinical linac (T&G offset of 0.05 cm): the simultaneous plans experienced a much larger underdosing than the sequential plans. The average reduction in the $D_{50\%}$ of the eight PTV regions was 73 % higher for the simultaneous plans, relative to the sequential plans.

The measurements done of the T&G-plans with finger-patterns on the diamond detector and the gafchromic films showed that the T&G offset set in beam commissioning probably has a slightly too low value. With a higher T&G offset the calculated depth of the T&G wells would correspond better to the measured dose curves. Though, with a higher value of the T&G offset would result in a lower dose level to the target volumes, especially for plans with a high relative amount of MLC flanks, as seen for the simultaneous plans. The measurements of the simultaneous plans showed a little over-dosage, so with a tiny increase in the T&G offset the calculated dose distribution would give a poorer correspondence to the measured. The T&G offset does thereby not contribute in the explanation of the over-dosage for the simultaneous optimized plans. Relative to a sequential optimized plan the simultaneous plan is generally more exposed to external influences causing larger dose deviation, resulting in a poorer verification value, due to a smaller field size. Because of the faster MLC speed a simultaneous plan is more exposed to a lag in the MLC bank causing a larger field opening. This may be a contributor for the over-dosage of the simultaneous plans.

The patient case no. 7 with sequential optimization deviated considerably from the rest of the patient cases when the MLC offsets of $\pm 1$ mm were introduced. The extracted MLC information, relative to the eight sequential plans, also showed the lowest MLC opening, the largest MLC speed, and the highest amount MLC flank relative to the field size. The plan corresponds to the suggested hypothesis of a robustness index that may disclose a plan that is more vulnerable for external influences.

### 5.4.2 Clinical approval

The coverage of the PTV had a small deviation between the two optimized plans. For most of the patient plans the simultaneous plan had a slightly better coverage of the PTV. The dose distribution to the OARs deviated more, where the sequential optimized plan gave a higher dose to the OARs than the simultaneous plan did. Still the sequential plan did not exceed the maximum dose constraint to the OARs, and therefore may not have any further serious clinical effect to the patients. The overall clinical quality was slightly better for the simultaneous plan, though the difference between the two sequences was not very significant.

### 5.4.3 Comparison with clinical plans

The simultaneous and clinical plans had similar correspondence between the extracted MLC information (**Results 4.3**), with small deviations in the MLC openings, MLC flanks, MLC speeds, amount of MU and amount of MLC islands. However, the accompanying dosimetric results (median to the DD, DTA and $\gamma$-index) had some small deviated, varying from patient to patient. Adding the extracted MLC information together in a robustness-index, this index had a better correspondence to the verification value ($\gamma$-index).

A random choice of patient cases were selected with a verification value ($\gamma$-index) of 100 %. The MLC-information was extracted from these plans, and analyzed against the eight plans with poorer verification values. Excluding patient case no. 4 (which had a readout error: having a $\gamma$-index of 99.3 % and not 93.3 %), the MLC flank relative to the MLC opening was relatively low, around $10 \pm 3$ %. Compared to the sequential and simultaneous plans, this is $\approx 20$ % and $\approx 50$ % lower, respectively. The average amount of MLC islands per MLC leaf pairs was $\approx 7 \pm 3$ islands/leaf pair. Compared to the sequential and simultaneous plans, this is $\approx 13$ % and $\approx 30$ % lower, respectively. The average MLC speed was $\approx 0.12$ cm/deg. Compared to the sequential and simultaneous plans, this is $\approx 30$ % and $\approx 52$ % lower, respectively. As expected, less MLC flank relative to the MLC opening, lower amount of islands/leaf pair, and lower MLC speed are favorable parameters for a treatment plan.

### 5.4.4 Robustness-index

A robustness-index was suggested after studying the different extracted MLC-information from the eight patient cases with the three optimization sequence (sequential, simultaneous and clinical). Based on whether the extracted parameters were favorable of having high or low value, they were added below or above the fraction-slash, resulting in the **e.q. 3.1**.

The effect of adding together all the extracted information gave a distinct separation between the sequential sequence, and the simultaneous and clinical optimization sequence. The robustness-index is thereby suggested to be a good index to estimate the robustness of a treatment plan against external influences. Though, it should be tested in a clinical context, and include the size of the treatment field to make the script more general. In this thesis the eight patient plans had similar size of the treatment fields. The field size was therefore not included in the robusness-index when the script was applied on the plans, but since then the field size has been included in the index.

Chapter 6

# Conclusion

The overall goal of this thesis has been to be able to localize the complexity of doseplans, thereby for less complex plans the dosimetric QA could be skipped and the plan directly given to the patient. The robustness was tested on two different optimization sequences, for eight clinical patient cases, by introducing different offsets: both physical MLC leaf offsets and simulated offsets of the linac model in the dose planning system. The optimization sequence with a sequential sequence showed a significantly better robustness against the introduced offsets, compared to a simultaneous sequence. In the dosimetric QA the sequential sequence also gave substantially better verification degrees than both the simultaneous sequence and the original clinical treatment plans. The sequential optimization sequence is thereby suggested to be a validated sequence, that can be used as a basic sequence to obtain robust treatment plans in the clinic.

Scripting in RayStation TPS was used as a tool to make plans with specific behavior, and to collect data from patient plans. Various information were extracted from patient plans in the TPS, mainly regarding the MLC leaf positions. Comparisons of this information were done between three different optimization sequences for the eight clinical patient cases. Compared to the clinical and simultaneous plans, the sequential optimization sequence gave substantially better values for parameters suggested to be favorable for a plan resulting in a good verification degree. Corresponding to this, ten clinical patient cases, all with verification degree of 100 %, agreed to these parameters. The values of the parameters were: low amount of MLC flank relative to the field opening, low MLC travel distance, and few MLC islands relative to the amount of MLC leaf pairs. The script-plans with specific behaviors mainly focused on the uncertainties regarding the MLC motion. A fast MLC travel distance was suggested to give rise to a lag in the rearmost MLC leaf bank, resulting in a larger field opening, and thereby an increase in the total dose. This may be a possible explanation for the over-dosage of the plans with simultaneous optimization sequence. These plans had a significant higher MLC travel distance than the sequential plans.

A robustness-index has been suggested to give a validated estimate of the robustness of a treatment plan against external influences, and a value of the treatment plan's complexity. The index is based on the extracted information in RayStation TPS, taking into account characteristics regarding the MLC leaf positions, field size, and amount of monitor units. The robustness-index gave

reasonable values of the treatment plans tested in this thesis. It is further suggested to test the index in a clinical context, before determining the need of an individual dosimetric QA.

# Bibliography

Aarup, L., Nahum, A., Zacharatou, C., Juhler-Nottrup, T., Knoos, T., Nystrom, Specht, L., Wieslander, E., Korreman, S., 2009. The effect of different lung densities on the accuracy of various radiotherapy dose calculation methods: implications for tumour coverage.

Ahnesjö, A., 1989. Collapsed cone convolution of radiant energy for photon dose calculation in heterogeneous media.

Alfonso, R., Andreo, P., Capote, R., Huq, M., Kilby, W., Kjäll, P., Mackie, T., Palmans, H., Rosser, K., Seuntjens, J., Ullrich, W., Vatnitsky, S., 2008. A new formalism for reference dosimetry of small and nonstandard fields.

Ashland, 2005. Gafchromic$^{TM}$ radiotherapy films, self-developing film for radiotherapy dosimetry.

Bedford, J. L., Lee, Y. K., Wai, P., South, C. P., Warrington, A. P., 2009. Evaluation of the delta4 phantom for imrt and vmat verification. Institute of Physics and Engineering in Medicine 54 (9).

Boylan, C., McWilliam, A., Johnstone, E., Rowbottom, C., 2012. The impact of continuously-variable dose rate vmat on beam stability, mlc positioning, and overall plan dosimetry.

Brochure, B. S., 2006. The international system of units (si).

Charles, P. H., Cranmer-Sargison, G., Thwaites, D. I., Crowe, S. B., Kairn, T., Knight, R. T., Kenny, J., Langton, C. M., Trapp, J. V., 2014. A practical and theoretical definition of very small field size for radiotherapy output factor measurements.

Cherry, R. N., 2012. Encyclopaedia of occupational health and safety.

Cosgrove, V. P., Thomas, M. D. R., Weston, S. J., Thompson, M. G., Reynaert, N., Evans, C. J., Brown, K. J., Wagter, C. D., Thwaites, D. I., Warrington, A. P., 2009. Physical characterization of a new concept design of an elekta radiation head with integrated 160-leaf, multi-leaf collimator.

Cozzi, L., Dinshaw, K., Shrivastava, S., Mahantshetty, U., Engineer, R., Deshpande, D., Jamema, S., Vanetti, E., Clivio, A., Nicolini, G., Fogliata, A., 2008. A treatment planning study comparing volumetric arc modulation with rapidarc and fixed field imrt for cervix uteri radiotherapy.

Darryl, G., Kaurin, Sweeney, E. L., Marshall, I. E., Mahendra, S., 2012. Vmat testing for an elekta accelerator. Journal of Applied Clinical Medical Physics 13 (2).

Defoor, D. L., Vazquez-Quino, L. A., Mavroidis, P., Papanikolaou, N., Stathakis, S., 2015. Anatomy-based, patient-specific vmat qa using epid or mlc log files.

Ding, G. X., Duggan, D. M., Coffey, C. W., 2007. Comment on 'testing of analytical anisotropic algorithm for photon dose calculation'.

Drzymala, R., Mohan, R., Brewster, L., Chu, M. J., Goitein, M., Harms, W., Urie, B. M., 2009. Dose-volume histograms.

Ghandour, S., Matzinger, O., Pachoud, M., 2015. Volumetric-modulated arc therapy planning using multicriteria optimization for localized prostate cancer. Journal of Applied Clinical Medical Physics 16 (3).

Hægeland, C., 2015. Optimization and verification of vmat dose plans.

ICRU, 1976. International commission on radiation units and measurements.

Kron, T., Clivio, A., Vanetti, E., Nicolini, G., Cramb, J., Lonski, P., Cozzi, L., Fogliata, A., 2012. Small field segments surrounded by large areas only shielded by a multileaf collimator: Comparison of experiments and dose calculation.

Laboratories, R., 2012a. Raystation 4.5, rayphysics manual.

Laboratories, R., 2012b. Raystation 4.5, reference manual.

Laboratories, R., 2012c. Raystation 4.5, user manual.

Levitt, S. H., Purdy, J. A., Perez, C. A., Poortmans, P., 2012. Technical basis of radiation therapy.

Litzenberg, Gallagher, Masi, Lee, Prisciandaro, Hamstra, Ritte, Lam, 2013. A measurement technique to determine the calibration accuracy of an electromagnetic tracking system to radiation isocenter.

LoSasso, T., Chui, C., Ling, C., 1998. Physical and dosimetric aspects of a multileaf collimation system used in the dynamic mode for implementing intensity modulated radiotherapy.

Low, D., Dempsey, J., 2003. Evaluation of the gamma dose distribution comparison method. Medical physics.

Low, D. A., Harms, W. B., Mutic, S., Purdy, J. A., 1997. A technique for the quantitative evaluation of dose distributions.

Mayles, P., Nahum, A., Rosenwald, J., 2007. Handbook of Radiotherapy Physics: Theory and Practice. Taykor and Francis.

Mohan, R., 1995. Field shaping for three-dimensional conformal radiation therapy and multileaf collimation.

Mzenda, B., Mugabe, K. V., Sims, R., Godwin, G., Loria, D., 2014. Modeling and dosimetric performance evaluation of the raystation treatment planning system.

Newbold, K., Partridge, M., Cook, G., Sohaib, S., Charles-Edwards, E., Rhys-Evans, P., Harrington, K., Nutting, C., 2006. Advanced imaging applied to radiotherapy planning in head and neck cancer: a clinical review.

Oliver, M., Ansbacher, W., Beckham., W., 2009. Comparing planning time, delivery time and plan quality for imrt, rapidarc and tomotherapy. Journal of Applied Clinical Medical Physics 10 (4).

Otto, K., 2008. Volumetric modulated arc therapy: Imrt in a single gantry arc.

Palma, D., Verbakel, W., Otto, K., Senan, S., 2010. New developments in arc radiation therapy: a review.

Pillalamarri, I., 2006. Compton scattering.

Podgorsak, E. B., 2005. Radiation oncology physics: A handbook for teachers and students.

Qian, J., Xing, L., Luxton, G., 2011. Dosimetric verification for volumetric modulated arc therapy (vmat) with gating. Medical physics.

Saur, S., Frengen, J., 2008. Gafchromic ebt film dosimetry with flatbed ccd scanner: a novel background correction method and full dose uncertainty analysis. Medical Physics 35 (7).

Software, E. I., 2010. Mosaiq user's guide.

Tertel, J., Wulff, J., Karle, H., Zink, K., 2010. Verification of a commercial implementation of the macro-monte-carlo electron dose calculation algorithm using the virtual accelerator approach.

Thompson, C. M., Weston, S. J., Cosgrove, V. C., Thwaites, D. I., 2014. A dosimetric characterization of a novel linear accelerator collimator.

Thwaites, D., Tuohy, J., 2006. Back to the future: the history and development of the clinical linear accelerator.

Topolnjak, R., van der Heide, U., Meijer, G., van Asselen, B., Raaijmakers, C., Lagendijk, J., 2007. Influence of the linac design on intensity-modulated radiotherapy of head-and-neck plans.

Vorwerk, H., Wagner, D., Hess, C., 2008. Impact of different leaf velocities and dose rates on the number of monitor units and the dose-volume-histograms using intensity modulated radiotherapy with sliding-window technique.

Wang, J., Jin, X., Peng, J., Jiang Xi and, J. C., Hu, W., 2016. Are simple imrt beams more robust against mlc error? exploring the impact of mlc errors on planar quality assurance and plan quality for different complexity beams. Journal of Applied Clinical Medical Physics 17 (3).

Wang, J., Li, X., WD, W. D., Stewart, R., 2003. Impact of prolonged fraction delivery times on tumor control: a note of caution for intensity-modulated radiation therapy (imrt).

Wasbø, E., Kvinnsland, Y., Hysing, L. B., Frengen, J., 2005. 418 vera: A software tool for dose verification and evaluation.

Winiecki, J., Morgas, T., Majewska, K., Drzewiecka, B., 2010. The gamma evaluation method as a routine qa procedure of imrt.

Yu, C., 1995. Intensity-modulated arc therapy with dynamic multileaf collimation: an alternative to tomotherapy.

# Appendix

## A Project thesis

### Reproducibility of the linac

Verification value of the eight patient cases done twice on linac SB6 and SB2 to check the reproducibility of the linac.

**Table 6.1:** Verification values of the two measurements done on SB2 and SB6, checking the reproducibility

| | SB2 | | SB6 | |
|---|---|---|---|---|
| Patient | 1st | 2nd | 1st | 2nd |
| 1 | 92.3 | 94.8 | 96.1 | 95.8 |
| 2 | 97.5 | 97.5 | 97.7 | 99.6 |
| 3 | 93.3 | 93.9 | 91.7 | 90.7 |
| 4 | 99.5 | 99.8 | 99.5 | 99.5 |
| 5 | 95.8 | 95.6 | 90.7 | 89.8 |
| 6 | 96.9 | 95.6 | 94.0 | 95.5 |
| 7 | 98.9 | 99.2 | 99.8 | 99.8 |
| 8 | 96.9 | 96.6 | 99.1 | 99.1 |
| 9 | 94.4 | 99.9 | 99.1 | 99.1 |

### Verification between the four twin-linacs

The verification value (gamma-index) of the nine patient cases measured on each of the four twin-linacs checking the correspondens between them.

**Table 6.2:** Verification value of the nine patient cases measured on each of the four twin-linacs

| Patient no. | Clinical | SB6 | SB2 | SB3 | SB4 |
|---|---|---|---|---|---|
| 1 | 90.2 | 95.95 | 93.55 | 86.9 | 98.1 |
| 2 | 92.0 | 98.65 | 97.5 | 96.2 | 99.8 |
| 3 | 92.5 | 91.2 | 93.6 | 79.6 | 95.2 |
| 4 | 93.3 | 99.5 | 99.65 | 99.1 | 99.3 |
| 5 | 94.0 | 90.25 | 95.7 | 86.6 | 97.2 |
| 6 | 94.9 | 94.75 | 97.0 | 93.4 | 98.3 |
| 7 | 96.1 | 99.8 | 99.05 | 95.9 | 99.2 |
| 8 | 96.2 | 99.1 | 96.75 | 94.2 | 99.5 |
| 9 | 96.2 | 99.1 | 99.65 | 96.9 | 99.1 |

**Comparison between the sequential and simultaneous plan**

**Table 6.3:** Verification values of sequential and simultaneous optimized plans

| Patient no. | **Simultaneous** | | | **Sequential** | | |
|---|---|---|---|---|---|---|
| | Median | DTA | Gamma | Median | DTA | Gamma |
| 1 | 1.8 | 98.5 | 97.4 | 0.3 | 100 | 100 |
| 2 | 1.4 | 99.3 | 93.7 | -0.5 | 100 | 100 |
| 3 | 2.1 | 99.1 | 94.6 | 0.0 | 100 | 100 |
| 4 | 1.1 | 100 | 96.4 | 0.1 | 99.6 | 99.8 |
| 5 | 1.7 | 98.9 | 94.3 | 0.0 | 100 | 100 |
| 6 | 1.6 | 98.7 | 89.8 | 0.0 | 100 | 100 |
| 7 | 1.4 | 99.7 | 97.6 | 1.5 | 99.7 | 97.2 |
| 8 | 1.5 | 98.0 | 96.4 | 0.3 | 100 | 99.8 |

# B Introduced physical MLC offset ($\pm$1 mm)

A physical calibration error in the MLC leaves was introduced to check the robustness of the sequential and simultaneous optimized plans of MLC offset. Three measurements were obtained for each of the plans: without calibration error, with MLC offset -1 mm, and with MLC offset +1 mm.

**Table 6.4:** Measurements of plans without calibration error

| Patient | **Simultaneous** | | | **Sequential** | | |
|---|---|---|---|---|---|---|
| no. | Median | DTA | Gamma | Median | DTA | Gamma |
| **1** | 1.8 | 98.5 | 97.4 | 0.3 | 100 | 100 |
| **2** | 1.4 | 99.3 | 93.7 | -0.5 | 100 | 100 |
| **3** | 2.1 | 99.1 | 94.6 | 0.0 | 100 | 100 |
| **4** | 1.1 | 100 | 96.4 | 0.1 | 99.6 | 99.8 |
| **5** | 1.7 | 98.9 | 94.3 | 0.0 | 100 | 100 |
| **6** | 1.6 | 98.7 | 89.8 | 0.0 | 100 | 100 |
| **7** | 1.4 | 99.7 | 97.6 | 1.5 | 99.7 | 97.2 |
| **8** | 1.5 | 98.0 | 96.4 | 0.3 | 100 | 99.8 |

**Table 6.5:** Measurements of plans with physical MLC offset of -1mm

| Patient | **Simultaneous** | | | **Sequential** | | |
|---|---|---|---|---|---|---|
| no. | Median | DTA | Gamma | Median | DTA | Gamma |
| **1** | -3.0 | 96.9 | 76.7 | -2.0 | 98.8 | 94.2 |
| **2** | -2.7 | 97.8 | 68.0 | -1.7 | 100 | 98.1 |
| **3** | -2.1 | 99.5 | 85.5 | -1.8 | 99.3 | 93.6 |
| **4** | -3.3 | 97.5 | 45.0 | -2.4 | 98.8 | 80.1 |
| **5** | -2.2 | 96.0 | 82.5 | -1.7 | 99.6 | 94.6 |
| **6** | -1.7 | 95.9 | 89.0 | -2.0 | 95.0 | 86.9 |
| **7** | -2.8 | 98.3 | 69.0 | -2.9 | 96.9 | 62.5 |
| **8** | -3.3 | 94.4 | 72.7 | -2.2 | 98.8 | 88.3 |

**Table 6.6:** Measurements of plans with physical MLC offset of +1mm

| Patient | **Simultaneous** | | | **Sequential** | | |
|---|---|---|---|---|---|---|
| no. | Median | DTA | Gamma | Median | DTA | Gamma |
| **1** | 6.4 | 39.6 | 17.3 | 2.6 | 91.0 | 85.4 |
| **2** | 5.2 | 83.4 | 36.3 | 0.5 | 100 | 100 |
| **3** | 6.0 | 52.3 | 23.0 | 1.8 | 97.4 | 93.8 |
| **4** | 5.5 | 64.0 | 14.8 | 2.4 | 92.2 | 83.5 |
| **5** | 5.6 | 49.4 | 17.7 | 1.6 | 97.5 | 95.1 |
| **6** | 6.4 | 46.4 | 11.1 | 2.0 | 90.3 | 82.7 |
| **7** | 5.2 | 71.3 | 23.2 | 5.5 | 69.0 | 22.9 |
| **8** | 6.2 | 56.0 | 33.1 | 2.5 | 92.3 | 84.5 |

### DVH comparison

Comparison of DVHs for the two different optimized plans, with and without MLC offset ($\pm 1$ mm).

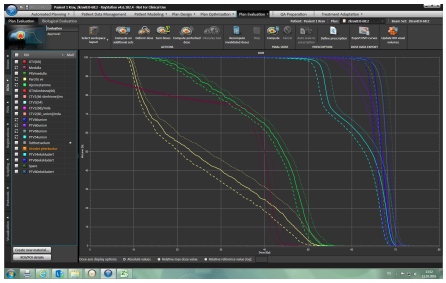

**(a)** Sequential optimization

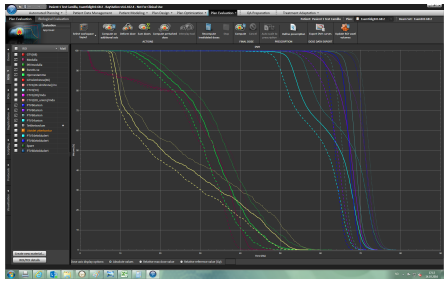

**(b)** Simultaneous optimization

**Figure 6.1:** Patient no. 1 with MLC offset -1 mm (- - - -) and +1 mm (. . . .), and without MLC offset (solid line).

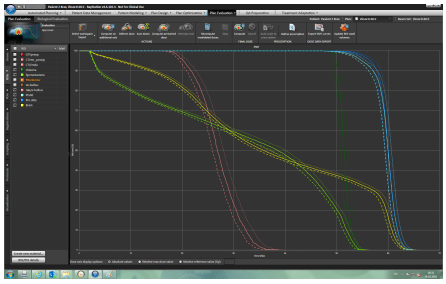

**(a)** Sequential optimization

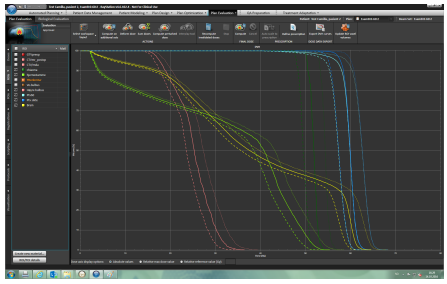

**(b)** Simultaneous optimization

**Figure 6.2:** Patient no. 2 with MLC offset -1 mm (- - - -) and +1 mm (. . . .), and without MLC offset (solid line).

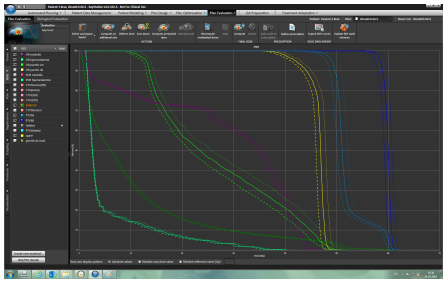

**(a)** Sequential optimization

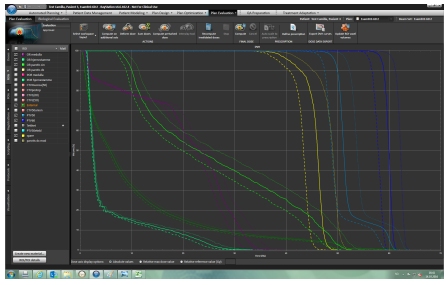

**(b)** Simultaneous optimization

**Figure 6.3:** Patient no. 3 with MLC offset -1 mm (- - - -) and +1 mm (. . . .), and without MLC offset (solid line).

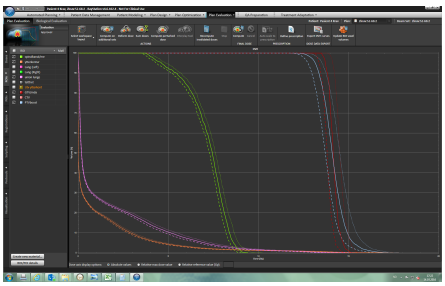

**(a)** Sequential optimization

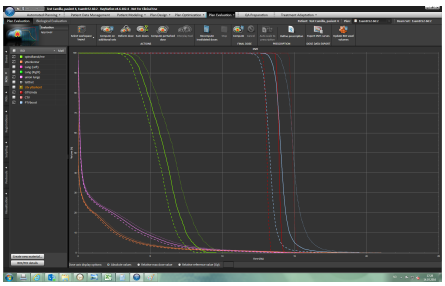

**(b)** Simultaneous optimization

**Figure 6.4:** Patient no. 4 with MLC offset -1 mm (- - - -) and +1 mm (. . . .), and without MLC offset (solid line).

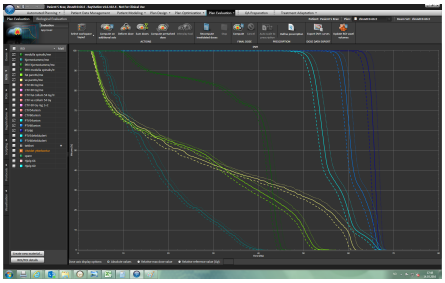

**(a)** Sequential optimization

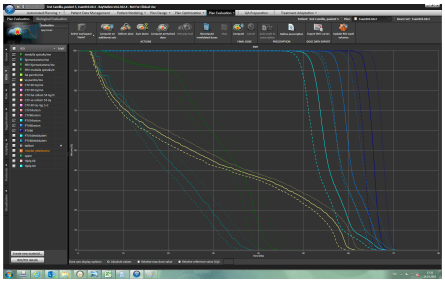

**(b)** Simultaneous optimization

**Figure 6.5:** Patient no. 5 with MLC offset -1 mm (- - - -) and +1 mm (. . . .), and without MLC offset (solid line).

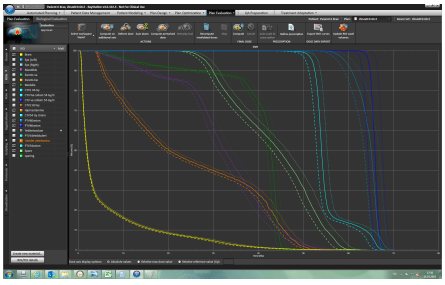

**(a)** Sequential optimization

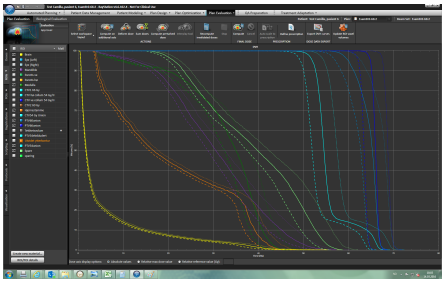

**(b)** Simultaneous optimization

**Figure 6.6:** Patient no. 6 with MLC offset -1 mm (- - - -) and +1 mm (. . . .), and without MLC offset (solid line).

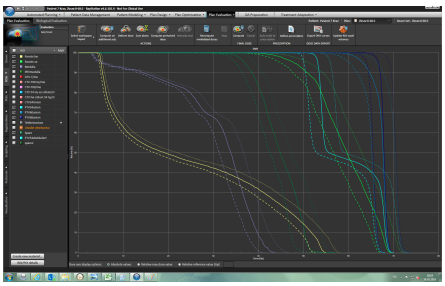

**(a)** Sequential optimization

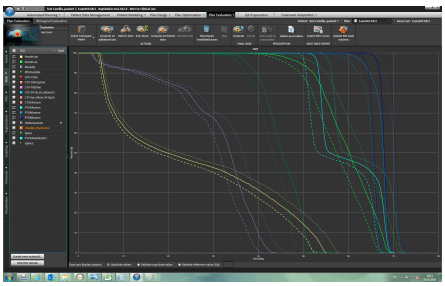

**(b)** Simultaneous optimization

**Figure 6.7:** Patient no. 7 with MLC offset -1 mm (- - - -) and +1 mm (. . . .), and without MLC offset (solid line).

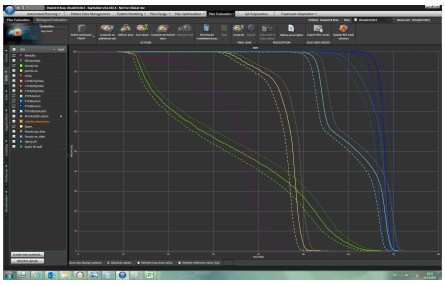

**(a)** Sequential optimization

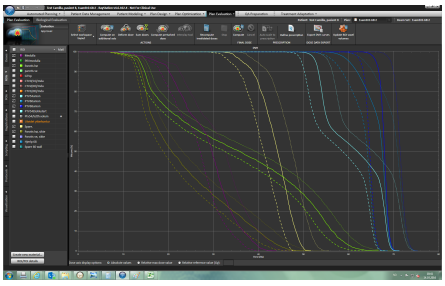

**(b)** Simultaneous optimization

**Figure 6.8:** Patient no. 8 with MLC offset -1 mm (- - - -) and +1 mm (. . . .), and without MLC offset (solid line).

### Comparison of DVH between *new_machine_T&G* and clinical linac

Comparison of DVHs for the two different optimized plans with two different machine models applied: *new_machine_T&G* with T&G offset equal 0.20 cm and clinical linac with T&G offset equal 0.05 cm.

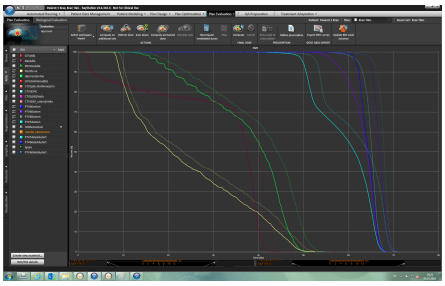

**(a)** Sequential optimization

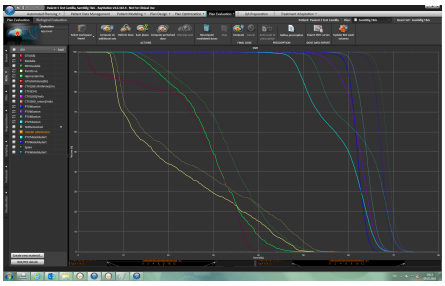

**(b)** Simultaneous optimization

**Figure 6.9:** Patient no. 1 with T&G offset of 0.2 cm (solid line), and without T&G offset (.....).

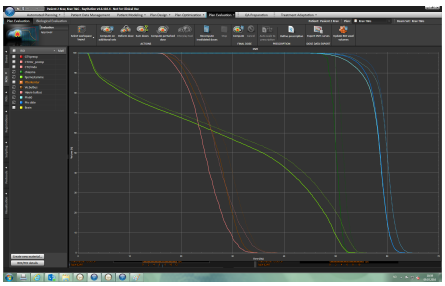

**(a)** Sequential optimization

**(b)** Simultaneous optimization

**Figure 6.10:** Patient no. 2 with T&G offset of 0.2 cm (solid line), and without T&G offset (.....).

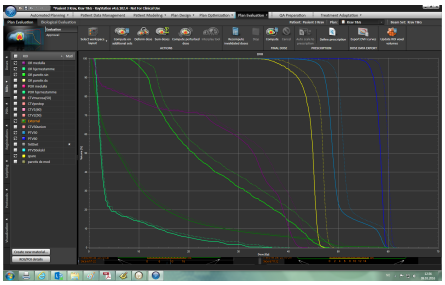

**(a)** Sequential optimization

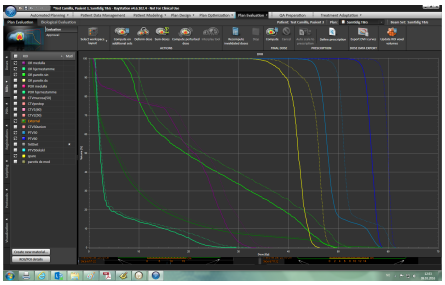

**(b)** Simultaneous optimization

**Figure 6.11:** Patient no. 3 with T&G offset of 0.2 cm (solid line), and without T&G offset (.....).

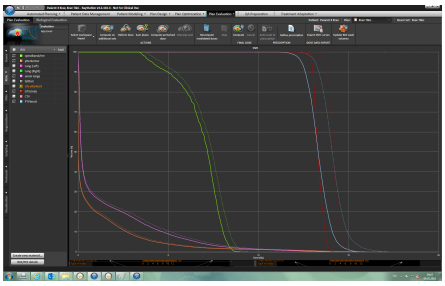

**(a)** Sequential optimization

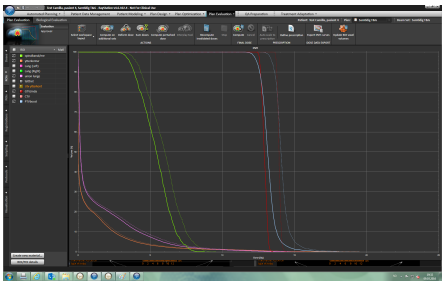

**(b)** Simultaneous optimization

**Figure 6.12:** Patient no. 4 with T&G offset of 0.2 cm (solid line), and without T&G offset (.....).

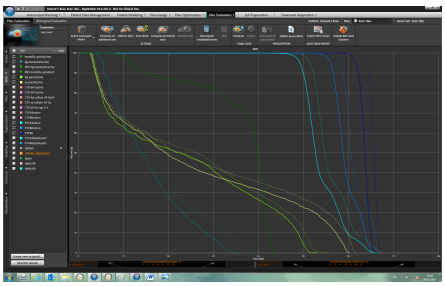

**(a)** Sequential optimization

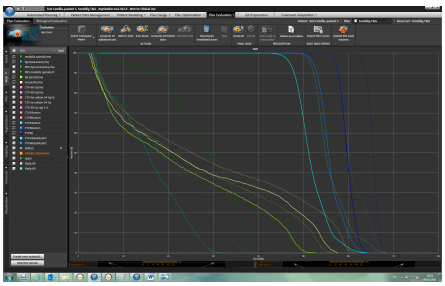

**(b)** Simultaneous optimization

**Figure 6.13:** Patient no. 5 with T&G offset of 0.2 cm (solid line), and without T&G offset (.....).

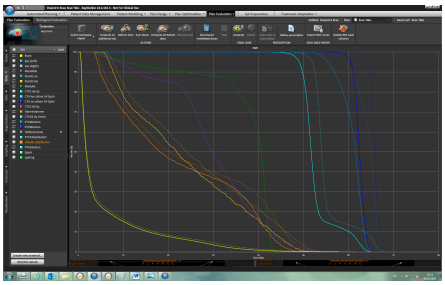

**(a)** Sequential optimization

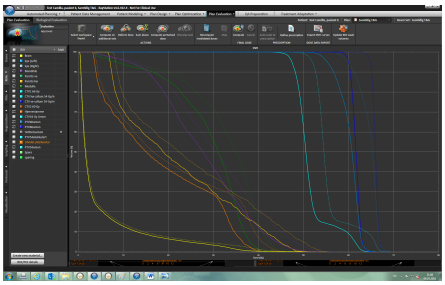

**(b)** Simultaneous optimization

**Figure 6.14:** Patient no. 6 with T&G offset of 0.2 cm (solid line), and without T&G offset (.....).

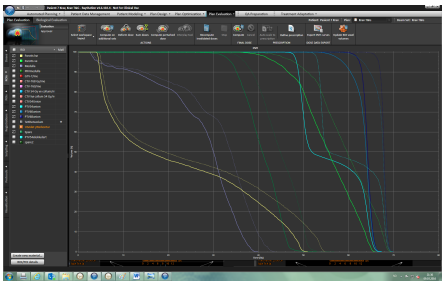

**(a)** Sequential optimization

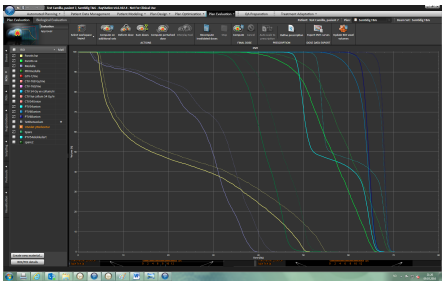

**(b)** Simultaneous optimization

**Figure 6.15:** Patient no. 7 with T&G offset of 0.2 cm (solid line), and without T&G offset (.....).

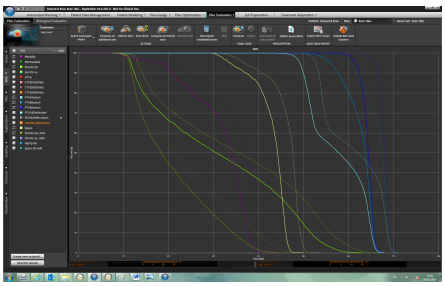

**(a)** Sequential optimization

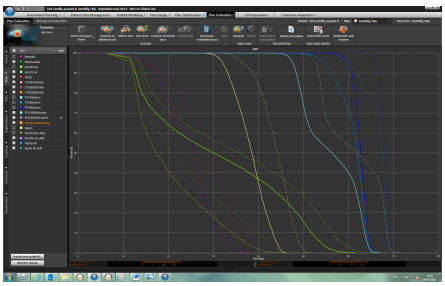

**(b)** Simultaneous optimization

**Figure 6.16:** Patient no. 8 with T&G offset of 0.2 cm (solid line), and without T&G offset (.....).

# C Measurements of plans with specific MLC position

### Constant field sizes

**Table 6.7:** Static plans with fixed field opening, of three different field sizes

| Field opening | | Median | DTA | Gamma |
|---|---|---|---|---|
| **1 cm** | arc1 | 0.0 | 99.5 | 100 |
| | arc2 | -0.5 | 100 | 100 |
| | **Total** | -0.4 | 100 | 100 |
| **1.5 cm** | arc1 | 0.0 | 100 | 100 |
| | arc2 | 0.1 | 100 | 100 |
| | **Total** | 0.0 | 100 | 100 |
| **2 cm** | arc1 | 0.6 | 100 | 100 |
| | arc2 | 0.8 | 100 | 100 |
| | **Total** | 0.6 | 100 | 100 |

### Tongue-and-groove plans

**Table 6.8:** Plans with finger-pattern of 1 cm protrusion width, 2 arcs

| MLC_T&G_2LP_2arcs | | Median | DTA | Gamma |
|---|---|---|---|---|
| **SB3** | arc1 | -4.5 | 94.7 | 89.3 |
| | arc2 | -3.3 | 96.7 | 92.4 |
| | **Total** | **-5.0** | **58.5** | **13,6** |
| **SB2** | arc1 | -5.9 | 93.0 | 86.7 |
| | arc2 | -5.6 | 94.5 | 88.8 |
| | **Total** | **-6.8** | **27.7** | **3.7** |

**Table 6.9:** Plans with finger-pattern of 2 cm protrusion width, 2 arcs

| MLC_T&G_4LP_2arcs | | Median | DTA | Gamma |
|---|---|---|---|---|
| **SB3** | arc1 | -3.3 | 99.3 | 86.1 |
| | arc2 | -2.4 | 98.8 | 84.7 |
| | **Total** | **-2.2** | **88.7** | **62.1** |
| **SB2** | arc1 | -3.2 | 97.8 | 83.4 |
| | arc2 | -3.3 | 98.2 | 82.8 |
| | **Total** | **-2.8** | **75.5** | **46.1** |

### Dynamic movement of a fixed field opening with one arc

**Table 6.10:** 2 cm fixed field opening with MLC speed 0.5 cm/deg, 1 arc of 24 degrees with 0° as middle point

| Linac | Median | DTA | Gamma |
|---|---|---|---|
| **SB2** | 1.0 | 100 | 91.3 |
| **SB3** | 1.0 | 100 | 87.0 |
| **SB4** | 1.2 | 100 | 91.3 |

**Table 6.11:** 4 cm fixed field opening with MLC speed 1 cm/deg, 1 arc of 24 degrees with 0° as middle point

| Linac | Median | DTA | Gamma |
|---|---|---|---|
| **SB2** | 2.8 | 84.2 | 49.9 |
| **SB3** | 2.2 | 94.7 | 60.7 |
| **SB4** | 2.7 | 94.7 | 53.5 |

### Different fixed field-openings with various MLC speeds, 2 arcs

Measurements done of plans with various combinations of field openings and traveling distances.

**Table 6.12:** First measurement done on SB2, traveling distance = 1.25 cm/deg

| Field opening | | Median | DTA | Gamma |
|---|---|---|---|---|
| 1 cm | arc1 | -2.4 | 95.2 | 88.9 |
| | arc2 | -0.5 | 90.2 | 82.5 |
| | **Total** | **-1.1** | **95.0** | **87.0** |
| 2 cm | arc1 | 1.7 | 96.6 | 85.2 |
| | arc2 | 2.5 | 84.0 | 74.9 |
| | **Total** | **2.3** | **92.5** | **84.6** |
| 4 cm | arc1 | 2.3 | 98.6 | 77.2 |
| | arc2 | 2.0 | 82.3 | 65.2 |
| | **Total** | **2.5** | **92.4** | **73.2** |
| 5 cm | arc1 | 1.2 | 97.4 | 91.5 |
| | arc2 | 1.3 | 86.1 | 80.2 |
| | **Total** | **1.5** | **91.5** | **83.9** |

**Table 6.13:** Second measurement on SB2, traveling distance = 1.25 cm/deg

| Field opening | | Median | DTA | Gamma |
|---|---|---|---|---|
| 1 cm | arc1 | -2.0 | 97.6 | 92.2 |
| | arc2 | -0.5 | 96.3 | 85.3 |
| | **Total** | **-0.6** | **95.7** | **89.7** |
| 1.5 cm | arc1 | 0.5 | 96.9 | 84.3 |
| | arc2 | 1.1 | 93.8 | 77.7 |
| | **Total** | **1.6** | **96.9** | **84.2** |
| 2 cm | arc1 | 1.2 | 96.6 | 85.4 |
| | arc2 | 2.0 | 92.0 | 80.9 |
| | **Total** | **1.7** | **95.2** | **82.8** |
| 4 cm | arc1 | 2.0 | 98.6 | 78.9 |
| | arc2 | 2.5 | 91.1 | 72.3 |
| | **Total** | **2.6** | **96.2** | **77.2** |
| 5 cm | arc1 | 1.2 | 100 | 95.7 |
| | arc2 | 1.7 | 93.1 | 84.7 |
| | **Total** | **1.8** | **98.6** | **93.2** |

**Table 6.14:** First measurement on SB2, traveling distance = 1 cm/deg

| Field opening | | Median | DTA | Gamma |
|---|---|---|---|---|
| 1 cm | arc1 | -2.9 | 84.6 | 66.7 |
| | arc2 | -2.2 | 90.6 | 69.8 |
| | **Total** | **-2.9** | **88.4** | **66.7** |
| 2 cm | arc1 | 1.0 | 97.2 | 80.3 |
| | arc2 | 0.8 | 92.4 | 76.2 |
| | **Total** | **0.7** | **94.1** | **80.3** |
| 4 cm | arc1 | 1.5 | 99.0 | 89.9 |
| | arc2 | 1.6 | 87.4 | 83.7 |
| | **Total** | **1.5** | **97.2** | **85.8** |

**Table 6.15:** Second measurement on SB2, traveling distance = 1 cm/deg

| Field opening | | Median | DTA | Gamma |
|---|---|---|---|---|
| 1 cm | arc1 | -3.1 | 85.7 | 68.0 |
| | arc2 | -2.6 | 91.6 | 71.9 |
| | **Total** | **-3.1** | **87.8** | **67.1** |
| 1.5 cm | arc1 | 2.2 | 87.2 | 63.3 |
| | arc2 | 2.2 | 86.5 | 61.7 |
| | **Total** | **2.5** | **86.7** | **66.7** |
| 2 cm | arc1 | 0.8 | 98.6 | 83.6 |
| | arc2 | 0.8 | 95.7 | 79.3 |
| | **Total** | **0.8** | **96.7** | **81.8** |
| 4 cm | arc1 | 1.3 | 99.0 | 93.0 |
| | arc2 | 1.9 | 98.1 | 88.4 |
| | **Total** | **1.8** | **99.1** | **90.6** |

**Table 6.16:** First measurement on SB2, traveling distance = 0.5 cm/deg

| Field opening | | Median | DTA | Gamma |
|---|---|---|---|---|
| 1 cm | arc1 | -3.8 | 99.4 | 88.9 |
| | arc2 | -2.6 | 99.4 | 100 |
| | **Total** | **-2.8** | **99.4** | **95.0** |
| 2 cm | arc1 | -0.3 | 100 | 98.4 |
| | arc2 | 0.2 | 92.8 | 92.9 |
| | **Total** | **0.3** | **98.7** | **97.3** |

**Table 6.17:** Second measurement on SB2, traveling distance = 0.5 cm/deg

| Field opening | | Median | DTA | Gamma |
|---|---|---|---|---|
| 1 cm | arc1 | -4.3 | 100 | 77.8 |
| | arc2 | -2.7 | 98.8 | 95.2 |
| | **Total** | **-3.1** | **100** | **85.0** |
| 1.5 cm | arc1 | 0.2 | 99.5 | 100 |
| | arc2 | -0.1 | 99.5 | 100 |
| | **Total** | **0.3** | **99.5** | **100** |
| 2 cm | arc1 | 0.2 | 100 | 100 |
| | arc2 | 0.4 | 100 | 94.9 |
| | **Total** | **0.3** | **100** | **98.6** |

# D MLC position information, extracted from scripts in RayStation

### MLC opening: distance between MLC leaf [0][j] and MLC leaf [1][j]

**Table 6.18:** MLC opening: average distance between leaf pairs (cm)

| Patient no. | Sequential | Simultaneous | Clinical |
|---|---|---|---|
| 1 | 5.01515 | 2.89090 | 2.79905 |
| 2 | 6.75993 | 3.67088 | 3.64075 |
| 3 | 6.11997 | 3.28664 | 2.96052 |
| 4 | 4.53661 | 2.67686 | 2.98642 |
| 5 | 6.80614 | 3.16445 | 2.73948 |
| 6 | 5.75781 | 3.04312 | 2.80847 |
| 7 | 3.38212 | 3.49824 | 3.49210 |
| 8 | 4.72007 | 2.82766 | 2.98963 |
| **Average** | **5.38720** | **3.13230** | **3.05205** |

**Table 6.19:** STD to the MLC openings

| Patient no. | Sequential | Simultaneous | Clinical |
|---|---|---|---|
| 1 | 1.42744 | 0.76300 | 0.76546 |
| 2 | 1.28766 | 1.01427 | 0.98491 |
| 3 | 1.86199 | 0.77405 | 0.77225 |
| 4 | 1.91203 | 0.66300 | 0.94146 |
| 5 | 2.79882 | 0.89889 | 0.81627 |
| 6 | 1.64369 | 0.82747 | 0.56756 |
| 7 | 0.87343 | 0.91977 | 0.90282 |
| 8 | 0.98897 | 0.59083 | 0.79040 |
| **Average** | **1.59930** | **0.80640** | **0.81764** |

**MLC speed: average travel distance of a MLC leaf between two segments**

**Table 6.20:** MLC speed: MLC travel distance between two segments

| Patient no. | Sequential | Simultaneous | Clinical |
|---|---|---|---|
| 1 | 0.68724 | 0.99011 | 0.97245 |
| 2 | 0.45865 | 0.85893 | 0.72714 |
| 3 | 0.62984 | 0.95836 | 1.02390 |
| 4 | 0.45928 | 0.82842 | 0.96166 |
| 5 | 0.77921 | 1.20061 | 1.25747 |
| 6 | 0.68694 | 1.08944 | 1.03210 |
| 7 | 1.05556 | 1.04702 | 1.04076 |
| 8 | 0.79473 | 1.01586 | 0.80541 |
| **Average** | **0.69393** | **0.99859** | **0.97761** |

**Table 6.21:** STD to the MLC speed

| Patient no. | Sequential | Simultaneous | Clinical |
|---|---|---|---|
| 1 | 0.22585 | 0.27911 | 0.27679 |
| 2 | 0.20042 | 0.27372 | 0.26794 |
| 3 | 0.22110 | 0.29414 | 0.27596 |
| 4 | 0.28248 | 0.42580 | 0.75243 |
| 5 | 0.31770 | 0.29327 | 0.30215 |
| 6 | 0.23890 | 0.26157 | 0.25404 |
| 7 | 0.23920 | 0.25865 | 0.26083 |
| 8 | 0.21937 | 0.22966 | 0.24146 |
| **Average** | **0.24313** | **0.28949** | **0.32895** |

**MLC flank: distance of the longside of MLC leaf where it is exposed to an open field**

**Table 6.22:** Amount of MLC flank (cm)

| Patient no. | Sequential | Simultaneous | Clinical |
|---|---|---|---|
| 1 | 0.73855 | 0.59425 | 0.60451 |
| 2 | 0.75831 | 0.67433 | 0.69334 |
| 3 | 0.78630 | 0.61923 | 0.64000 |
| 4 | 0.51010 | 0.46015 | 0.44560 |
| 5 | 0.71721 | 0.63239 | 0.60160 |
| 6 | 0.78652 | 0.64448 | 0.62247 |
| 7 | 0.63850 | 0.63779 | 0.63008 |
| 8 | 0.82851 | 0.70762 | 0.67232 |
| **Average** | **0.72050** | **0.62128** | **0.61374** |

**Table 6.23:** STD to the MLC flank

| Patient no. | Sequential | Simultaneous | Clinical |
|---|---|---|---|
| 1 | 0.05021 | 0.03525 | 0.02580 |
| 2 | 0.03151 | 0.03851 | 0.05039 |
| 3 | 0.06265 | 0.02613 | 0.03573 |
| 4 | 0.05709 | 0.02372 | 0.02631 |
| 5 | 0.05206 | 0.02447 | 0.04800 |
| 6 | 0.06805 | 0.03850 | 0.05681 |
| 7 | 0.05101 | 0.05374 | 0.05423 |
| 8 | 0.05577 | 0.05358 | 0.03969 |
| **Average** | **0.05354** | **0.03674** | **0.04212** |

**MLC islands: total amount of open fields, surrounded by MLC leaves/y-jaws**

**Table 6.24:** Total amount of MLC islands

| Patient no. | Sequential | Simultaneous | Clinical |
|---|---|---|---|
| 1 | 257 | 400 | 444 |
| 2 | 198 | 305 | 280 |
| 3 | 251 | 280 | 339 |
| 4 | 266 | 286 | 283 |
| 5 | 326 | 419 | 482 |
| 6 | 339 | 442 | 402 |
| 7 | 271 | 262 | 274 |
| 8 | 322 | 420 | 449 |
| **Average** | **279** | **352** | **369** |

# E Comparison of extracted MLC-information

**Table 6.25:** Extracted information from the eight clinical patient cases

| Patient no. | Total MU | MLC flanke | STD | MLC opening | STD | MLC speed | STD |
|---|---|---|---|---|---|---|---|
| 1 | 493.78 | 0.60451 | 0.02580 | 2.79905 | 0.76546 | 0.97245 | 0.27679 |
| 2 | 404.90 | 0.69334 | 0.05039 | 3.64075 | 0.98491 | 0.72714 | 0.26794 |
| 3 | 470.93 | 0.64000 | 0.03573 | 2.96052 | 0.77225 | 1.02390 | 0.27596 |
| 4 | 549.23 | 0.44560 | 0.02631 | 2.98642 | 0.94146 | 0.96166 | 0.75243 |
| 5 | 553.09 | 0.60160 | 0.04800 | 2.73948 | 0.81627 | 1.25747 | 0.30215 |
| 6 | 499.93 | 0.62247 | 0.05681 | 2.80847 | 0.56756 | 1.03210 | 0.25404 |
| 7 | 426.17 | 0.63008 | 0.05423 | 3.49210 | 0.90282 | 1.04076 | 0.26083 |
| 8 | 472.78 | 0.67232 | 0.03969 | 2.98963 | 0.79040 | 0.80541 | 0.24146 |
| **Average** | **483.85** | **0.61374** | **0.04212** | **3.05205** | **0.81764** | **0.97761** | **0.32895** |

**Table 6.26:** Amount of total MU

| Patient no. | Sequential | Simultaneous | Clinical |
|---|---|---|---|
| 1 | 294.70 | 490.91 | 493.78 |
| 2 | 226.25 | 416.75 | 404.90 |
| 3 | 258.89 | 421.81 | 470.93 |
| 4 | 417.57 | 588.60 | 549.23 |
| 5 | 296.52 | 512.53 | 553.09 |
| 6 | 293.38 | 475.53 | 499.93 |
| 7 | 438.42 | 421.23 | 426.17 |
| 8 | 315.79 | 500.33 | 472.78 |
| **Average** | **317.69** | **478.46** | **483.85** |

**Table 6.27:** Clinical cases with 100 % verification degree

| **Plassering** | **MU** | **Flanke** | STD | **Opening** | STD | **Speed** | STD |
|---|---|---|---|---|---|---|---|
| $Brain_1$ | 212.78 | 0.45568 | 0.06034 | 6.33893 | 0.65092 | 0.13038 | 0.15507 |
| $Brain_2$ | 230.16 | 0.58553 | 0.04078 | 6.62701 | 1.44866 | 0.46475 | 0.34295 |
| $Otolaryngologi_1$ | 234.20 | 0.35507 | 0.01648 | 4.74435 | 1.24680 | 0.30608 | 0.28368 |
| $Otolaryngologi_2$ | 460.95 | 0.70163 | 0.03519 | 3.34049 | 0.60112 | 1.00780 | 0.22058 |
| Prostate | 389.57 | 0.80534 | 0.08227 | 6.30515 | 1.68821 | 0.78309 | 0.27909 |
| Ani | 271.89 | 0.61752 | 0.04606 | 6.84201 | 1.03309 | 0.41492 | 0.24308 |
| Recti | 314.42 | 0.59141 | 0.08512 | 5.29908 | 1.38750 | 0.38069 | 0.20197 |
| NH lymfom | 253.74 | 0.49073 | 0.05626 | 8.17337 | 1.41306 | 0.16476 | 0.11575 |
| gallegang | 384.95 | 0.47582 | 0.02538 | 3.98593 | 1.66734 | 0.72339 | 0.37815 |

**Table 6.28:** Clinical cases with 100 % verification degree

| **Plassering** | **# open fields** | **# segments** | **# leafs (average)** |
|---|---|---|---|
| $hjerne_1$ | 180 | 180 | 18.0 |
| $hjerne_2$ | 100 | 94 | 25,5 |
| $ØNH_1$ | 94 | 92 | 20.0 |
| $ØNH_2$ | 324 | 180 | 34.0 |
| prostata | 302 | 180 | 36.0 |
| ani | 198 | 180 | 33.5 |
| recti | 202 | 180 | 27.5 |
| NH lymfom | 184 | 180 | 33.0 |
| gallegang | 319 | 180 | 38.0 |

# F Simulated machine models

### Clinical treatment machine

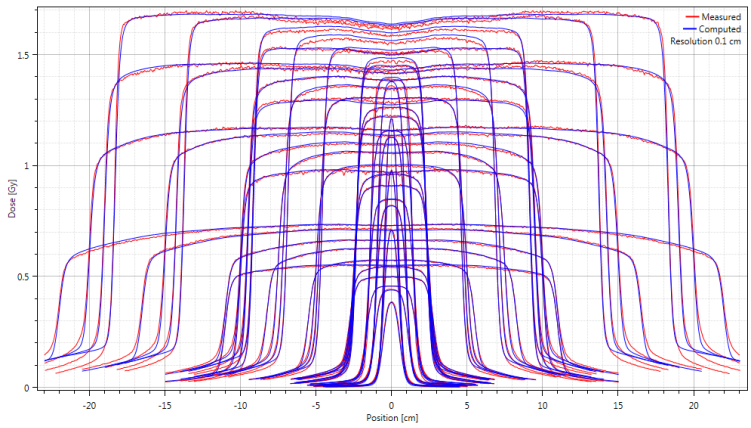


**Figure 6.17:** Cross-plane profiles for the clinical treatment machine.

**Table 6.29:** $D_{50\%}$ to the PTV of sequential and simultaneous plans

| Patient | PTV region | Sequential, D50% | Simultaneous, D50% |
|---|---|---|---|
| 1 | PTV66union | 66.85 | 67.20 |
| 2 | PTV60 | 59.97 | 59.87 |
| 3 | PTV60 | 59.98 | 59.96 |
| 4 | PTVboost | 14.09 | 14.07 |
| 5 | PTV60union | 60.57 | 60.09 |
| 6 | PTV60union | 65.02 | 65.30 |
| 7 | PTV60union | 67.67 | 67.68 |
| 8 | PTV60union | 67.50 | 67.48 |
| **Average** | | **57.71** | **57.71** |

**MLC offset = 0.200 cm, *new_machine_MLC***

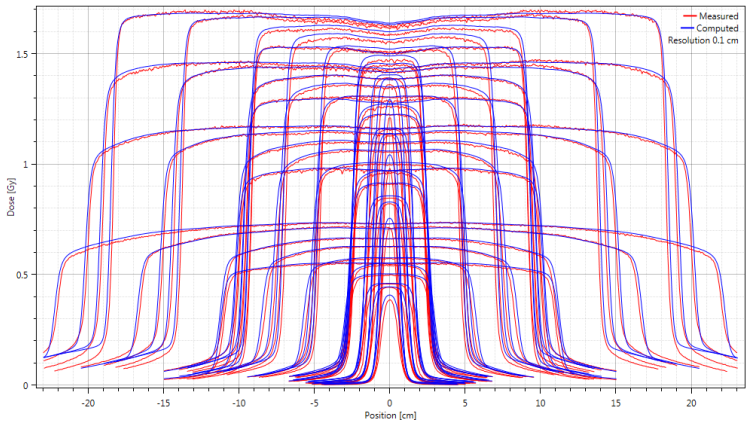


**Figure 6.18:** Cross-plane profiles for the machine model *new_machine_MLC*, with MLC x-position = 0.200 cm.

**Table 6.30:** $D_{50\%}$ to the PTV of sequential and simultaneous plans

| Patient no. | PTV region | Sequential, D50% | Difference from original (%), sequential | Simultaneous, D50% | Difference from original (%), simultaneo |
|---|---|---|---|---|---|
| 1 | PTV66union | 69.76 | 4.35 | 74.73 | 11.21 |
| 2 | PTV60 | 61.22 | 2.08 | 65.05 | 8.65 |
| 3 | PTV60 | 61.48 | 2.50 | 64.34 | 7.30 |
| 4 | PTVboost | 14.89 | 5.68 | 15.75 | 11.94 |
| 5 | PTV60union | 62.53 | 3.24 | 65.33 | 8.72 |
| 6 | PTV60union | 68.11 | 4.75 | 70.63 | 8.16 |
| 7 | PTV60union | 72.69 | 7.42 | 72.41 | 6.99 |
| 8 | PTV60union | 70.55 | 4.52 | 73.93 | 9.56 |
| **Average** | | **60.15** | **4.32** | **63.08** | **9.07** |

**MLC offset = +0.100 cm, *new_machine_+1***

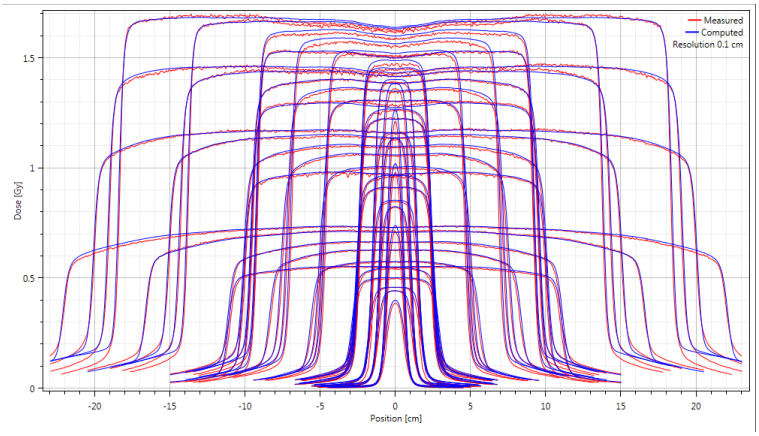


**Figure 6.19:** Cross-plane profiles for the machine model *new_machine_+1*, with MLC x-position = +0.100 cm.

**Table 6.31:** $D_{50\%}$ to the PTV of sequential and simultaneous plans

| Patient no. | PTV region | Sequential, D50% | Difference from original (%), sequential | Simultaneous, D50% | Difference from original (%), simultaneo |
|---|---|---|---|---|---|
| 1 | PTV66union | 68.35 | 2.24 | 71.09 | 5.79 |
| 2 | PTV60 | 60.62 | 1.08 | 62.57 | 4.51 |
| 3 | PTV60 | 60.75 | 1.28 | 62.20 | 3.74 |
| 4 | PTVboost | 14.52 | 3.05 | 14.93 | 6.11 |
| 5 | PTV60union | 61.57 | 1.65 | 62.79 | 4.49 |
| 6 | PTV60union | 66.65 | 2.51 | 68.08 | 4.26 |
| 7 | PTV60union | 70.28 | 3.86 | 70.15 | 3.65 |
| 8 | PTV60union | 69.11 | 2.39 | 70.87 | 5.02 |
| **Average** | | **58.98** | **2.26** | **60.34** | **4.70** |

**MLC offset = -0.100 cm, *new_machine1***

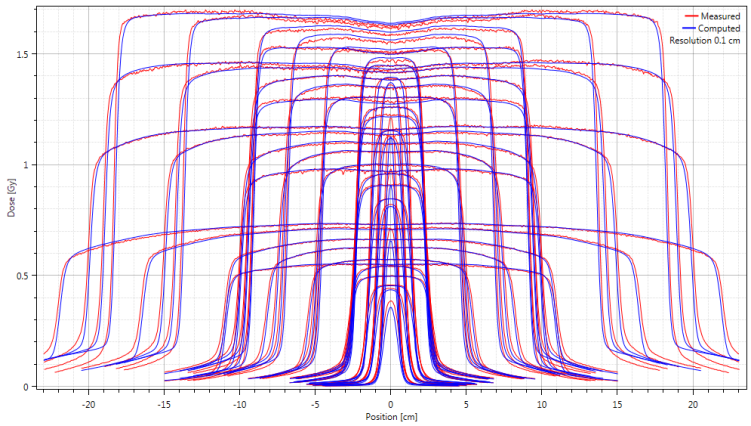


**Figure 6.20:** Cross-plane profiles for the machine model *new_machine_MLC*, with MLC x-position = -0.100 cm.

**Table 6.32:** $D_{50\%}$ to the PTV of sequential and simultaneous plans

| Patient no. | PTV region | Sequential, D50% | Difference from original (%), sequential | Simultaneous, D50% | Difference from original (%), simultaneo |
|---|---|---|---|---|---|
| 1 | PTV66union | 62.78 | -6.09 | 63.67 | -5.25 |
| 2 | PTV60 | 59.37 | -1.00 | 57.31 | -4.28 |
| 3 | PTV60 | 59.27 | -1.18 | 57.89 | -3.45 |
| 4 | PTVboost | 13.71 | -2.70 | 13.28 | -5.61 |
| 5 | PTV60union | 59.67 | -1.49 | 57.64 | -4.08 |
| 6 | PTV60union | 63.42 | -2.46 | 62.69 | -4.00 |
| 7 | PTV60union | 65.19 | -3.66 | 65.35 | -3.44 |
| 8 | PTV60union | 65.94 | -2.31 | 64.15 | -4.93 |
| **Average** | | **56.17** | **-2.61** | **55.25** | **-4.38** |

### Tongue-and-groove offset = 0.20 cm

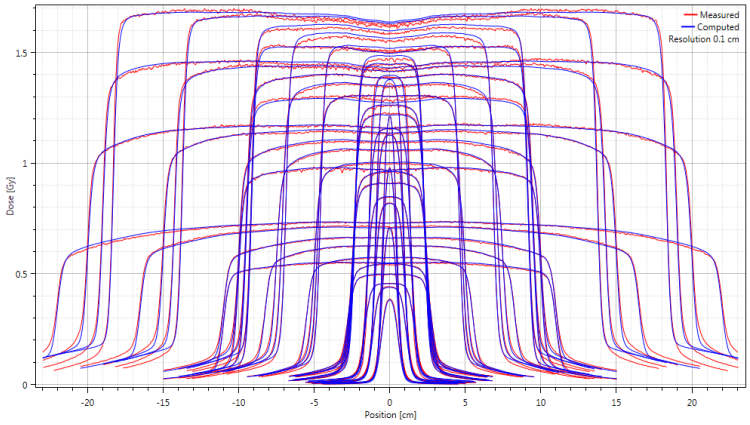


**Figure 6.21:** Treatment machine with T&G offset = 0.20 cm.

**Table 6.33:** $D_{50\%}$ to the PTV of sequential and simultaneous plans

| Patient no. | PTV region | Sequential, D50% | Difference from original (%), sequential | Simultaneous, D50% | Difference from original (%), simultaneo |
|---|---|---|---|---|---|
| 1 | PTV66union | 64.32 | -3.78 | 61.97 | -7.78 |
| 2 | PTV60 | 58.58 | -2.32 | 55.64 | -7.07 |
| 3 | PTV60 | 58.44 | -2.57 | 56.64 | -5.54 |
| 4 | PTVboost | 13.34 | -5.32 | 13.14 | -6.61 |
| 5 | PTV60union | 58.81 | -2.91 | 55.53 | -7.59 |
| 6 | PTV60union | 61.53 | -5.37 | 60.76 | -6.95 |
| 7 | PTV60union | 63.91 | -5.56 | 64.08 | -5.32 |
| 8 | PTV60union | 63.72 | -5.60 | 62.00 | -8.12 |
| **Average** | | **55.33** | **-4.18** | **53.72** | **-6.87** |

# G Scripts

Two scripts were made setting the MLC leaves in wanted positions/achieve wanted behavior. In the first script a dynamic movement was obtained: a fixed MLC opening of wanted size, traveling a selected distance per segment. In the second script a T&G finger-pattern was created of selected protrusion width.
Three scripts were also made for extracting information of the MLC positions: information regarding MLC flank and amount of MLC islands, MLC opening, and MLC travel distance.

### Selection of MLC positions

```
# Dynamic MLC movement, fixed MLC opening, for plan with 24 degrees rotation,
# CP at ever 4th degree → 7 segments for each beam

from connect import *

plan = get_current("Plan")
beam_set = get_current("BeamSet")

# making a function that takes a beam set as input parameter
def CheckMLCLimit(beam_set):

    CurrentBeam = 0
    Beams = beam_set.Beams.Count        # amount of beams for the selected plan

    while Beams > CurrentBeam:

        # amount of segments for the specific beam
        SegmentCount = beam_set.Beams[CurrentBeam].Segments.Count
        SCounter = 0


        # set values of wanted MLC opening and travel distance:
        opening = 2        # selected MLC opening, here set to 2 cm
        o = opening*0.5
       # selected MLC travel distance per segment, here set to 2 cm/CP = 0.5 cm/deg
        MLC_travel_distance = s = 2

        while SCounter < SegmentCount:

            beamset = plan.BeamSets[0]
            LP = LPL = beamset.Beams[CurrentBeam].Segments[SCounter].LeafPositions

            if SCounter < 1:
                for i in range (0 , LP[0].Count-1):
                    LP[0][i] = -o+3*s
```

```
                LP[1][i] = o+3*s
            if SCounter > 0:
                for i in range (0 , LP[0].Count-1):
                    LP[0][i] = -o+2*s
                    LP[1][i] = o+2*s
            if SCounter > 1:
                for i in range (0 , LP[0].Count-1):
                    LP[0][i] = -o+s
                    LP[1][i] = o+s
            if SCounter > 2:
                for i in range (0 , LP[0].Count-1):
                    LP[0][i] = -o
                    LP[1][i] = o
            if SCounter > 3:
                for i in range (0 , LP[0].Count-1):
                    LP[0][i] = -o-s
                    LP[1][i] = o-s
            if SCounter > 4:
                for i in range (0 , LP[0].Count-1):
                    LP[0][i] = -o-2*s
                    LP[1][i] = o-2*s
            if SCounter > 5:
                for i in range (0 , LP[0].Count-1):
                    LP[0][i] = -o-3*s
                    LP[1][i] = o-3*s

            print "The value of Segment Counter is {0}".format(SCounter)

            # Write the modifications back to the LeafPosition object:
            LP = beamset.Beams[CurrentBeam].Segments[SCounter].LeafPositions = LP
            SCounter += 1

        CurrentBeam += 1

# Running the function 'CheckMLCLimit' taking the current beam set as input parameter
print CheckMLCLimit(get_current('BeamSet'))
```

### Selection of T&G MLC position

```
# Dynamic MLC movement
# constant MLC opening
# for plan with 24 degrees rotation,
# CP at ever 4th degree → 7 segments for each beam

from connect import *
```

```
plan = get_current("Plan")
beam_set = get_current("BeamSet")

# making a function that takes a beam set as input parameter
def CheckMLCLimit(beam_set):

    CurrentBeam = 0       Beams = beam_set.Beams.Count

    while Beams > CurrentBeam:

        SegmentCount = beam_set.Beams[CurrentBeam].Segments.Count
        SCounter = 0

        while SCounter < SegmentCount:
            beamset = plan.BeamSets[0]
            LP = LPL = beamset.Beams[CurrentBeam].Segments[SCounter].LeafPositions

            if CurrentBeam % 2 == 0:
                for i in range (10 , LP[0].Count-2, 2):
                if i % 4 == 0:
                    LP[0][i] = LP[0][i+1] = 9.0
                    LP[1][i] = LP[1][i+1] = 10.0

                    else:
                        LP[0][i] = LP[0][i+1] = -10.0
                        LP[1][i] = LP[1][i+1] = 10.0

            else:
                for i in range (10 , LP[0].Count-2, 2):
                    if i % 4 == 0:
                        LP[0][i+3] = LP[0][i+2] = -10.0
                        LP[1][i+3] = LP[1][i+2] = -9.0

                    else:
                        LP[0][i+3] = LP[0][i+2] = -10.0
                        LP[1][i+3] = LP[1][i+2] = 10.0

            print "Value of the Segment Counter is {0}".format(SCounter)
            # Write the modifications back to the LeafPosition object
            LP = beamset.Beams[CurrentBeam].Segments[SCounter].LeafPositions = LP
            SCounter += 1

        CurrentBeam += 1

print CheckMLCLimit(get_current('BeamSet'))
```

### Extracted MLC flank-information and amount of MLC islands

```
from connect import *
import clr
import System.Array
import math

beam_set = get_current("BeamSet")

def CheckMLCLimit(beam_set):
  Beams = beam_set.Beams.Count
  CurrentBeam = 0
  averagelist = []
  averagelistSTD = []
  averageopenfields = []
  sumopenfieldperbeam = []
  sumsegmentsperbeam = []

  while Beams > CurrentBeam:
    ActiveBeam = beam_set.Beams[CurrentBeam]
    SegmentCount = ActiveBeam.Segments.Count        # 90 segmenter = SegmentCount
    SCounter = 0

    list_distances = []        # list of MLC flank distances for all the leafs in one segment
    gjliste = []        # list of average MLC flank distances for all the segments (average of 'list_distances')
    openfields = []        # list of #opened fields per segment, containing all the segments

    while SCounter < SegmentCount:        # operation for each segment
      Leaves = ActiveBeam.Segments[SCounter].LeafPositions
      Lcounter=0
      OpenFieldCounter = 1

      # assuming the same # of leaves on each bank
      start = int((20+(ActiveBeam.Segments[SCounter].JawPositions[2]))*2)
      # start leaf = int([20+(-10.5)]*2) = 19
      stop = int(80-(20-ActiveBeam.Segments[SCounter].JawPositions[3])*2)-1
      # stop leaf = int(80-[20-8.5]*2)-1 = 56

      for i in range(start, stop, 1):        # going through all the leafs between start and stop

        if ((Leaves[0][i+1] < Leaves[1][i]) and (Leaves[0][i] < Leaves[1][i+1])):
        # "ordinary" MLC opening
          if Leaves[1][i] >= Leaves[1][i+1]:
            distance1 = Leaves[1][i] - Leaves[1][i+1]        # right MLC leaf
            list_distances.append(distance1)

          if Leaves[1][i+1] > Leaves[1][i]:
```

```
            distance1 = Leaves[1][i+1] - Leaves[1][i]        # right MLC leaf
            list_distances.append(distance1)

        if Leaves[0][i] >= Leaves[0][i+1]:
            distance0 = Leaves[0][i] - Leaves[0][i+1]        # left MLC leaf
            list_distances.append(distance0)

        if Leaves[0][i+1] > Leaves[0][i]:
            distance0 = Leaves[0][i+1] - Leaves[0][i]        # left MLC leaf
            list_distances.append(distance0)

    elif ((Leaves[0][i+1] <= Leaves[1][i]) and (Leaves[0][i] >= Leaves[1][i+1])):
        # overlapping –> OpenFieldCounter += 1
        # right MLC leaf:
        distance1 = (Leaves[0][i] - Leaves[1][i])
        list_distances.append(distance1)
        # add to list containing MLC flank distances
        # left MLC leaf:
        distance0 = (Leaves[0][i+1] - Leaves[1][i+1])
        list_distances.append(distance0)        # add to list containing MLC flank distances
        OpenFieldCounter += 1

    elif ((Leaves[0][i+1] <= Leaves[1][i]) and (Leaves[0][i] <= Leaves[1][i+1])):
        # right MLC leaf
        distance1 = (Leaves[1][i] - Leaves[0][i])
        list_distances.append(distance1)
        # left MLC leaf
        distance0 = (Leaves[1][i+1] - Leaves[0][i+1])
        list_distances.append(distance0)
        OpenFieldCounter += 1

    elif (Leaves[0][i+1] >= Leaves[1][i]):        # overlapping –> OpenFieldCounter += 1
        # right MLC leaf:
        distance1 = (Leaves[1][i] - Leaves[0][i])
        list_distances.append(distance1)        # add to list containing MLC flank distances
        # left MLC leaf:
        distance0 = (Leaves[1][i+1] - Leaves[0][i+1])
        list_distances.append(distance0)        # add to list containing MLC flank distances
        OpenFieldCounter += 1

    # now the list 'list_distances' contains all the MLC flank distances for this segment
    # want to find the average distance for this segment:
    gjsnitt = sum(list_distances)/len(list_distances)
    gjliste.append(gjsnitt)        # add the average flank distance for this segment to the list 'gjsnitt'

    # OpenFieldCounter = number of opened fields for this segment
```

```
            openfields.append(OpenFieldCounter)        # add OpenFieldCounter to the list 'openfields'
            print 'OpenFieldCounter for segment{0}: '.format(SCounter)
            print OpenFieldCounter

            SCounter += 1

        tot_gjsnitt = sum(gjliste)/len(gjliste)        # finding the average flank distance for the beam
        CurrentBeam += 1
        print "Mean MLC flank for beam no. {0}:".format(CurrentBeam)
        print tot_gjsnitt
        print 'Standard deviation:'
        STD = getStandardDeviation(gjliste)
        print STD

        averagelist.append(tot_gjsnitt)
        # add the average flank distance for the beam to the list 'averagelist'
        averagelistSTD.append(STD)

        sumopenfieldperbeam.append(sum(openfields))
        sumsegmentsperbeam.append(len(openfields))

    print "- - - - - - - - - - "
    print "Average distance: "
    print averagelist        # prints the average distances for each beam, presented in a list
    print sum(averagelist)/len(averagelist)        # prints the average distances for all the beams
    print "Average STD: "
    print averagelistSTD
    print sum(averagelistSTD)/len(averagelistSTD)
    print "Number of open fields for each beam: "
    print sumopenfieldperbeam
    print "Segments per beam: "
    print sumsegmentsperbeam

print CheckMLCLimit(get_current('BeamSet'))
```

### Extracted MLC opening-information

```
from connect import *
import clr
import System.Array
import math

beam_set = get_current("BeamSet")

def getStandardDeviation(array):
```

```
mean = sum(array)/len(array)
deviation = []
for x in array:
    devi = (x-mean)*(x-mean)
    deviation.append(devi)
mean_deviation = sum(deviation)/len(deviation)

return math.sqrt(mean_deviation)


def CheckMLCLimit(beam_set):

Beams = beam_set.Beams.Count
CurrentBeam = 0
tot_gjsnitt_list = []
listSTD = []

while Beams > CurrentBeam:
    ActiveBeam = beam_set.Beams[CurrentBeam]

    SegmentCount = ActiveBeam.Segments.Count        # 90 segmenter = SegmentCount
    SCounter = 0
    gjliste = []

    while SCounter < SegmentCount:        # operation for each segment
        start = int((20+(ActiveBeam.Segments[SCounter].JawPositions[2]))*2)
       # start leaf = int([20+(-10.5)]*2) = 19
        stop = int(80-(20-ActiveBeam.Segments[SCounter].JawPositions[3])*2)
       # stop leaf = int(80 - [20-8.5]*2) = 57

        leaf_positions = ActiveBeam.Segments[SCounter].LeafPositions
        distances = [rp - lp for lp, rp in zip(leaf_positions[0][start:stop], leaf_positions[1][start:stop])]

        gjsnitt = sum(distances)/len(distances)
       # finds average value of the distances between the MLC leafs for one segment
        gjliste.append(gjsnitt)        # adds the average value of the distances to the list 'gjliste'

        SCounter += 1


         tot_gjsnitt = sum(gjliste)/len(gjliste)
       # finds the total average of the distances for all segments in one beam
    STD = getStandardDeviation(gjliste)
    # finds the STD of the distances for all segments in one beam

    tot_gjsnitt_list.append(tot_gjsnitt)
```

```
        listSTD.append(STD)

        print 'Amount of MLC leafs'
        print len(leaf_positions[0][start:stop])

        print "Mean distance between the MLC leafs, and STD, for beam no. {0}:".format(CurrentBeam)
        print tot_gjsnitt
        print STD

        CurrentBeam += 1

        # Average of the beams:
        print '- - - - - '
        print "Average mean distance between the MLC leafs:"
        print sum(tot_gjsnitt_list)/len(tot_gjsnitt_list)
        print "Average standard deviation:"
        print sum(listSTD)/len(listSTD)

print CheckMLCLimit(get_current('BeamSet'))
```

### Extracted MLC speed-information

```
from connect import *
import clr
import System.Array
import math

beam_set = get_current("BeamSet")

def CheckMLCLimit(beam_set):

    Beams = beam_set.Beams.Count
    CurrentBeam = 0

    averagelist = []
    averagelistSTD = []

    while Beams > CurrentBeam:
        ActiveBeam = beam_set.Beams[CurrentBeam]

        SegmentCount = (ActiveBeam.Segments.Count - 1)        # 90 segmenter = SegmentCount
        SCounter = 0
        gjliste1 = []
        gjliste2 = []

        while SCounter < SegmentCount:        # operation for each segment
```

```
        Leaves = ActiveBeam.Segments[SCounter].LeafPositions
        Lcounter=0
        # assuming the same # of leaves on each bank

        start = int((20+(ActiveBeam.Segments[SCounter].JawPositions[2]))*2)
       # start leaf = int([20+(-10.5)]*2) = 19
        stop = int(80-(20-ActiveBeam.Segments[SCounter].JawPositions[3])*2) - 1
       # stop leaf = int(80-[20-8.5]*2)-1 = 56

        # Left MLC leafs:
        leaf_1 = ActiveBeam.Segments[SCounter].LeafPositions[0][start:stop]
        leaf_2 = ActiveBeam.Segments[SCounter+1].LeafPositions[0][start:stop]
        distances = [abs(rp - lp) for lp, rp in zip(leaf_1, leaf_2)]

        gjsnitt1 = sum(distances)/len(distances)
       # finds average value of the "speed" between two segment, for left MLC leafs
        gjliste1.append(gjsnitt1)
       # adds the average speed value (for left MLC leafs) to the list 'gjliste1'

        # Right MLC leafs:
        leaf_1 = ActiveBeam.Segments[SCounter].LeafPositions[1][start:stop]
        leaf_2 = ActiveBeam.Segments[SCounter+1].LeafPositions[1][start:stop]
        distances = [abs(rp - lp) for lp, rp in zip(leaf_1, leaf_2)]

        gjsnitt2 = sum(distances)/len(distances)
       # finds average value of the "speed" between two segment, for right MLC leafs
        gjliste2.append(gjsnitt2)
       # adds the average speed value (for right MLC leafs) to the list 'gjliste2'

        SCounter += 1


    tot_gjsnitt_1 = sum(gjliste1)/len(gjliste1)
   # finds total average speed for all segments (left MLC leafs)
    tot_gjsnitt_2 = sum(gjliste2)/len(gjliste2)
   # finds total average speed for all segments (right MLC leafs)

    CurrentBeam += 1

     print "Mean distance between neighboring MLC leafs ([0][j] - [0][j+1]) for beam no. {0}:".for-
mat(CurrentBeam)
    print tot_gjsnitt_1
    print 'Standard deviation:'
    STD1 = getStandardDeviation(gjliste1)
    print STD1
```

```
        print "Mean distance between neighboring MLC leafs ([1][j] - [1][j+1]) for beam no. {0}:".format(CurrentBeam)
        print tot_gjsnitt_2
        print 'Standard deviation:'
        STD2 = getStandardDeviation(gjliste2)
        print STD2

        averagelist.append(tot_gjsnitt_1)
        averagelist.append(tot_gjsnitt_2)
        averagelistSTD.append(STD1)
        averagelistSTD.append(STD2)

        print "- - - - - - - - - -"
        print "Average distance: "
        print sum(averagelist)/len(averagelist)
        print "Average STD: "
        print sum(averagelistSTD)/len(averagelistSTD)

print CheckMLCLimit(get_current('BeamSet'))
```

### Calculation of standard deviation

```
from connect import *
import clr
import System.Array
import math

beam_set = get_current("BeamSet")

def getStandardDeviation(array):

    mean = sum(array)/len(array)
    deviation = []
    for x in array:
        devi = (x-mean)*(x-mean)
        deviation.append(devi)
    mean_deviation = sum(deviation)/len(deviation)
    return math.sqrt(mean_deviation)
```

## H Test for scripts

Two plans were made with specific MLC behavior to check that the scripts were reliable and gave the expected values.

### Test of the MLC speed-script

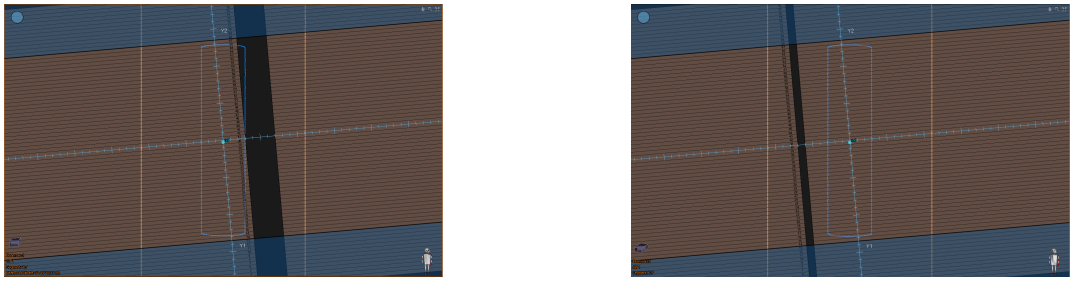

**(a)** 1st segment **(b)** 7th segment

**Figure 6.22:** Test-plan made for testing the MLC speed script

Calculation of the MLC travel distance for a test plan (**fig. 6.22**) where the size of the MLC opening varies between each segment:

Leaf bank 0, varying in positions (cm): 3 → -1 → 1 → -1 → -5 → -7
Total distance between each control point = 18 cm
Average distance for the beam = 18 cm/6 "movements" = 3 cm per MLC leaf travel
STD = 1

Leaf bank 1, varying in positions (cm): 7 → 2 → 3 → 1 → 2 → -2 → -6
Total distance between each control point = 17 cm
Average distance for the beam = 17 cm/6 "movements" = 2.833 cm per MLC leaf travel
STD = 1.5723

Average MLC speed = 17.5 cm/6 = 2.91667 cm per MLC leaf travel
Average STD = 1.286165

**Fig. 6.23** shows the result of the script, which corresponds to the above calculation.

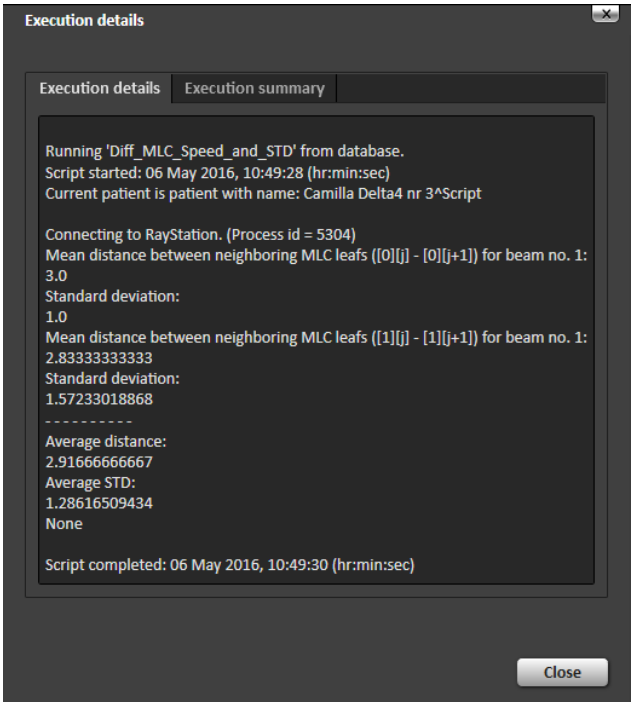


**Figure 6.23:** Results from the script, applied on a test-plan of MLC speed.

***The script used to make the plan:***

```
from connect import *

# for plan with 24 degrees rotation,
# CP at ever 4th degree –> 7 segments/CP
# Left leaf bank: 3 -> -1 -> 1 -> -1 -> -5 -> -3 -> -7 = 18 cm travel distance = 3.0 cm/4deg, STD = 1.00 cm
# Right leaf bank: 7 -> 2 -> 3 -> 1 -> 2 -> -2 -> -6 = 17 cm travel distance = 2.83 cm/4deg, STD = 1.57 cm

plan = get_current("Plan")
beam_set = get_current("BeamSet")

def CheckMLCLimit(beam_set):

    CurrentBeam = 0
    Beams = beam_set.Beams.Count #vanligvis 2 beams

    while Beams > CurrentBeam:

        SegmentCount = beam_set.Beams[CurrentBeam].Segments.Count
        SCounter = 0

        while SCounter < SegmentCount:
```

```
            beamset = plan.BeamSets[0]
            LP = LPL = beamset.Beams[CurrentBeam].Segments[SCounter].LeafPositions

            if SCounter < 1:
                for i in range (0 , LP[0].Count-1):
                    LP[0][i] = 3.0
                    LP[1][i] = 7.0
            if SCounter > 0:
                for i in range (0 , LP[0].Count-1):
                    LP[0][i] = -1.0
                    LP[1][i] = 2.0
            if SCounter > 1:
                for i in range (0 , LP[0].Count-1):
                    LP[0][i] = 1.0
                    LP[1][i] = 3.0
            if SCounter > 2:
                for i in range (0 , LP[0].Count-1):
                    LP[0][i] = -1.0
                    LP[1][i] = 1.0
            if SCounter > 3:
                for i in range (0 , LP[0].Count-1):
                    LP[0][i] = -5.0
                    LP[1][i] = 2.0
            if SCounter > 4:
                for i in range (0 , LP[0].Count-1):
                    LP[0][i] = -3.0
                    LP[1][i] = -2.0
            if SCounter > 5:
                for i in range (0 , LP[0].Count-1):
                    LP[0][i] = -7.0
                    LP[1][i] = -6.0

            print "The value of Segment Counter is {0}".format(SCounter)

            # Write the modifications back to the LeafPosition object
            LP = beamset.Beams[CurrentBeam].Segments[SCounter].LeafPositions = LP
            SCounter += 1

        CurrentBeam += 1

print CheckMLCLimit(get_current('BeamSet'))
```

### Test of T&G plans

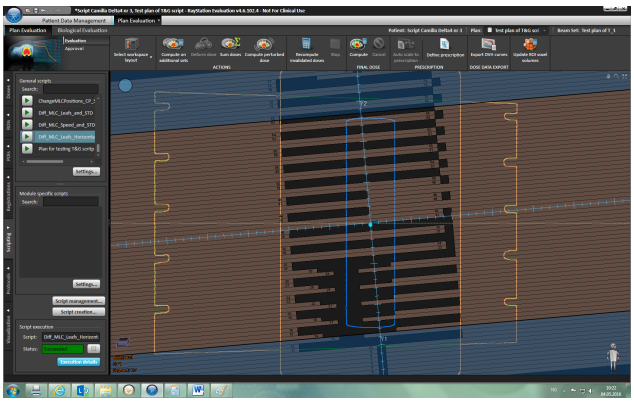

**Figure 6.24:** Test-plan made for testing the MLC flank script.

Calculation of the MLC flank for a test plan (**fig. 6.24**) where different amounts of MLC flanks are introduced for each MLC leaf pair:

MLC islands = 14
MLC flanks:
Leaf 14 – 18: (9+8cm)*2 + 2*3cm + (3+14cm) = 57 cm
Leaf 19 – 30: (5+11cm) + (1+2cm)*3 + 1cm *2+ 7cm*4 + 4cm*6 + (12+7cm) = 98 cm
Leaf 33 – 50: 19cm*6 + 1cm*5 + 10cm*4 = 159 cm
Leaf 53 – 66: (3+14cm)*4 + (3+6cm)*4 + (4+9cm)*4 = 156
TOTAL = 470 cm
MLC leafs = 106
Flanks/leaf = 470cm/106 = 4.396226

**Fig. 6.25** shows the result of the script, which corresonds with the above calculation.

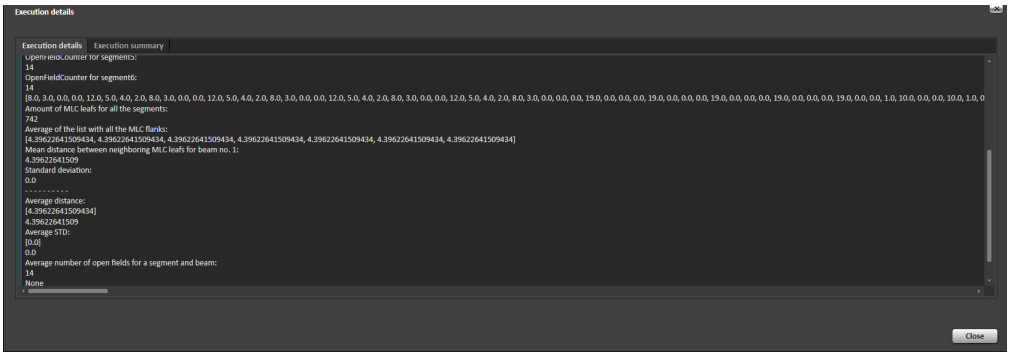


**Figure 6.25:** Results from the script, applied on a test-plan of MLC flank.

***The script used to make the plan:***

```
from connect import *
```

```
# creation of a test-plan to check the T&G scripts

plan = get_current("Plan")
beam_set = get_current("BeamSet")

def CheckMLCLimit(beam_set):

        CurrentBeam = 0
        Beams = beam_set.Beams.Count

        while Beams > CurrentBeam:

            SegmentCount = beam_set.Beams[CurrentBeam].Segments.Count
            SCounter = 0

            while SCounter < SegmentCount:

                beamset = plan.BeamSets[0]
                LP = LPL = beamset.Beams[CurrentBeam].Segments[SCounter].LeafPositions

                if CurrentBeam % 2 == 0:
                    for i in range (10 , 20, 2):
                        if i % 4 == 0:
                            LP[0][i] = -7.0
                            LP[1][i] = -4.0
                            LP[0][i+1] = -1.0
                            LP[1][i+1] = 2.0
                    for i in range (20 , 30, 2):
                        if i % 4 == 0:
                            LP[0][i] = -5.0
                            LP[1][i] = -1.0
                            LP[0][i+1] = -3.0
                            LP[1][i+1] = -2.0
                        else:
                            LP[0][i] = -2.0
                            LP[1][i] = 5.0
                            LP[0][i+1] = -10.0
                            LP[1][i+1] = -6.0
                    for i in range (30 , 40, 2):
                        if i % 4 == 0:
                            LP[0][i] = 9.0
                            LP[1][i] = 10.0
                            LP[0][i+1] = 9.0
                            LP[1][i+1] = 10.0
                        else:
```

```
            LP[0][i] = -10.0
            LP[1][i] = 10.0
            LP[0][i+1] = -10.0
            LP[1][i+1] = 10.0

    for i in range (40 , 50, 2):
        if i % 4 == 0:
            LP[0][i] = 9.0
            LP[1][i] = 10.0
            LP[0][i+1] = 9.0
            LP[1][i+1] = 10.0
        else:
            LP[0][i] = -10.0
            LP[1][i] = 0.0
            LP[0][i+1] = -10.0
            LP[1][i+1] = 0.0

    for i in range (50 , LP[0].Count-4, 2):
        if i % 4 == 0:
            LP[0][i] = -7.0
            LP[1][i] = -4.0
            LP[0][i+1] = -1.0
            LP[1][i+1] = 5.0
        else:
            LP[0][i] = -10.0
            LP[1][i] = 9.0
            LP[0][i+1] = -10.0
            LP[1][i+1] = 9.0


     else:
    for i in range (10 , LP[0].Count-2, 2):
        if i % 4 == 0:
            LP[0][i+3] = -10.0
            LP[1][i+3] = -9.0
            LP[0][i+2] = -10.0
            LP[1][i+2] = -9.0
        else:
            LP[0][i+3] = -10.0
            LP[1][i+3] = 10.0
            LP[0][i+2] = -10.0
            LP[1][i+2] = 10.0

print "Value of the Segment Counter is 0".format(SCounter)
#Write the modifications back to the LeafPosition object
LP = beamset.Beams[CurrentBeam].Segments[SCounter].LeafPositions = LP
SCounter += 1
```

```
            CurrentBeam += 1
print CheckMLCLimit(get_current('BeamSet'))
```